The Pennsylvania State University

The Graduate School

Department of Materials Science and Engineering

STUDY OF FILLED TUNGSTEN BRONZE STRONTIUM BARIUM NIOBATE FOR THERMOELECTRIC APPLICATIONS

A Thesis in

Materials Science and Engineering

by

Jason Chan

Submitted in Partial Fulfillment
of the Requirements
for the Degree of

Master of Science

December 2015

The thesis of Jason Chan was reviewed and approved* by the following:

Clive A. Randall
Professor of Materials Science and Engineering
Thesis Co-Advisor

Susan Trolier-McKinstry
Professor of Ceramic Science and Engineering
Thesis Co-Advisor

Nasim Alem
Assistant Professor of Materials Science and Engineering

Susan Sinnott
Professor of Materials Science and Engineering
Head of the Department

*Signatures are on file in the Graduate School

ABSTRACT

The criteria for developing efficient thermoelectric materials have been well-established: a high electrical conductivity, high Seebeck coefficient, and a low thermal conductivity are all required. These three material properties are encompassed in a dimensionless material figure of merit, zT. Commercial thermoelectrics which use materials with zTs ~ 1 are usually either expensive or non-sustainable. The formulation of an oxide thermoelectric would facilitate achieving sustainability and cost-effectiveness. Currently, there are only a handful of high performance thermoelectric oxides, especially of the n-type variety. The n-type oxide, strontium barium niobate (SBN), had previously been reported to have a figure of merit of 0.5 to 1.0 at 550 K. The higher thermopower is correlated with the precipitation of an NbO_{2-x} secondary phase within the parent material after reaching a particular degree of oxygen-deficiency. The process was found to be reversible, leading to the hypothesis that A-site occupancy within the structure is directly linked to the thermoelectric properties.

In this work, A-site filled strontium barium niobate ($Sr_xBa_{6-x}Nb_{10}O_{30-\delta}$) ceramics prepared by conventional solid-state sintering were explored. The barium end member, $Ba_6Nb_{10}O_{30-\delta}$, served as a model system of study with respect to synthesis and electrical properties. Ceramic samples were prepared by solid-state sintering of powders for the filled SBN compositions. Sr-Ba ratios of 0-100, 10-90, 20-40, 40-60, 60-40, 80-20, and 100-0 were fabricated under 1300-1350°C at ~10^{-16} atm pO_2. Densities of ~95% were reached. Phase purity was assessed by X-ray diffraction (XRD), scanning electron microscopy (SEM), transmission electron microscopy (TEM), and energy dispersive spectroscopy (EDS). Electrical conductivities, Seebeck coefficients and Hall measurements were also used to provide insight into potential thermoelectric properties.

XRD phase purity, and hence solid-solution, was achieved up to the 80-20 composition. Backscatter imaging from SEM and TEM micrographs showed no secondary phases on the microscopic level. Quantitative EDS showed that the 60-40 SBN sample had an A-site cation content of 6.21 +/- 0.33 and 5.07 +/- 0.25 for the filled and unfilled

compositions, respectively. These numbers were within error of the ideal values of 6.00 and 5.00, proving the difference in site occupancy of the filled and unfilled bronze, respectively.

The electrical conductivities of phase pure, non-oxidized filled SBN reached values of at least 120 S/cm. Kinetics were demonstrated to affect the final conductivities such that 30 hour anneals at 1300°C were required for 2.75 mm thick samples. For thin samples (1.38 mm) a 5 hour sinter was enough to achieve high conductivities. The largest conductivities and room temperature conductivities were demonstrated by the 40-60 samples; the values were 700 S/cm at 600 K and 400 S/cm, respectively. The high conductivity was consistent with A-site filling. However, measuring electrical conductivities on samples annealed at 10^{-14} atm pO_2 at 1300°C showed one to two orders of magnitude decrease in the conductivity, despite being phase pure. The carrier concentrations in the filled and unfilled 60-40 composition were on the order of 10^{19} carriers/cm^3 to 10^{21} carriers/cm^3, respectively, implying a different defect compensation between the filled and unfilled bronzes. These two results suggest that the A-site filling plays a part in the high thermoelectric performance, but may not be solely responsible.

Seebeck coefficients were taken to compare the power factors of the filled SBN to those of the unfilled SBNs. The largest power factor was demonstrated in the 60-40 composition with a value of 2.7 $\frac{\mu W}{m-K^2}$ for samples processed under 2.5% H_2 (10^{-16} atm pO_2). Hall measurements were conducted to assess the carrier concentration of the filled and unfilled SBNs. It was found that the carrier concentration was on the order of 10^{21} carriers/cm^3 for these heavily reduced samples, which was consistent with the A-site model hypothesis. This suggests that for the filled SBNs heat-treated at 10^{-16} atm pO_2 are over-reduced and optimization of the power factor would require a higher partial pressure of oxygen during processing.

TABLE OF CONTENTS

LIST OF FIGURES

LIST OF TABLES

ACKNOWLEDGEMENTS

This thesis would not have been possible without the help and support of the MCL staff and fellow graduate student peers. I would especially like to thank my fellow students within the Randall and Trolier-McKinstry groups. Their advice, support, and assistance has been invaluable and I look forward to the continuation of being able to help each other. I would like to give special thanks to Jonathan Bock; this work was a collaborative effort between us in exploring the intricacies and puzzling aspects of strontium barium niobate. I am also very grateful to Joanne Aller, who has assisted me in countless administration tasks. She is without a doubt, one of the best kindest people out there and will not hesitate to help citizens and students alike. I would also like to offer special thanks to Dr. Weiwei Zhao and Jiang Jue from Dr. Moses Chan's group who trained and assisted me in Hall measurements. I also owe gratitude to Dr. Hanzheng Guo for preparing TEM samples and providing the TEM data.

I would also like to thank my family for their continued support and their frequent inquiries and concerns on my financial status. They are too generous. I also owe my friends from home who have confided in me, and I them, as we grow and mature onwards from post-undergraduate life. It has been a fun, yet emotional time. I greatly thank you for your support and frequent status checks.

Last, but certainly not least, I wanted to thank my advisers, Dr. Clive Randall and Dr. Susan Trolier-McKinstry. Their professionalism, wisdom, and standards extend beyond anyone I have ever met. I could not have asked for better advisers in showing me how to be an upright scholar and really showing me how much there is to know out there. They have not only supported me professionally, but also on a personal level, given that the first two years of graduate school were very emotional times with several bumps in life. Their personal advice and regards for my well-being have helped me greatly.

This work was funded by the National Science Foundation and would not be possible without their continued support.

Chapter 1

Introduction

1.1 Thermoelectricity

Thermoelectricity was discovered in 1821 when Thomas Seebeck demonstrated the existence of a thermoelectric potential at a junction between dissimilar metals in the presence of a thermal gradient[1, 2]. This Seebeck effect has two well-known applications: temperature sensing and waste-heat power generation. This is found in thermocouples and thermoelectric generators, respectively. The thermoelectric voltage is dependent on the magnitude of the temperature gradient as well as the properties of the material. This can be expressed as a linear field-response expression in the form of a second rank tensor:

$$E_m = \alpha_{mn} \frac{dT}{dX_n} \quad \textbf{(Eq 1.1)}$$

where E_m is the induced electric field from the thermoelectric potential, α_{mn} is the Seebeck coefficient (also known as thermopower) which describes the change in potential for a given temperature difference, and $\frac{dT}{dX_n}$ is the temperature gradient[3]. The thermopower is therefore, not a "power", but rather, the ratio of the potential difference imparted by the temperature difference when two dissimilar materials are joined. The thermopower possesses the units of V/K and can be expressed as[4]:

$$\alpha = \frac{dV}{dT} \quad \textbf{(Eq 1.2)}$$

where $\frac{dV}{dT}$ is the differential potential developed in response to the temperature difference.

The Seebeck effect is only one of three effects associated with thermoelectricity. Two other interrelated effects, the Peltier effect, and the Thomson-Kelvin effect, complete the description of thermoelectricity. The Peltier effect, discovered in 1834, can be thought of as the "inverse" of the Seebeck effect, such that the application of an applied field will

transport heat from one junction to the other. Thus, the material acts as a solid-state heat pump. The effect is attributed to the difference in the Fermi Energies between two materials in Ohmic contact[2]. Whether heat is released or absorbed at the junction is dependent on whether the charge carrier moves into a state of higher energy or lower energy at the contacts. In the instance where an electron from one material that previously occupied a higher energy moves into the other material with a lower energy state, heat will be released at that junction. As a result, this junction will rise in temperature, as shown in Figure 1-1. An increase (or decrease) of energy of an electron occurs when an electron absorbs (or releases) heat from the environment[4].

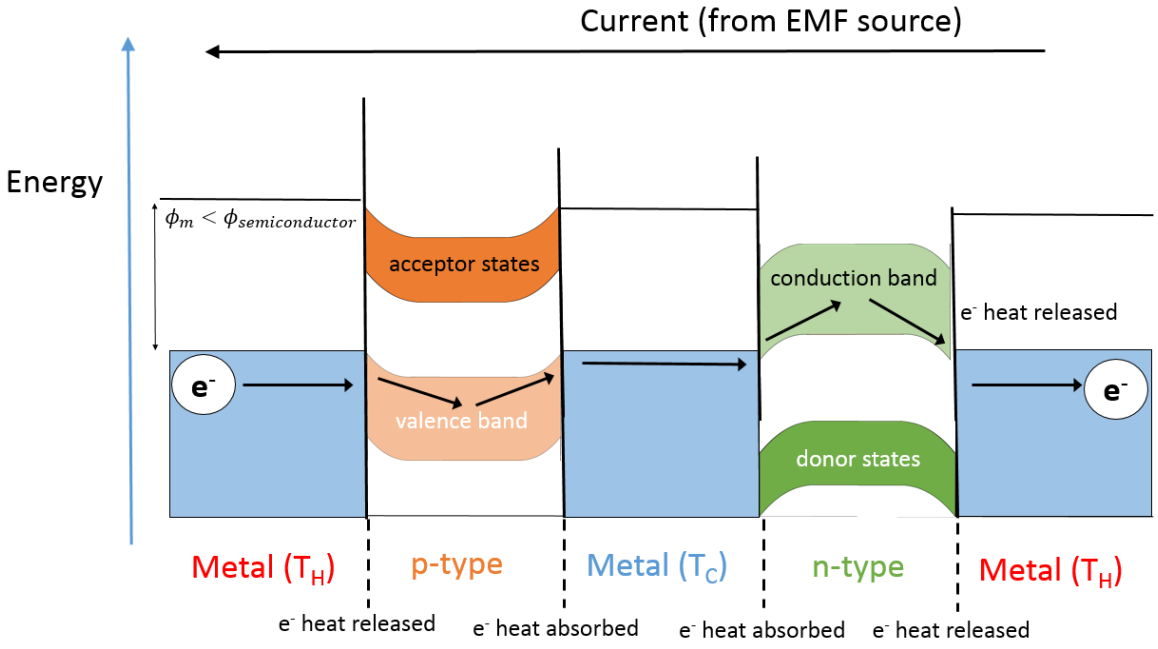

Figure 1-1. The movement of charge carriers at contact points that illustrate the Peltier effect. The bending of the bands has been simplified. The case shown pertains to one in which the work function of the metal is less than the work function of the semiconductors. (Diagram adapted from Tamer and Sparks)[5, 6].

Like the Seebeck effect, the Peltier effect can also be expressed as a second rank tensor:

$$q_m = \pi_{mn} J_n \qquad \textbf{(Eq 1.3)}$$

where $q_m$is the heat flow, π_{mn} the Peltier coefficient, and J_n is the current density[3].

Since a temperature gradient can induce a thermoelectric current, and a current that flows can establish a temperature gradient, it is not illogical to predict a relationship between the Seebeck and Peltier effects. The Thomson-Kelvin effect, discovered in 1854 by William Thomson (Lord Kelvin), represents the reversible thermoelectric heat that is either absorbed or released (depending on the direction of the current) along a conductor in the presence of a temperature gradient[1, 7, 8]. Under this scenario, the net heat per unit volume per second that evolves, $\dot{Q}$, can be represented as:

$$\dot{Q} = \frac{J_x^2}{\sigma} - \varphi J_x \frac{dT}{dX} \quad \textbf{(Eq 1.4)}$$

where the first term is the irreversible Joule heating due to a finite resistance (J_x is the current density in the x-direction and σ is the electrical conductivity), and the second term is the reversible thermoelectric heat, with φ being the Thomson heat or coefficient[1]. More specifically, it is the rate of heating per unit length under a temperature gradient and current [8]. Irreversible thermodynamics can then be used to derive the two Kelvin equations:

$$\varphi = T\frac{d\alpha}{dT} \quad \textbf{(Eq 1.5)}$$

$$\pi = T\alpha \quad \textbf{(Eq 1.6)}$$

Eq 1.5 gives the definition of the Thomson heat. Its significance comes from the fact that upon integration with respect to temperature, it is one method to determine the absolute thermopower of a single material (which would otherwise be challenging since the Seebeck effect involves two dissimilar materials). Eq 1.6 relates the Peltier coefficient to the thermopower, which demonstrates that the figure of merit (discussed in Chapter 2) is the same for both refrigeration and power generation[1].

1.2 Motivation and Objectives of the Thesis

Thermoelectric materials may play a pivotal role in improving energy sustainability. Thermoelectric devices would not necessarily replace current methods of energy generation, but instead, harness the waste-heat that evolves from these processes.

Such processes include the burning of any fossil fuel in automobiles or power plants. Thermoelectric generators are especially attractive in that they are silent and house no moving components[9]. Other advantages include reliability (exceeding 100,000 hours of steady-state operation) and the scalability of size to meet the required application[10].

The factor that prevents thermoelectrics from being widely implemented is the low efficiency-to-cost ratio[9]. Many commercial thermoelectrics contain elements that are costly. For example, tellurium, a component in some of the most widely used thermoelectrics is rather costly as a result of its rarity, which rivals that of Pt[11]. Another example would be germanium in SiGe alloys, the cost per kg of Ge being two orders of magnitude larger than Si[12]. The SiGe alloy, among the most efficient thermoelectric materials at high temperatures, has an efficiency that is only around 8%[13]. Currently, thermoelectrics are used in niche cases, especially where cost concerns are outweighed by other factors, such as in military or space applications[10].

One solution in reducing the cost factor is to develop less expensive alternatives. Since oxygen is the most abundant anion in the earth's crust, occupying about 46% by weight, oxide materials would decrease the cost significantly[14]. Oxides also offer improved oxidation resistance at high temperatures and low-cost synthesis processes[15]. The bulk processing used in the synthesis of many thermoelectric oxides is low-cost relative to nano-structuring or thin film processing as shown by LeBlanc et al.[9].

However, only a handful of useful oxide thermoelectrics have been reported, with the layered cobaltites still leading by almost a factor of 2 in terms of the thermoelectric figure of merit[16]. Oxygen-deficient strontium barium niobate (or SBN, $Sr_{5-x}Ba_xNb_{10}O_{30}$), a complex oxide that crystallizes in the tungsten bronze structure, had been reported by Lee et al. to possess a figure of merit between 0.5 to 1.12 at 550 K. The upper bound rivals that of the layered cobaltites[17]. The reason for the high figure of merit was attributed to the anomalous increase in the electrical conductivity when processed under sufficiently-reducing atmospheres[18]. This increase coincided with the precipitation of a NbO_{2-x} secondary phase[18]. NbO_{2-x} is not thought to be directly responsible for the increase in electrical conductivity. It is instead suggested that there is a possibility that the remaining A-site within the structure is being occupied with the material to produce a "filled-bronze."

The A-site occupancy model is consistent with the work by Hessen et al.[19]. In that work, a reduced, rhombohedral $Ba_2Nb_{15}O_{32}$ crystal was fabricated from borate fluxes. A barium niobate compound with tetragonal tungsten bronze structure ($Ba_6Nb_{10}O_{30}$) was created as a side product during the process[19]. This side-product (BNO) can be regarded as the barium end member in tetragonal tungsten bronze SBN. In the unfilled case, neither the barium end member nor the strontium end member are known to crystallize as a tetragonal tungsten bronze[20].

The BNO side-product was isolated and its electrical conductivity was measured. The results are shown in Figure 1-2. It can be seen that this material possesses a high degree of anisotropic conductivity (about a factor of 55), while the anisotropy of SBN is only by a factor of 10[18]. Furthermore, the magnitudes of the conductivity are larger in the barium end member single crystal by almost a factor of 64 compared to SBN[18]. The trend with temperature also shows that despite very high conductivities, the material still shows a negative coefficient of resistivity, with the high conductivity persisting at room temperature and below.

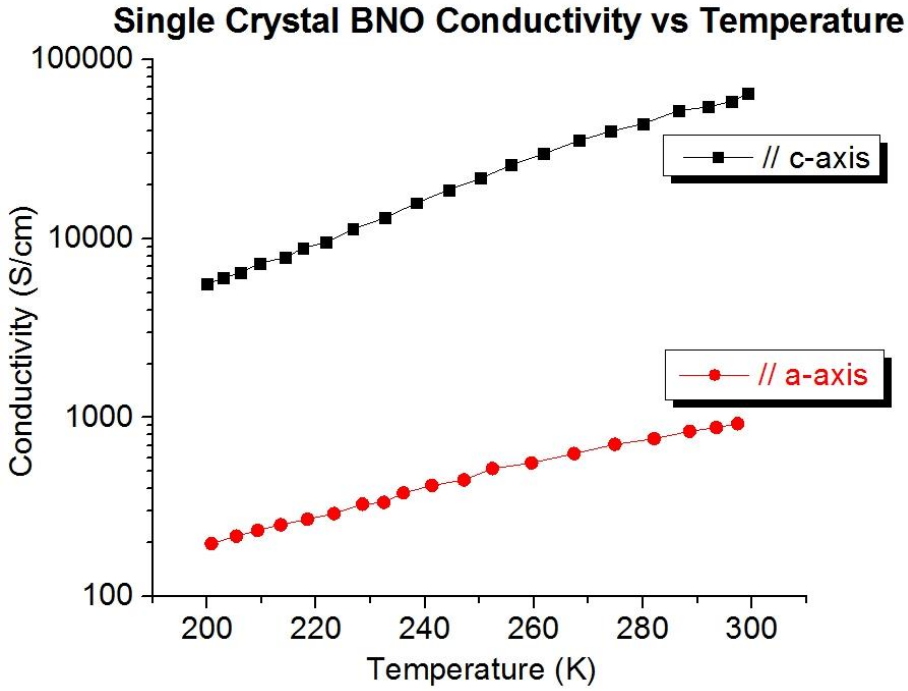

Figure 1-2. Single crystal of BNO grown from borate flux showing high, anisotropic conductivity. Replotted from Sunshine et al.[19].

The objectives of this thesis are as follows:

- Determine if A-site filling can be achieved using conventional ceramic, solid-state processing methods.
- Determine if the A-site filling occurs across the whole solid-solution range of SBN.
- Determine if the A-site filling is responsible for the anomalous increase in the electrical conductivity.
- Assess the thermoelectric performance of the filled SBNs compared to that of the unfilled counterpart.

1.3 Organization of the Thesis

The thesis is organized into 5 chapters, beginning with the introductory chapter. Chapter 2 provides a literature review that covers multiple aspects of thermoelectricity, beginning with a discussion on the thermoelectric figure of merit and ways in which to optimize it. Chapter 2 then reviews some prominent non-oxide and oxide thermoelectrics, to put SBN into context. Chapter 2 also provides a review on two important material properties of the figure of merit: the electrical conductivity and the thermopower. Lastly, Chapter 2 provides a review on the tungsten bronze structure as it pertains to SBN and then reviews SBN as a thermoelectric.

Chapter 3 covers the experimental procedures and methods utilized in this work, starting with powder processing and then sintering of the green bodies. Sample preparation (including density measurements) is then discussed. This chapter also details the methods used for characterization in this work.

Chapter 4 discusses the results of this work as it relates to the objectives of this thesis. Chapter 5 summarizes the findings of this work and gives directions for future work.

1.4 References

[1] D. MacDonald, *Thermoelectricity: an Introduction to the Principles*. Dover Publications, Mineola, New York, 2006.

[2] J. Martin, T. Tritt, and C. Uher, "High Temperature Seebeck Coefficient Metrology," *J. Appl. Phys.*, **108** [2010] 121101–1 – 121101–12 (2010).

[3] R.E. Newnham, *Properties of Materials : Anisotropy, Symmetry, Structure: Anisotropy, Symmetry, Structure*. Oxford University Press, Oxford, 2004.

[4] S.O. Kasap, *Principles of Electronic Materials and Devices*, 3rd ed. McGraw Hill, New York, NY, 2006.

[5] R. Tamer F, L. William S, and D. Russell J, "Temperature Control of Avalanche Photodiode using Thermoelectric Cooler," (1999).

[6] T.D. Sparks, "Oxide Thermoelectrics : The Role of Crystal Structure on Thermopower in Strongly Correlated Spinels;" PhD Thesis, Harvard University, 2012.

[7] D. Rowe, *CRC Handbook of Thermoelectrics*. CRC Press, Boca Raton, FL, 2010.

[8] H.J. Goldsmid, *Introduction to Thermoelectricity*. Springer Science & Business Media, Berlin, Germany, 2010.

[9] S. LeBlanc, S.K. Yee, M.L. Scullin, C. Dames, and K.E. Goodson, "Material and Manufacturing Cost Considerations for Thermoelectrics," *Renew. Sustain. Energy Rev.*, **32** 313–327 (2014).

[10] S.B. Riffat and X. Ma, "Thermoelectrics: a Review of Present and Potential Applications," *Appl. Therm. Eng.*, **23** [8] 913–935 (2003).

[11] R.U. Ayres and L. Ayres, *A Handbook of Industrial Ecology*. Edward Elgar Publishing, Northhampton, MA, 2002.

[12] *U.S Geological Survey, 2015, Mineral Commodity Summaries 2015: U.S. Geological Survey*. 2015.

[13] S.K. Bux, R.G. Blair, P.K. Gogna, H. Lee, G. Chen, M.S. Dresselhaus, R.B. Kaner, and J. Fleurial, "Nanostructured Bulk Silicon as an Effective Thermoelectric Material," *Adv. Funct. Mater.*, **19** [15] 2445–2452 (2009).

[14] R.L. Rudnick and S. Gao, "Composition of the Continental Crust," *Treatise on Geochemistry*, **3** 1–64 (2003).

[15] J. Yang and F.R. Stabler, "Automotive Applications of Thermoelectric Materials," *J. Electron. Mater.*, **38** [7] 1245–1251 (2009).

[16] S. Walia, S. Balendhran, H. Nili, S. Zhuiykov, G. Rosengarten, Q.H. Wang, M. Bhaskaran, S. Sriram, *et al.*, "Transition Metal Oxides – Thermoelectric Properties," *Prog. Mater. Sci.*, **58** [8] 1443–1489 (2013).

[17] S. Lee, J.A. Bock, S. Trolier-McKinstry, and C.A. Randall, "Ferroelectric-thermoelectricity and Mott Transition of Ferroelectric Oxides with High Electronic Conductivity," *J. Eur. Ceram. Soc.*, **32** [16] 3971–3988 (2012).

[18] S. Lee, R.H.T. Wilke, S. Trolier-McKinstry, S. Zhang, and C.A. Randall, "$Sr_xBa_{1-x}Nb_2O_{6-\delta}$ Ferroelectric-thermoelectrics: Crystal Anisotropy, Conduction Mechanism, and Power Factor," *Appl. Phys. Lett.*, **96** [3] 031910–1 – 031910–3 (2010).

[19] J.V. Hessen, B. Sunshine, S.A., Siegrist, T. Fiory, A.T., Waszczak, "Structure and Properties of Reduced Barium Niobium Oxide Single Crystals Obtained from Borate Fluxes," *Chem. Mater*, **3** [16] 528–534 (1991).

[20] J.R. Carruthers and M. Grasso, "Phase Equilibria Relations in the Ternary System BaO-SrO-Nb_2O_5," *J. Electrochem. Soc.*, **117** [11] 1426–1430 (1970).

Chapter 2

Literature Review

2.1 The Figures of Merit, zT and ZT

2.1.1 Two Thermoelectric Figures of Merit and Their Relation to Efficiency

A thermoelectric material's efficiency in converting waste-heat to electricity can be assessed by the dimensionless material figure of merit, zT. This figure of merit is given as:

$$zT = \frac{\alpha^2 \sigma T}{\kappa} \quad \textbf{(Eq 2.1)}$$

where α is the thermopower, σ is the electrical conductivity, T is the absolute temperature, and κ is the thermal conductivity[1]. This material figure of merit, which is applicable for a single material, must be distinguished from the device figure of merit, ZT. The device figure of merit can be related directly to the calculation of efficiency[1–3].

The operation of a thermoelectric power generator is analogous to that of a solid-state heat engine. Like all heat engines, the efficiency is bound by the ideal Carnot efficiency[1, 4, 5]. In such an engine, the processes are completely reversible, with no net increase in the entropy. The efficiency of this ideal engine depends on the amount of heat input and the useful work output, and thus only on the temperature difference as shown in Eq 2.2:

$$\eta_{Carnot} = \frac{P}{\dot{Q}} = \frac{T_H - T_C}{T_H} \quad \textbf{(Eq 2.2)}$$

where η_{Carnot} represents the Carnot efficiency, $\dot{Q}$ is the input heat flow rate, P is the output power, T_H is the temperature of the hot reservoir, and T_C is the temperature of the cold reservoir[5].

Figure 2-1 shows the electrical circuit formed by the thermoelectric generator and the load or device being powered.

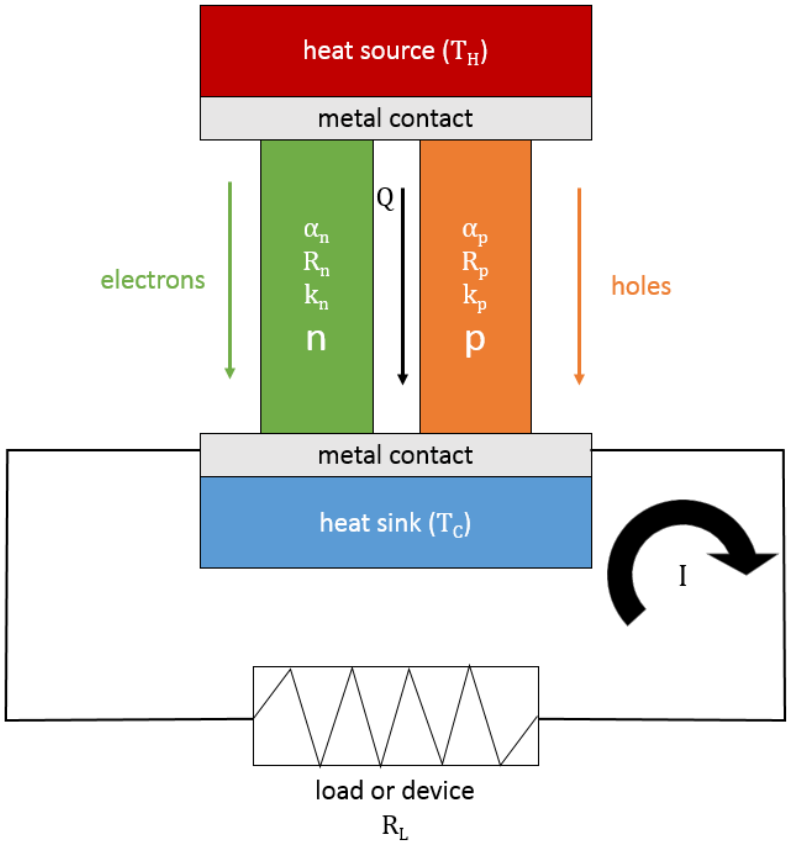

Figure 2-1. Thermoelectric generator (solid-state heat engine) electric circuit illustrating the transport processes involved. These processes can be used to derive the efficiency and its relation to ZT[5].

Using a simplified model where contact resistances are neglected and heat from the source is assumed to only flow through the legs (no leakage into the surroundings), Goldsmid derived a relationship between the efficiency, η, and ZT. ZT is the same for both refrigeration and power generation[5]. A brief overview is described below:

The thermoelectric current due to the Seebeck effect is given by:

$$I = \frac{\alpha \Delta T}{R} = \frac{(\alpha_p - \alpha_n)(T_H - T_C)}{R_p + R_n + R_L} \qquad \textbf{(Eq 2.3)}$$

where I is thermoelectric current, R is the resistance of the series circuit shown in Figure 2-1, and the subscripts p and n refer to the p-type and n-type leg of the thermoelectric generator, and L is the load or device being powered, respectively[5]. The power provided to the device can then be expressed as:

$$P = I^2 R_L = \left(\frac{(\alpha_p - \alpha_n)(T_H - T_C)}{R_p + R_n + R_L}\right)^2 R_L \quad \textbf{(Eq 2.4)}$$

which can be substituted in Eq 2.2[5].

The heat flow rate from the heat source can then be expressed as:

$$\dot{Q} = (\alpha_p - \alpha_n) I T_H + (K_p + K_n)(T_H - T_C) - \frac{1}{2} I^2 (R_p + R_n) \quad \textbf{(Eq 2.5)}$$

where the first term represents the heat being drawn from the source to balance the Peltier cooling, (using the Thomson relation in Chapter 1) the second term is the thermal conduction from the legs, where K is the thermal conductance, and the third term is the Joule heating, split between the two legs[6]. Substituting the current defined in Eq 2.3 into Eq 2.4 and Eq 2.5, and considering the efficiency defined in Eq 2.2, one eventually arrives at the conclusion that the ratio between the load resistance, R_L, to the resistance of the legs, (R_n+R_p), now defined as the variable M, is related to achieving maximum conversion efficiency:

$$\mathrm{M} = \frac{\mathrm{R_L}}{R_n + R_p} = (1 + Z T_m)^{\frac{1}{2}} \quad \textbf{(Eq 2.6)}$$

where T_m is the mean temperature, or half the sum of T_C and T_H[5, 6]. Increasing M will increase the efficiency, η. Supposing that Z is taken to be the thermocouple analog of z (i.e. such that minimizing the thermal conductivity and electrical resistivity is desirable), then a high efficiency implies that the total thermal conductance and the electrical resistance should also be minimized. Optimizing Z with consideration to the geometry of each leg, it can be shown that K and R are minimized if:

$$\left(\frac{\mathrm{A_n} l_p}{A_p l_n}\right) = \sqrt{\frac{\sigma_p \kappa_p}{\sigma_n \kappa_n}} \quad \textbf{(Eq 2.7)}$$

where A is the area, and l is the length of the legs[3,6]. Abiding by the conditions set by Eq 2.7, Z is then[5]:

$$\mathrm{Z} = \frac{(\alpha_\mathrm{p} - \alpha_\mathrm{n})^2}{\left((K_n l_n \rho_n l_n)^{\frac{1}{2}} + (K_p l_p \rho_p p)^{\frac{1}{2}}\right)^2} = \frac{(\alpha_\mathrm{p} - \alpha_\mathrm{n})^2}{\left(\left(\frac{\kappa_\mathrm{n}}{\sigma_n}\right)^{\frac{1}{2}} + \left(\frac{\kappa_\mathrm{p}}{p}\right)^{\frac{1}{2}}\right)^2} = M^2 - 1 \quad \textbf{(Eq 2.8)}$$

In terms of device functionality, Eq 2.4 shows that the maximum power output is achieved if the load resistance, R_L, is equal to the sum of the resistances of the legs, R_n and R_p. Figure 2-2 shows a plot of Eq 2.4; independent of the Seebeck coefficients and temperature terms and if $R_n = R_p = 10\,\Omega$. However, this then means that the maximum power point is not necessarily the maximum efficiency point, since Eq 2.6 asserts R_L should be large compared to the module's resistance. Lee has shown that this optimization discrepancy for high power and high efficiency is less than 3% for ZTs of around 1.0, but increases to 10% for ZTs larger than 3.0[6].

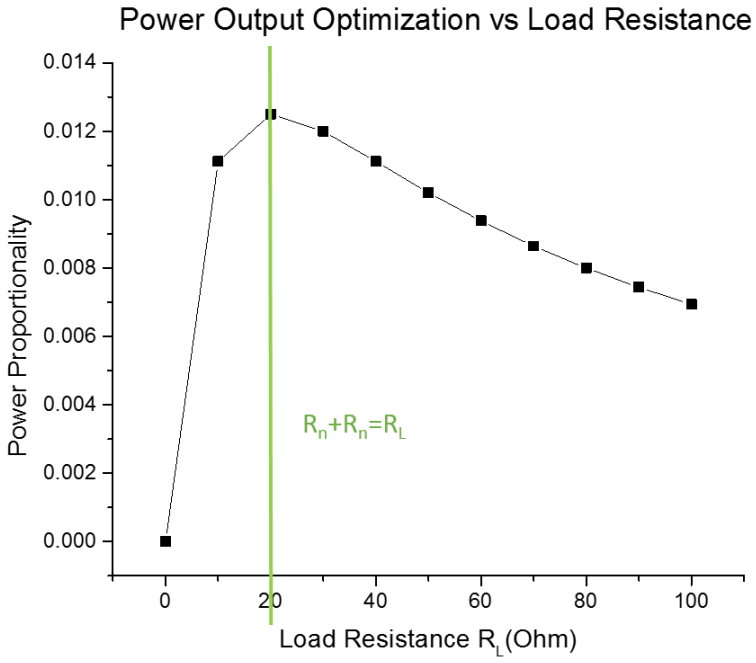

Figure 2-2. Proportionality of power output vs load resistance for a circuit where R_n and R_p both have a resistance of 10 ohms.

Finally, the expression for efficiency dependence on ZT is:

$$\eta = \frac{T_H - T_C}{T_H}\left(\frac{\sqrt{1+ZT_m}-1}{\sqrt{1+ZT_m}+\frac{T_C}{T_H}}\right) \qquad \textbf{(Eq 2.9)}$$

By taking ZT_m to very large values, Eq 2.9 simplifies to the Carnot efficiency. Figure 2-3 shows the efficiency plotted against ZT for three temperatures of the heat source if the heat sink is kept at a constant 300 K.

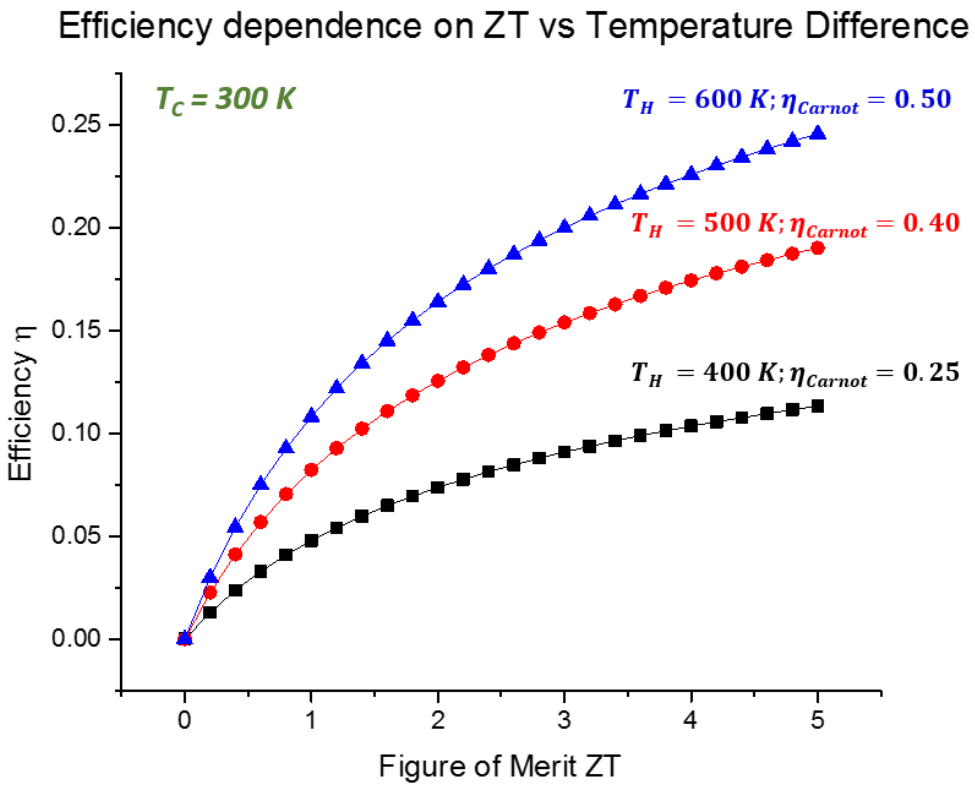

Figure 2-3. The efficiency of a thermoelectric device as a function of the ZT for a heat source at 600, 500, or 400 K, given that the heat sink is kept at 300 K. The Carnot efficiency is also shown.

It is of course, impractical to always pair a particular thermoelectric material with another of the opposite carrier type in order to assess the generator's efficiency. This is the rationale behind establishing the (single) material figure of merit zT. The relationship between z and Z is complex[2]. However, if the properties of the p and n-type materials are similar, and have similar temperature dependences, then an approximation for the relationship between Z and z is[3]:

$$Z \approx \frac{z_p + z_n}{2} \qquad \textbf{(Eq 2.10)}$$

If the n and p-type legs were exactly the same in terms of thermoelectric properties and temperature dependence, then the device Z is equivalent to the material z[1].

2.1.2 The Upper Bound of the Figure of Merit

There is still debate on the bounds of ZT, and consequently, the theoretical efficiency of a thermoelectric device. For example, Donahoe assumed that in the case where a low thermal conductivity of $0.01\frac{W}{m-K}$ could be achieved, a ZT of 5.1 at 300 K was possible[7]. On the other hand, Littman and Davidson state that the Seebeck coefficient increases with increasing band gap, E_g. Based on irreversible thermodynamics and the lack of a theoretical limit for the bandgap in semiconductors and insulators, they proposed that ZT had an upper-bound of infinity[8].

Goldsmid has agreed that theoretically, by the same bandgap argument, zT has no upper bound[3]. However, he states that band theory alone is not enough to justify this. In principle, one could achieve high zTs by maximizing the Seebeck coefficient if the material is assumed to obey the Wiedemann-Franz law relating the thermal conductivity to the electrical conductivity; it implies that a low carrier concentration would also provide low thermal conductivities. However, this law is only valid for metals. Therefore, enlarging the band gap alone will not necessarily enable zTs that approach infinity[3].

At the same time, materials that possess large Seebeck coefficients due to large band gaps have low electrical conductivities[3]. The lattice thermal conductivity would dominate the overall thermal conductivity in this case, since the electronic contribution to the thermal conductivity would be low. Goldsmid states that the thermal conductivity is dependent on a material's specific heat, the velocity of sound, and the mean free path of the phonon[3]. It was argued that the shortest mean free path should be on the order of interatomic spacing. Given this, Goldsmid predicted a lower-limit of $0.2\frac{W}{m-K}$ for the thermal conductivity, which is consistent with available data on non-porous bulk materials[3]. A zT of 4.1 was predicted and Goldsmid concludes that "it seems unlikely zT will exceed two" and "values of zT greater than four seem out of the question [3].

More recently, Nicolaou argued that if E_g approached infinity, the conductivity approaches zero and zT would be zero, and so from a standpoint of useful thermoelectrics, a limit to E_g should exist[9]. The figure of merit ZT can be expressed in an alternative

equation that factors the bandgap directly, plus a constant A[9]. Nicolaou claims to have evaluated a more accurate value of A, and concluded that the limit of ZT is 24.5[9]. A comprehensive overview of current and past arguments on the bounds of ZT is presented in this dissertation. Regardless of the upper limit, well-established thermoelectrics currently have a zT only slightly above unity.

2.1.3 Optimizing the Figure of Merit

The thermopower, electrical conductivity, and thermal conductivity are material properties that are a function of charge carrier concentration. In general, increasing the carrier concentration will: increase the electrical conductivity, increase the thermal conductivity, and decrease the thermopower. If electrons are the dominant carrier type, then the electrical conductivity can be expressed as:

$$\sigma = n(T)e\mu(T) \qquad \textbf{(Eq 2.11)}$$

where n is the carrier concentration, e is the elementary charge of an electron, and μ is the drift mobility of the carriers. Both the carrier concentration and mobility typically depend on temperature as noted in Eq 2.11. Likewise, the thermopower as well as the thermal conductivity are also dependent on temperature. These will be discussed in subsequent sections.

The carrier concentration for optimizing zT is usually in the range of $n = 10^{19}\ to\ 10^{20}\ \frac{carriers}{cm^3}$; with $10^{19}\ \frac{carriers}{cm^3}$ being more typical. One exception to this would be the layered oxide thermoelectric $NaCoO_2$ which has a carrier concentration on the order of $10^{21}\ \frac{carriers}{cm^3}$. [10] The general trend of zT as a function of carrier concentration with the trends of the electrical conductivity, thermal conductivity, and thermopower superimposed are shown in Figure 2-4. Heavily doped semiconductors meet this criteria and are unsurprisingly at the forefront of the thermoelectric field.

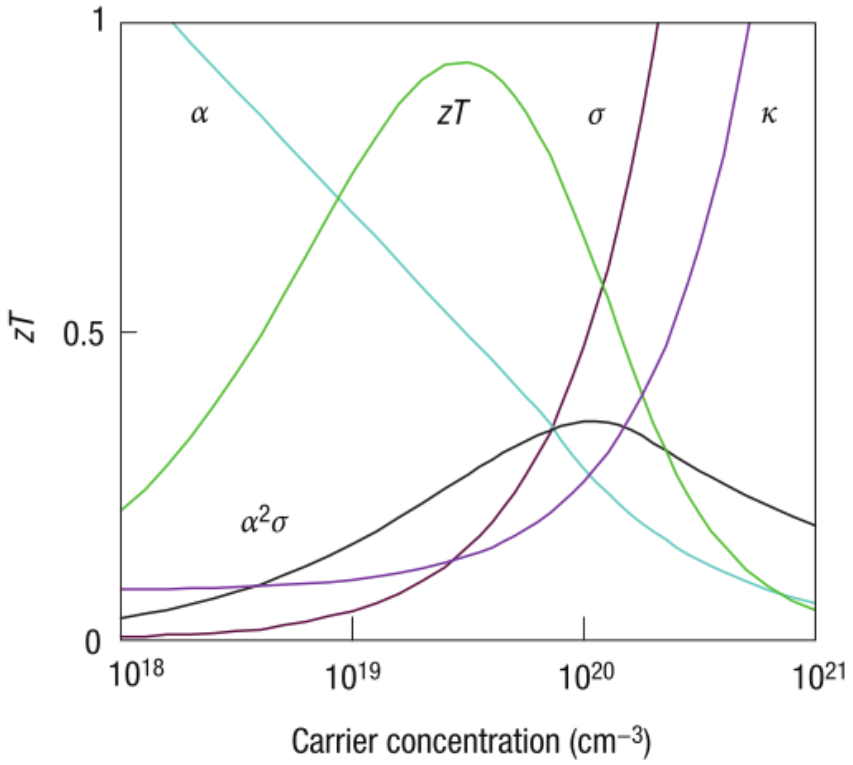

Figure 2-4. The variation of the thermopower, electrical conductivity, thermal conductivity, power factor and zT as a function of carrier concentration (Source: Snyder and Toberer)[1].

In so much that most useful thermoelectric materials all have in common this carrier concentration range, the zT will maximize at different temperatures for different materials as a result of the temperature dependence of the thermopower, electrical conductivity, and thermal conductivity. The temperature of the maximum zT governs the material's temperature of operation and its subsequent application. For example, waste heat recovery from a marine incinerator would require operating temperatures of at least 300°C[11].

The search for a good thermoelectric material therefore requires an unusual combination of properties. The contemporary model for achieving high zTs is the "phonon-glass, electronic crystal" first proposed by Slack[1, 12]. This viewpoint suggests engineering materials such that the thermal conductivity can be decoupled from the thermopower and the electrical conductivity. All state-of-the-art thermoelectrics share a commonality in that they possess low thermal conductivities[1]. To illustrate the importance of low thermal conductivity, consider the case of doped $SrTiO_3$. In the La-doped $SrTiO_3$ work by Okuda

et al., a power factor (the product of electrical conductivity and the square of the thermopower) of $36\frac{\mu W}{cm-K}$ was reported; this number is exceptional because this value rivals that of some of the best tellurides[13]. However, the thermal conductivity has a rather large value on the order of $10\frac{W}{m-K}$, which yields a zT that is only on the order of around 0.1[14]. One approach to novel thermoelectrics is to begin with a material system that already has a low thermal conductivity and then to tailor the electrical conductivity and thermopower. As a consequence, some of the contemporary research efforts have focused on optimizing the power factor, provided the material inherently possesses a low thermal conductivity[1].

2.2 Intermetallic Compounds and Non-oxide Thermoelectrics

2.2.1 Tellurides

The diversity of materials sold commercially as thermoelectrics is rather limited[1]. By far the most prominent is Bi_2Te_3[1]. As discussed in the introduction chapter, the high cost and rarity of tellurium provides an incentive to find new materials with high zT. Bi_2Te_3 is an example of a "phonon-glass electronic crystal," with a zT that ranges from 0.8 to 1.1 at temperatures of 273 to 473 K. Bi_2Te_3 is employed for both thermoelectric cooling and power generation, though more commonly the former due to its low operating temperature[15]. Bi_2Te_3 crystallizes in the rhombohedral system, consisting of two alternating layers of Te-Bi, and then a double Te layer[16]. A schematic of this structure is shown in Figure 2-5[17].

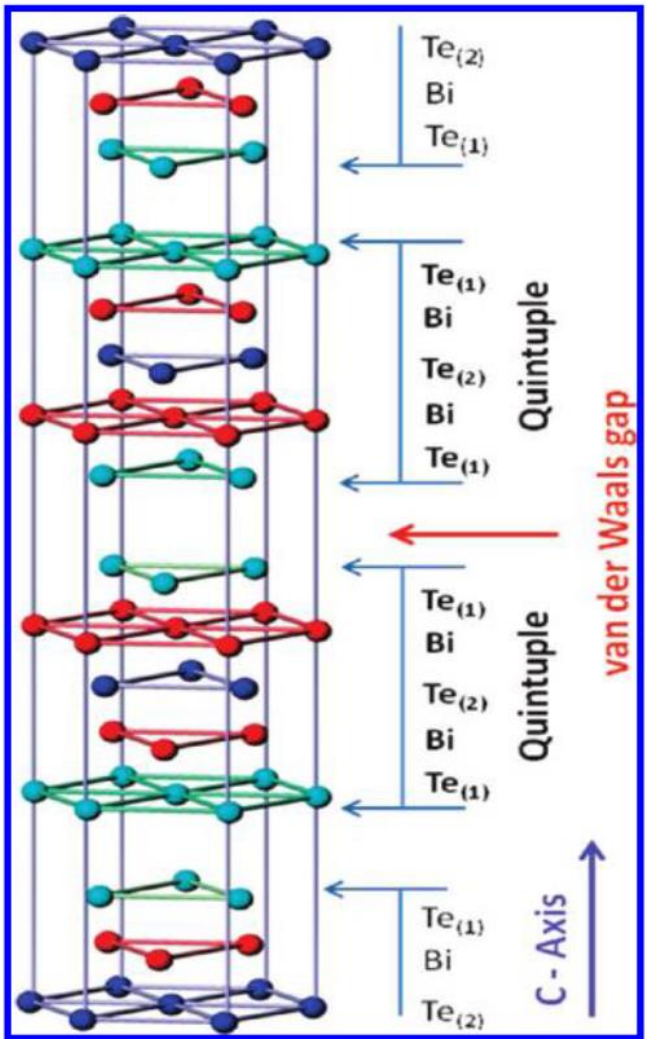

Figure 2-5. Schematic of the Bi and Te layers in Bi_2Te_3. Schematic taken from Teweldebrhan et al.[17].

The consequence of this complex unit cell is a low lattice κ due to phonon scattering[16]. The thermoelectric properties, S and σ are largest along the in-plane direction; σ being an order of magnitude greater here than the c-axis, and the thermal conductivity in this direction is on the order of 1.0 $\frac{W}{m-K}$ [16],[18].

Not all heavy-metal telluride compounds crystallize in the layered Bi_2Te_3-structure. One of these is the cubic PbTe. While the zT is not as high as that of Bi_2Te_3, it is useful in power generation in that its operating temperature is greater. Lately, there has

been extensive research into optimizing telluride chemistries by further reducing lattice thermal conductivity in the form of nanostructuring and/or alloying of these compounds[19].

2.2.2 Clathrates

Another class of important low-thermal conductivity thermoelectrics is the clathrates. The defining characteristic of clathrates as useful thermoelectric material is the large "cages" within the structure[1]. These large, open, cage-like structures allow atoms to "rattle," significantly decreasing the thermal conductivity.

The first type of clathrates, studied in the 19th century, were organic compounds of "ice" chlorine hydrates that exhibited several shapes of a large polyhedral cage[20]. Different geometries spurred the classification by of these materials by "type"[20]. It was found that these clathrates exhibited lower thermal conductivities than ice or water[20]. The logic behind clathrate thermoelectrics is primarily from the glass-like thermal conductivity resulting from the open-structure of the cage. When large atoms are placed within the cage, they scatter phonons effectively. The crystalline lattice making up the cage allows good electron mobility, resulting in high electrical conductivities[20]. Thermoelectric clathrates usually contain many large heavy atoms[21]. At least five useful types of clathrates have been actively researched, with some of the Type-VIII demonstrating zTs greater than unity with operating temperatures extending beyond that of Bi_2Te_3[21].

2.2.3 SiGe Alloys

Yet another important class of non-oxide thermoelectrics is SiGe. Both Si and Ge are well-known semiconductors that crystallize with the diamond cubic structure. As a consequence, pure Si and Ge suffer as thermoelectrics due to their high thermal conductivity. However, if alloyed together as a solid solution, the thermal conductivity can be decreased, almost by a factor of 5[15, 22]. Microstructural engineering, such as controlling grain boundaries, can further lower the thermal conductivity[22]. Doping SiGe allows tuning of the carrier concentration and further reductions in the thermal conductivity[22]. Vining has shown that n-type SiGe has a zT of around unity, while the p-type variant has a zT only

about half of this[22]. Despite the low zT on the p-type, SiGe remains relevant to thermoelectric applications because its operating temperature is among the highest of all thermoelectric materials. This makes it ideal for radioisotope thermoelectric generators, which are frequently used in spacecrafts as a long-lasting and reliable power source[23].

Table 2.1 shows, in ascending order of general operating temperature, some of the highest zT non-oxide thermoelectrics that have been reported[1, 19, 21, 22, 24–28].

Table 2.1 zTs of Non-oxide Thermoelectrics

Material	Carrier Type	Operating Temperature (K)	zT	Reference
$BiSb_4Te_{7.5}$	p	300	0.99	24
(p) Bi_2Te_3	p	375	1.00	1
(n) Bi_2Te_3	n	375	1.00	1
Bi_2Te_2Se	p	400	0.90	24
Bi_2Te_3-$74Sb_2Te_3$	n	423	1.27	25
Bi_2Te_3-$25Bi_2Se_3$	p	423	1.14	25
(p) ZnSb	p	448	0.63	24
Type-VIII $Ba_8Ga_{16}Sn_{30}$ (clathrate)	p	480	0.90	21
$AgSbTe_2$	p	673	0.87	24
$La_{0.7}Ba_{0.1}Ga_{0.1}T_{i0.1}Fe_3CoSb_{12}$ (thin film skutteruddite)	n	723	0.75	26
(n) PbTe	n	723	0.94	19
TAGS (two-phase AgSbTeGeTe)	p	773	1.20	27
SnSe	p	900	2.50	28
InAs	n	973	0.68	24
(p) SiGe	p	1123	0.51	22
(n) SiGe	n	1173	1.04	22

2.3 Thermoelectric Oxides

2.3.1 General Considerations in Oxide Thermoelectrics

The number of high-performing oxide thermoelectrics material types is low relative to the non-oxides. In general, most oxides possess high lattice thermal conductivities, owing to their strong, mixed ionic and covalent bonds[10]. The electrical conductivity of many oxides are lower than typical semiconductors as a consequence of lower carrier mobilities[10]. In cases where an oxide does have high mobility, such as In_2O_3, the effective mass of the carrier is small and leads to low Seebeck coefficents[10]. Despite somewhat lower zTs however, a major attraction of oxides is their sustainability and their high operating temperatures for power generation. It was only after the discovery of $NaCo_2O_4$ as a high zT thermoelectric that oxides could be considered relevant to the field[5, 29].

The majority of thermoelectric oxides are transition metal oxides. This is not too surprising, since multiple valence states allow for low-energy electronically compensating dopants. For instance, consider the example of Ca-doped NaCl provided by Smyth[30]. In NaCl, in which the conduction band can be thought of as arising from the Na^+ ions. It is energetically unfavorable to excite electrons into the Na^+ conduction band of NaCl because such a situation calls for Na^+ become a neutral Na atom. In such a highly ionic compound, Na prefers to stay as Na^+. Therefore, the compensation is almost always ionic in this case[30]. In cases of non-binary transition metal oxides, there is considerable flexibility in ways to introduce non-stoichiometry in order to either tune the carrier concentration or incorporate defects that lower the thermal conductivity. A brief overview of some of the most studied oxides is given here. Because of the importance of $NaCo_2O_4$ in pioneering the way for thermoelectric oxides, more emphasis will be devoted to this material.

2.4.2 The Layered Cobaltites

$NaCo_2O_4$ (sometimes written as Na_xCoO_2) currently is the champion p-type oxide after the discovery of its high thermoelectric performance by Terasaki et al. in 1997[31]. This layered cobaltite crystallizes in a trigonal space group, and shares some resemblance to

some of the copper oxide high-temperature superconductors [29, 32] . The motif of the structure is an alternating stack of Na (with 50% occupancy), and blocks of CoO_2 that resemble the hexagonal close-packed structure of CdI_2, with the Co octahedrally-coordinated to the oxygen [29]. The layers stack in the direction of the c-axis. As with Bi_2Te_3, the anisotropic structure reflects the anisotropy in the material, with superior thermoelectric properties along the plane of the layers[33]. The structure of this cobalt oxide was refined by single crystal diffraction by Takahashi et al., and a more complete treatment of its crystal structure can be found in his work [32].

With a zT of around unity at 800 K in the single crystal, this material features a high power factor and a low thermal conductivity[34]. However, there are some distinct features of this material unlike those of other thermoelectrics. First is its unusually high zT of 0.8 as a polycrystalline ceramic as reported by Ito et al.[35]. Second, is the exceptionally high carrier concentration in this material. From Figure 2-3, it was shown that for many thermoelectrics, (including PbTe) [19] $1.0 \times 10^{19} \frac{carriers}{cm^3}$ is the optimum. As reported by Terasaki, the carrier concentration for $NaCo_2O_4$ is on the order of $10^{21} - 10^{22} \frac{carriers}{cm^3}$.[10] According to the Mott Criterion an metal-insulator transition can be characterized by the Bohr radius (thought of as a sphere of interaction between charge carriers) and the carrier concentration[36]. It is expressed as:

$$n^{\frac{1}{3}} a_h \cong 0.25 \qquad \textbf{(Eq 2.12)}$$

where n is the carrier concentration and a_h is the Bohr radius of a material. If this product exceeds 0.25, then the material is expected to be either metallic or a degenerate semiconductor[36]. Many papers discuss optimization of zT by engineering the carrier concentration just on the semiconducting side of the metal-insulator transition. With a carrier concentration two orders of magnitude larger than what is expected for the zT optimization, $NaCo_2O_4$ is a metal and would therefore be expected to have low thermopowers. While $NaCo_2O_4$ possesses metallic conductivity, its thermopower has been decoupled from the electrical conductivity and remains at a relatively high value of $100 - 150 \frac{\mu V}{K}$ [31].

Two different models have been proposed to describe the unique behavior of $NaCo_2O_4$. The first was established by Singh et al, which entails a band structure calculation exploring a delocalized band structure with "pockets" in the valence band to rationalize the large Seebeck coefficient[37]. The second model was proposed by Koshibae et al.; this model gives a localized picture that explores the degeneracy of the spin state of the Co ions as a result of the mixed oxidation states (Co^{3+} and Co^{4+}) as well as the crystal field splitting into the e_g and t_{2g} states [38]. For the Co^{4+} ions in the structure, the t_{2g} states are completely filled, resulting is no other degenerate state. For the Co^{3+}, 5 electrons fill the three t_{2g} orbitals, leaving one empty state. The vacancy can occupy any of the 6 states and still give the same energy; these 6 arrangements yields 6 degenerate states, which can be thought of as an entropy contribution. By calculation with a modified Heike equation, the thermopower was calculated to be $150\frac{uV}{K}$, which is true experimentally at 1000 K[10]. A more detailed description of these models is given in references 16, 40, and 41. The thermopower and its entropy relation and the Heike equation will be discussed further in section 2.6.

The success of $NaCo_2O_4$, has led to the exploration of other layered cobaltite systems with the same principle in mind. One of these is $Ca_3Co_4O_9$. The structure is very similar to that of the Na compound, but its unit cell consists of alternating CoO_2 and three layers of a distorted rock-salt structure, as opposed to just the single layer of Na as found in $NaCo_2O_4$ [33]. Other layered cobaltites, including a bismuth variant, have been synthesized that yield similar zTs near unity or higher[39].

2.4.3 Other Oxides

ZnO is among one of the most studied oxide thermoelectrics, unique in the fact that it is a binary compound. Power factors for this material range from $8-15\frac{\mu W}{cm-K^2}$ (room temperature to ~1000 K), which is lower than that of Bi_2Te_3 by a factor of about 2.5[40]. The performance of ZnO suffers due to its high thermal conductivity. However, the thermal conductivity has been shown to decrease with increasing temperature, from about $\sim 40\frac{W}{m-K}$

at ambient to $\sim 5 \frac{W}{m-K}$ at 1000 K[40]. ZnO as a thermoelectric has been extensively studied by Ohtaki et al.[41]. As an nonvolatile oxide, its high operating temperature makes ZnO a promising candidate for power generation applications, where a zT of 0.65 has been reported[41]. Further increases in the power factor by magnetically texturing have been extensively studied by Kaga et al.[42]. and a comprehensive review of nanostructuring and other efforts to lower the thermal conductivity is covered by Wang[43–45].

Oxides that crystallize in the perovskite structure have also been investigated as potential thermoelectrics. Carrier concentrations can be tuned by doping due to the high tolerance of the perovskite structure. Several groups have investigated $SrTiO_3$ as a high temperature thermoelectric [13, 46, 47]. Okuda et al. and Ohta et al. have shown that La-doped $SrTiO_3$ boasts an impressive power factor of $23 - 36 \frac{\mu W}{cm-K^2}$ near room temperature[13, 47]. Despite high power factors, the thermal conductivities of heavily La or Nb-doped $SrTiO_3$ are high, about $9.1 - 12.0 \frac{W}{m-K}$, resulting in zTs below 0.1 in this temperature range[47]. Ohta has shown that the thermal conductivity decreases with temperature, such that at 1100 K, the thermal conductivity decreases to about $2.5 \frac{W}{m-K}$ for both La and Nb-doped $SrTiO_3$[47]. However, at this high temperature, the power factor suffers and decreases to $\sim 9 \frac{\mu W}{cm-K^2}$, resulting in a zT of about 0.20[47]. Efforts to reduce the thermal conductivity while preserving the power factor in $SrTiO_3$ thin films resulted in a zT of 0.27 at 875 K[48]. Using a novel monolithic module based on a multilayer ceramic capacitor design, Funahashi et al. had reported a zT of ~ 0.37 at 750 K in La-doped $SrTiO_3$ thermoelectric modules manufactured by Murata Manufacturing Ltd.[49].

Additionally, the perovskite $BaTiO_3$ has been studied by Lee et al.. Oxygen-deficient-$BaTiO_3$ was investigated alongside $SrTiO_3$ to study the effects of ferroelectricity on thermoelectricity[46]. In this work, annealing at different oxygen partial pressures was used to control the concentration of negative charge carriers from compensation of oxygen vacancies. Using the enthalpy of formation for oxygen vacancies for this system, the carrier concentration was calculated to be on the order of $10^{19}\ to\ 10^{20}$ per cm^3, which is the same as that reported in the La and Nb-doped $SrTiO_3$ by Ohta et al.[47]. $BaTiO_3$ has large

thermopowers, on the order of $400\frac{\mu V}{K}$ at 550 K, but the electrical conductivity is only on the order of $10\frac{S}{cm}$, resulting in lower power factors[46].

Due to the sheer number of transition metal oxides, many of the other oxide thermoelectrics are not discussed here. However, the cobaltites, ZnO, and $SrTiO_3$ have so far yielded the highest reported zTs. A comprehensive review of other thermoelectric oxides has been given by Walia et al. in reference 40 [40]. Table 2.2 shows some of the high zT oxides that have been reported in descending order of zT. Comparing Tables I and II reveal that there is currently a dearth in competitive oxides.

Table 2.2 zTs of Some Oxide Thermoelectrics

Material	Carrier Type	Operating Temperature (K)	zT	Reference
$Bi_2Sr_2Co_2O_8$	p	100	1.15	39
Na_xCoO_2	p	800	1.00	34
Na_xCoO_2 (ceramic)	p	1000	0.80	35
$Zn_{0.98}Al_{0.02}O$	n	1073	0.65	41
$Sr_{1-x}La_xTiO_3$ (thin film)	n	875	0.35	48
$Sr_{1-x}La_xTiO_3$	n	600-750	0.20-.37	47 and 49

2.5 Electrical Conductivity

2.5.1 Introduction

The electrical conductivity is the material property that represents the ease with which a current of charge carriers can flow under an applied potential. With the exception

of superconductors, (which do not exhibit the Seebeck Effect) all materials will oppose this flow in some way. This results in Joule heating. One reason that the electrical conductivity appears in the figure of merit is because Joule heating needs to be minimized such that a temperature gradient is maintained during operation [4].

The electrical conductivity was given in Eq 2.11. Though Eq 2.11 defines the conductivity. The temperature dependence of the conductivity is a function of the band structure of the material. Even a qualitative picture of the band structure is useful for predicting and modeling the electrical conductivity and thermopower trends of a material. Roughly, the conduction mechanisms can be divided into two classes. Wood has designated these two classes as "wide-band" or itinerant conduction and "narrow-band" or hopping conduction[15]. Here, the two classes will be referred to as "high-mobility conductors" (band conduction) and "low mobility conductors" (hopping conduction), respectively.

2.5.2 Metals (High Mobility)

The simplest model of the electrical conductivity pertains to the conduction found in metals. It is best described by the Drude model, which depicts a sea of delocalized electrons that are free to move under an applied field; the vibrating positive ion cores which act as scattering centers[50]. The mobility in Eq 2.11 can be related to a mean free time between scattering events, τ:[50]

$$\mu(T) = \frac{e}{m_e}\tau \qquad \textbf{(Eq 2.13)}$$

where e is the elementary charge and m_e is the effective mass of an electron. The effective mass accounts for the inertial resistance to electron acceleration due to the periodicity of the crystal and varies for different materials[50]. The amplitude of the atomic vibrations are proportional to the average kinetic energy (and thus approximately to temperature). Thus, it can be shown that τ is inversely proportional to temperature. Substituting such an expression back into Eq 2.11, yields:

$$\sigma = \frac{A}{T} \qquad \textbf{(Eq 2.14)}$$

where A is a collection of constants that include n, e, and m_e[50].

In metallic lattices, the outer atomic orbitals, both full and empty, have significant overlap at the atoms' equilibrium separation distance, r_0[51]. As a consequence, metals are characterized by their lack of forbidden energy states and so states exist immediately above the Fermi energy that electrons can occupy. As a result, metallic conductors have a large number of carriers with rather high mobility, resulting in high electrical conductivity even at room temperature and below. The mobility decreases with increasing temperature due to increased vibrations of the atoms as depicted in Eq 2.13, and so metals usually possess a negative temperature coefficient of resistivity.

2.5.3 Semiconductors (High Mobility)

Band-type semiconductors are also high mobility conductors. Unlike metals, a plot of the outer atomic orbital energies vs. the atom spacing shows that the bands do not overlap at the equilibrium separation distance. The result is a forbidden energy band gap, E_g, where no states are available for electrons to occupy[52]. For *intrinsic semiconductors*, conduction electrons must come from the filled valence band and be excited by an energy greater than E_g into the conduction band, where the electron is delocalized. For every electron promoted to the conduction band, an empty state is left behind in the valence band, called a hole. The hole acts as a positive charge carrier and is delocalized in the valence band. This results in the creation of two carriers that are created by a thermal activation process, with $n_i = p_i$, where n and p are the concentration of mobile electrons and holes, respectively, and the subscript i denotes intrinsic.

It can be shown that this activation process obeys an Arrhenius relationship with respect to temperature. To derive this, one must consider the density of states, $g(E)$, and the Fermi-Dirac distribution, $f(E)$. A non-rigorous treatment is given here. The density of states represents the number of states per unit energy per unit volume. The distribution of energy states within a band comes from a linear combination of x different electron wave functions if there are x atoms in the crystal[50]. Kasap gives a "coin-flip" analogy to demonstrate the distribution of energy states within a band. If there are 10 coins (atoms), then one will find that only one combination will give 10 tails or 10 heads, while several

combinations will yield 5 heads and 5 tails; the number of combinations being the analog of the number of states[50]. Thus, when considering the energy boundaries of a band (bottom of the band to top of the band), one would expect a distribution that shows a greater number of states of energies that are in the central region of the band. $g(E)$ is $\sim \propto m_e^{\frac{3}{2}} E^{\left(\frac{1}{2}\right)}$, but with the caveat that as $E \rightarrow E_{top\ of\ band}$, $g(E) \rightarrow zero$[50].

The Fermi-Dirac distribution, $f(E)$, is also a function of energy, E, and describes the probability that an electron occupies a state with energy, E. Unlike the Boltzmann distribution, $f(E)$ accounts for the Pauli Exclusion Principle. Intuitively, one would expect that increasing the temperature would increase the probability of finding an electron at a higher energy state. $f(E)$ then has the form:

$$f(E) = \frac{1}{1 + \exp\left(\frac{E - E_F}{k_b T}\right)} \qquad \textbf{(Eq 2.15a)}$$

where k_b is the Boltzmann constant, E is the energy, and E_F is the Fermi Energy[52]. It is noted from Eq 2.14a, that the probability of an electron to occupy a state with the Fermi Energy is ½.

Integrating the product of $g(E)$ and $f(E)$ will give the density of the carriers. For electrons in the conduction band:

$$n_i = \int_{E_{bottom\ of\ band}}^{E_{top of\ band}} g(E) f(E) dE \qquad \textbf{(Eq 2.16)}$$

A schematic for deriving the electron concentration for a semiconductor is shown in Figure 2-6. Evaluating Eq 2.16 gives the carrier concentration that can be applied to Eq 2.11 for the electrical conductivity.

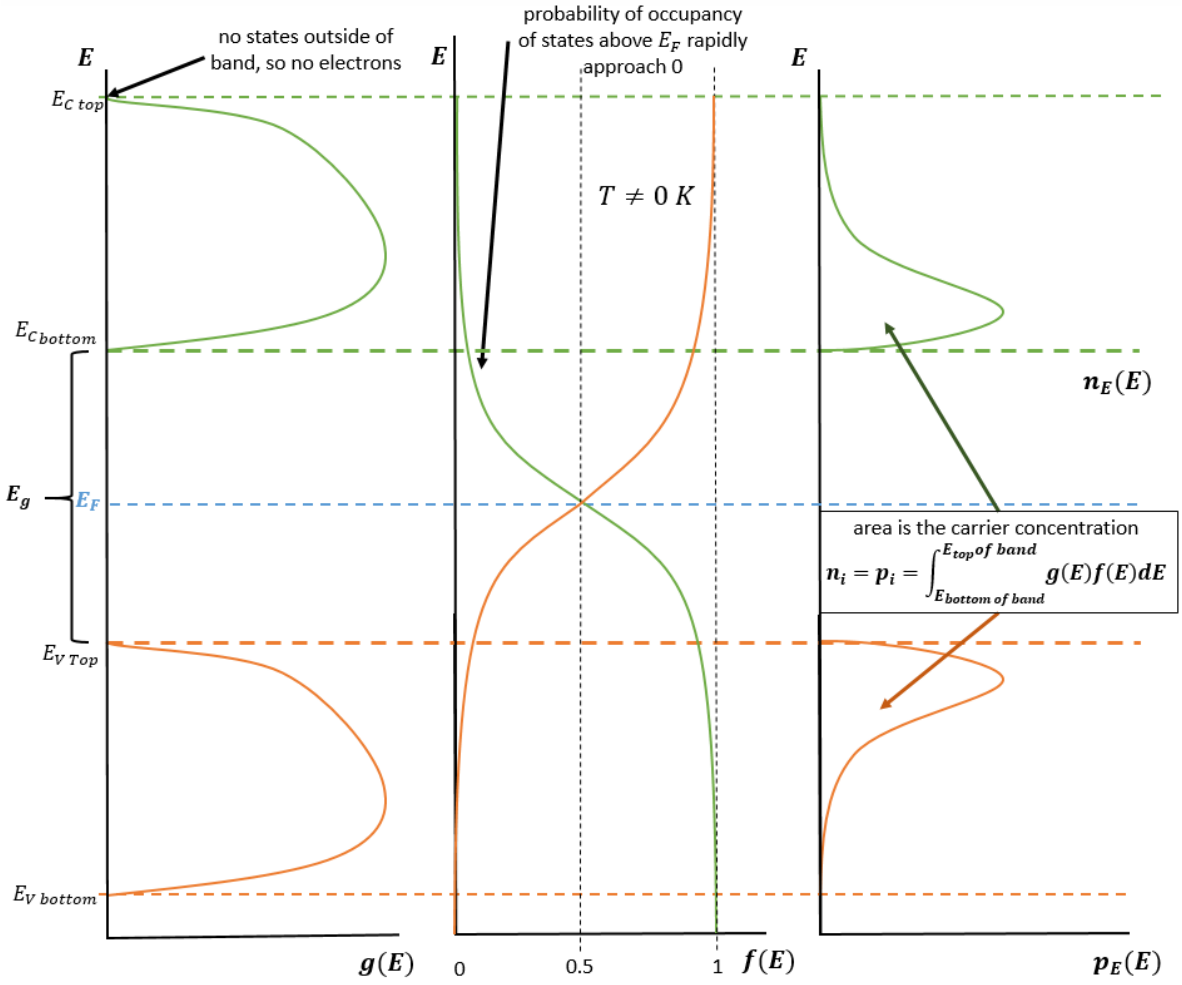

Figure 2-6. Band structure for intrinsic semiconductor, showing the relationship between the density of states $g(E)$, the Fermi-Dirac function $f(E)$, the electron (green) and hole (orange) concentration for a particular energy per unit volume $n_E(E)$, and carrier concentration, n_i (Adapted from Kasap[50].)

Eq. 21 can be more readily evaluated with a few simplifications and assumptions. At low temperatures (room temperature, for example) such that $k_bT \ll E - E_f$, the "1" term becomes negligible in Eq 2.14a and so this probability factor simplifies to the Boltzmann expression[53]:

$$f(E) = \exp(-\frac{E - E_F}{k_bT}) \qquad \textbf{(Eq 2.15b)}$$

This approximation is valid if the number of carriers is much less than the number of states in the band, where accounting for the Pauli Exclusion Principle will not appreciably affect the results[52]. Two more simplifications can be applied to simplify Eq

2.16. In regards to the energy, it is assumed that excited electrons and holes take on energy values corresponding to the edges of the conduction band and valence band, E_C and E_V, respectively. This is justified from Figure 2-6 showing that for a small number of carriers compared to the number of states, carriers will fill the many states near the edges of the band first. The band gap E_g, is simply $E_C - E_V$. The activation energy for electrons and holes would be $E_C - E_F$ and $E_F - E_V$, respectively. It is also noted that the upper bound of the integral in Eq 2.15 can be substituted with infinity so that the integration takes on a simplified form with little effect on the result, since the probability drops rapidly for energies beyond the Fermi energy[53].

Evaluating Eq 2.15 for electrons with the three above simplifications yields an Arrhenius form for the electron concentration:

$$n_i = N_C \exp(-\frac{E_C - E_F}{k_b T}) \qquad \textbf{(Eq 2.17)}$$

where $N_C \approx 1.0 \times 10^{-19} cm^3$ is a collection of terms from $g(E)$, and represents an effective density of states at the conduction band edge[50, 52]. A similar argument is given for the concentration of holes, where $N_V \approx 1.0 \times 10^{-19} cm^3$ would be the effective density of states for the valence band edge. It is noted that $N_C = N_V = N$.Since $n_i = p_i$ then:

$$n_i^2 = p_i^2 = n_i p_i = N_C N_V \exp\left(-\frac{E_C - E_F + E_F - E_V}{k_b T}\right) \qquad \textbf{(Eq 2.18)}$$

Since $E_g = E_C - E_V$, simplifying Eq 2.17 shows that the activation energy for carriers is half the bandgap:

$$n_i(T) = p_i(T) = N \exp\left(-\frac{E_g}{2k_b T}\right) \qquad \textbf{(Eq 2.19)}$$

The electrical conductivity in Eq 2.11 then takes on the form:

$$\sigma_i = n_i(T) e \mu_e(T) + p_i(T) h \mu_h(T). \qquad \textbf{(Eq 2.20)}$$

The mobility dependence should be similar to that of Eq 2.13. With this, the Arrhenius relation for conductivity with respect to temperature is justified.

The *extrinsic* semiconductor case follows the same logic, where the only difference is that an impurity level is introduced. The energies of the dopant states lie within the band gap of the intrinsic material and close to the conduction band edge or to the valence band

edge for n-type and p-type, respectively. The presence of states within the band gap drastically lowers the activation energy of carriers relative to intrinsic conduction. This is shown in Figure 2-7, which is a simplified band structure of an extrinsic semiconductor.

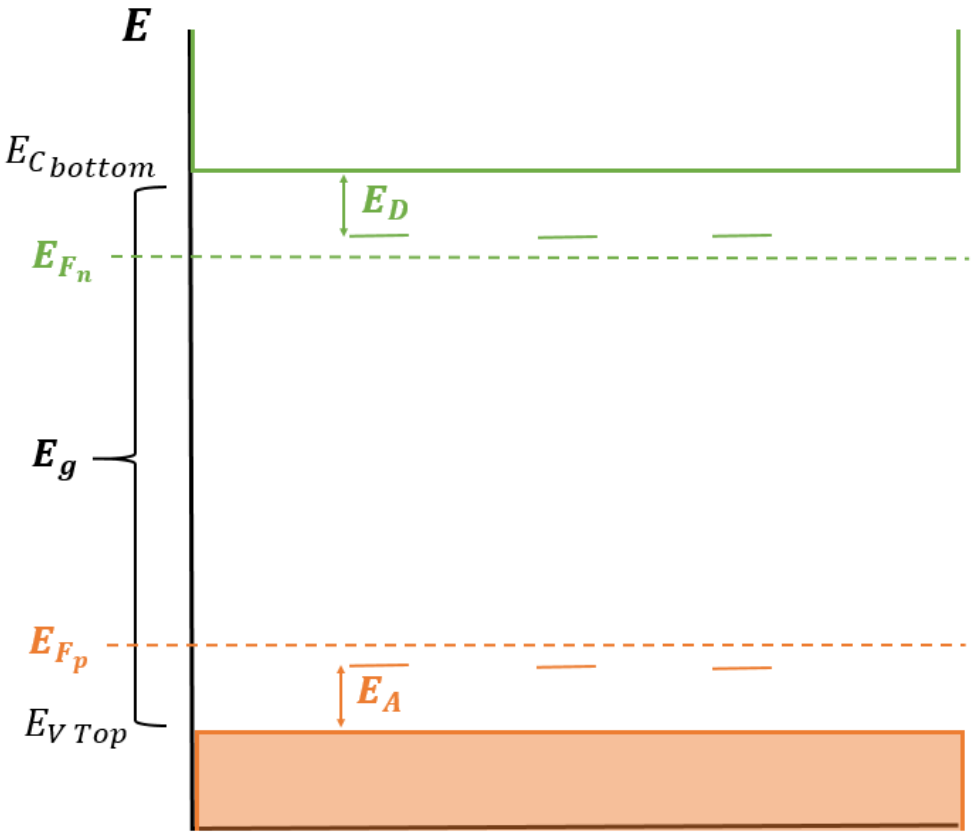

Figure 2-7. Simplified band diagram for an extrinsic semiconductor showing several isolated dopant states. Note that the location of the Fermi level, E_F is dependent on the carrier type as well as temperature.

The activation energy for *intrinsic* semiconductors was half the bandgap, as shown previously. Typical semiconductors have a bandgap of about $1.0 - 3.5\ eV$[52]. For extrinsic conduction, the activation energy from donors (n-type) or acceptors (p-type), E_D and E_A, respectively, usually falls between $0.02\ to\ 0.1\ eV$[52]. This means that even at ambient temperatures, there is enough thermal energy to excite these carriers into a conduction band. For an n-type semiconductor, the mobile electron concentration is much greater than the mobile hole concentration, and so

$$\sigma_n \approx n(T)e\mu_e(T) \quad \textbf{(Eq 2.20)}$$

where the subscript n denotes n-type. The converse is true for p-type semiconductors. Extrinsic conduction obeys the same Fermi-Dirac statistics, with only minor modifications[50]. In essence, the conduction will still obey an Arrhenius relationship. Once carriers reach the conduction or valence band, they are essentially delocalized, and free to conduct throughout the crystal.

2.5.4 Hopping Conductors (Low Mobility)

In many transition metals compounds, particularly their doped oxides, the d-orbitals can change the conducting behavior. In these low-mobility materials, a hopping mechanism dominates the conduction. The simplest model of a hopping conductor is described by the presence of multiple oxidation states for the transition metal ions, where (for example) an electron can sit on ion A (e.g. Nb^{4+},) and "hop" to an adjacent ion B (e.g. Nb^{5+}). The conduction is not delocalized as in the case of the high-mobility semiconductors. As a consequence, these materials possess low mobilities ($\approx 0.1 \frac{cm^2}{V-s}$) compared to that of metals or traditional semiconductors ($\approx 1.0 \times 10^3 \frac{cm^2}{V-s}$). [15, 52]

One important distinction is that for hopping conductors, the carrier concentration may be fixed by the dopant concentration, provided the temperature is not sufficient for intrinsic conduction. That is, each dopant typically provides one localized carrier which is trapped and not in a band. The trapping is a result of the polarization of the transition-metal oxide lattice caused by the local charge carrier[54]. Because of this, hopping carriers are also known as polarons[54].

The hopping occurs if the carrier can overcome the barrier of the trap[15]. The probability of hopping is correlated with the mobility. The electron may not move far, and it may be trapped again after a single hop. The result is a material with a high concentration of carriers that is temperature-independent, with low mobilities that are thermally activated[52, 54]. There are several flavors of hopping; two of which will be reviewed briefly:

the case of nearest neighbor hopping where the electron does not hop back into its original trap, and that of variable-range hopping.

Wood provides a model for the electrical conductivity given by the hopping mechanism for nearest neighbors[15, 25]. The final equation is:

$$\sigma_{\mathrm{nnh}} = \frac{\mathrm{c}(1-\mathrm{c})\mathrm{e}^2}{ak_bT}[\tau_0^{-1}\exp\left(\frac{-E_\mu}{k_bT}\right)] \qquad \textbf{(Eq 2.21)}$$

where the subscript nnh refers to "nearest-neighbor hopping". The terms, c and $(1-c)$ represent the concentrations of the lower valence and higher valence states of the transition metal ion, respectively. These two terms thus represent the charge carrier concentration, usually in parts per hundred or thousand. The term a is the hopping distance, usually on the order of a lattice constant; τ_0^{-1} is a pre-exponential term describing the probability for hopping; and E_u is the activation energy for hopping[15, 54]. Eq 2.21 is commonly shown in simplified form[55]:

$$\sigma_{\mathrm{nnh}} = \frac{\sigma_0}{T}\exp\left(\frac{-E_\mu}{k_bT}\right) \qquad \textbf{(Eq 2.22)}$$

As shown in Eq 2.22, plotting $\ln(\sigma_{nnh}T)$ (rather than simply $\ln(\sigma)$ for the band conductors) vs $\frac{1}{T}$ will give the activation energy. Increasing the dopant concentration generally decreases the activation energy and at sufficiently high dopant levels, the material may become metallic, which is consistent with the Mott criterion[54]. An example is found in $La_{1-x}Sr_xVO_3$ in which the activation energy steadily decreases with increasing x and falls to 0 at $x \approx 0.2$[54].

Variable-range hopping is similar to the hopping process outlined above except that the hopping distance may extend beyond the nearest neighbor. This is generally valid for materials with significant disorder, where nearest neighbors are not necessarily the lowest energy barriers for charges to move onto. Variable range hopping is often observed in amorphous materials[56]. Lewis gives the expression for the variable-range hopping model as

$$\sigma_{\mathrm{vrh}} = A\exp\left(\frac{-T_0}{T^{\frac{1}{4}}}\right) \qquad \textbf{(Eq 2.23)}$$

where the subscript "vrh" stands for variable-range hopping, and both A and T_0 are constants[56].

It is noted by Cox and Wood that variable-range hopping generally occurs at low temperatures (typically <77 K)[15, 54]. Fitting a system to the variable range-hopping mechanism is difficult. Some materials have an electrical conductivity that may fit a $T^{-\left(\frac{1}{4}\right)}$ dependence, but also have a temperature-independent thermopower, in contradiction with the model of a variable-range hopping conductor[56].

Gorham-Bergeron and Emin note that at temperatures below half the Debye temperature, a $T^{-\left(\frac{1}{4}\right)}$ dependence of the electrical conductivity may also exist in certain materials as a result of "non-activated" hopping. Below half the Debye temperature, there are few high energy phonons that assist in the hopping process[57, 58]. A more detailed analysis can be found in both Emin and Mott's work (references 57, 58, and 61.) A $T^{-\left(\frac{1}{4}\right)}$ dependence may also fit a hopping conduction as detailed by Emin[57].

Disorder is another factor that should be considered in the localization of charge carriers. As will be discussed in the section regarding strontium barium niobate (SBN), the band structure may be modified via mobility edges as a consequence of Anderson localization in high-disorder systems[54]. This was explored in the work of Bock et al..[59] Materials may not strictly follow any one model described above, and there are often transitions between regimes as a function of temperature.

2.6 Thermopower (Seebeck Coefficient)

2.6.1 Introduction

The thermopower is usually expressed as the potential that arises from a temperature gradient. However, the thermopower is more fundamentally an expression of the entropy per charge carrier, as described by Terasaki[10]. The current density, j, and thermal current density, q, are given by[10]:

$$\mathrm{j} = \sigma(-\nabla \mathrm{V}) + \sigma\alpha(-\nabla \mathrm{T}) = \sigma \mathrm{E} + \sigma\alpha(-\nabla \mathrm{T}) \quad \textbf{(Eq 2.24)}$$

$$\mathrm{q} = \sigma\alpha \mathrm{T}(-\nabla \mathrm{V}) + \kappa_0(-\nabla \mathrm{T}) = \sigma\alpha \mathrm{TE} + \kappa_0(-\nabla \mathrm{T}) \quad \textbf{(Eq 2.25)}$$

In the above equations, $-\nabla \mathrm{V} = \mathrm{E}$ is the applied electric field and κ_0 is the thermal conductivity at no electric field. The first term in equations 29 and 30 are the charge carrier contributions to the current density (Ohm's law), and thermal current density, respectively. The secondary terms in Eq 2.24 and Eq 2.25 represent the net movement of carriers under a temperature gradient (similar to Seebeck effect) and thermal conductance by phonons, respectively. If the temperature gradient, $-\nabla T$, is set to 0, then the only contributions to Eq 2.24 and Eq 2.25 come from the charge carriers. Solving for the electric field in Eq 2.24 after setting $-\nabla T = 0$ and substituting into Eq 2.25, and rearranging gives:

$$\frac{\mathrm{q}}{T}\left(\frac{1}{j}\right) = \alpha \quad \textbf{(Eq 2.26)}$$

where the quantity, $\frac{q}{T}$, can be thought of as an "entropy current density". Dividing this by the current density would make the Seebeck coefficient a measure of the entropy per charge within a material, provided the scattering times in j and q are assumed to be equal[10].

It is important to note that unlike the electrical conductivity, the thermopower can be negative or positive, and it is the absolute value that affects the power factor. The sign of the Seebeck coefficient will generally indicate the dominant carrier type. Hall measurements can also be used to determine the major charge carrier[60]. The Seebeck effect, like the electrical conductivity, entails a transport of carriers. In these two processes, the carriers near the Fermi energy are the relevant species. A formal derivation for the thermopower is given by Mott and Davis and Goldsmid[5, 61]. Three cases for the thermopower will be discussed here, one pertaining to metals and degenerate semiconductors (Mott equation), non-degenerate semiconductors, and the other pertaining to hopping conductors (Heike equation.)

2.6.2 High Mobility Conductors and General Remarks

Large effective masses of the charge carriers and large bandgaps generally produce large Seebeck coefficients. As shown in Eq 2.15a and Eq 2.16, the Fermi energy, E_F appears in the calculation of the carrier concentration. Rearrangement shows that that the Fermi energy can be expressed as[53]:

$$\mathrm{E_F} = \frac{\mathrm{h}^2}{2m_e}\left(\frac{3n}{8\pi}\right)^{\frac{2}{3}} \quad \textbf{(Eq 2.27)}$$

Eq 2.27 shows that the Fermi energy decreases with increasing effective mass and increases with increasing carrier concentration, n. The derivation given by Goldsmid for the Seebeck coefficient is:

$$\alpha = \frac{k_b}{e}\left(\frac{\pi^2}{3}\right)\left(k_b T \frac{r+\frac{3}{2}}{E_F}\right) \quad \textbf{(Eq 2.28)}$$

where r is a scattering parameter[5]. From Eq 2.27 and 2.28, it can be seen that as m_e increases, α is expected to increase; with increasing n, α is expected to decrease. A more intuitive form is given by Snyder and Toberer[1]:

$$\alpha = \frac{8\pi^2 k_b^2}{3eh^2} m_e T \left(\frac{\pi}{3n}\right)^{\frac{2}{3}} \quad \textbf{(Eq 2.29)}$$

Eq 2.13 shows that as the effective mass increases, the mobility decreases, which may result in a decrease in the electrical conductivity. This is another example of the trade-off of electrical conductivity and the Seebeck coefficient. Eq 2.29 shows that the absolute value of the thermopower increases with increasing temperature, which is consistent with experimental evidence in most metals[62].

For non-degenerate semiconductors in which bandgaps must be considered, Cox provides an expression that bears some similarity to Eq 2.28[54].

$$\alpha_n = -\frac{k_b}{e}\left[\left(\frac{E_C - E_F}{k_b T}\right) + A\right] \quad \textbf{(Eq 2.30)}$$

$$\alpha_p = \frac{k_b}{e}\left[\left(\frac{E_F - E_V}{k_b T}\right) + A\right] \quad \textbf{(Eq 2.31)}$$

where the subscripts n and p refer to n or p-type, respectively, A is a parameter that describes any changes in mobility with energy changes in a band, but is usually small enough (near unity) to be neglected[54, 63]. However, the term should not always be ignored if the semiconductor possesses large amounts of disorder. In the chalcogenide thin films studied by Rockstad et al., it was found that values of A could be as high as 7 for non-annealed Ge-Te-Si-Se alloys[63]. They showed that the Seebeck coefficient could decrease by up to 250 $\frac{\mu V}{K}$ after annealing / crystallization, showing that the thermopower is larger for more disordered materials[63]. The degree of disorder was tracked to changes of A. That is, A can also be interpreted as a reflection of disorder, with larger values correlated to more disorder[63].

Returning to the other terms in Eq 2.30 and 2.31, E_C and E_V are the energies at the conduction and valence band edges, respectively. Plotting α vs E_F while E_C and T are held constant will show that as E_F increases, α decreases, as in the case of metals. E_F moves closer to the valence band (gets smaller) as p increases. This has the same effect of making α_p smaller, which is consistent with the notion that increasing the carrier concentration will decrease the Seebeck coefficient.

One can also show the thermopower dependence on the band gap from Eq 2.30 and 36. As E_C and E_V are increased or decreased, respectively, the bandgap increases, and from Eq 2.30 and 36, this would also increase the Seebeck coefficient. A larger band gap minimizes intrinsic conduction. The excitation of oppositely charged carriers decreases the absolute value of the Seebeck coefficient.

2.6.3 Hopping Conduction and the Heike Formula

For materials that have hopping conduction, the temperature dependence of the Seebeck coefficient is not very strong[10]. For these materials the thermopower is commonly modeled with the temperature independent Heike equation. A derivation is given by Chaikin and Beni[64]. The most general form, however, is given by Cox:

$$\alpha = \frac{k_b}{e}\left[\ln\left(\frac{c}{1-c}\right) + A\right] \qquad \textbf{(Eq 2.32)}$$

where c and $(1-c)$ are the fractional concentrations of the transition metal ions $[M^{n+}]$ and $[M^{(n+1)}]$[54]. The A term, is both material dependent and difficult to evaluate, but is commonly neglected for most hopping conductors as reported in the literature[64]. Rockstad et al., say that in special circumstances, the value of A may become negative; hopping conduction being one of these cases. This may balance out larger positive values of A due to highly disordered systems, however, the concept has not been well-investigated or proven[63].

The numerator and denominator in Eq 2.32 are specified in such a way so as to give the proper sign for the thermopower corresponding to n or p-type, since an n-type is expected to have a greater number of the lower valence cations. These "c" terms are the analogue of the carrier concentration. Chaikin and Beni remark that the original Heike equation is strictly for systems under high magnetic fields or for when spin is neglected[64]. Over the years, other groups have modified the Heike equation to better suit particular models. Two of these will be briefly reviewed here.

The first modified-Heike model that will be discussed takes into account spin. This serves the purpose of being able to apply the model to more realistic materials as well as lifting the limitation of the high magnetic field. In most transition metal oxides, this Eq 2.32 is not ideal since the configuration and distribution of spin up or down is not accurate; for d^0 ions, the placement of an electron as spin up or down adds degeneracy and hence entropy which should be factored into the thermopower. In order to account for this limitation, Chaikin and Beni modified the Heike equation [64]:

$$\alpha = \frac{k_b}{e}\left[\ln\left(\frac{c}{2-c}\right)\right] \qquad \textbf{(Eq 2.33)}$$

For transition metals that are not d^0 ions, in which degeneracy is relatively large, Koshibae proposed a general modification for degeneracy of the multivalent ion[38]:

$$\alpha = \frac{k_b}{e}\left[\log\left(\frac{g_A}{g_B}\right)\left(\frac{x}{1-x}\right)\right] \qquad \textbf{(Eq 2.34)}$$

where g_A and g_B are the degeneracies of the A and B ions, respectively. x is the relative concentration of A, and $(1-x)$, the B ions. This equation is useful for materials such as

the layered-cobaltites as discussed earlier. In the case of Na_xCoO_2, A and B would correspond to $[Co^{4+}]$ and $[Co^{3+}]$ and g_A and $g_B$would be 6 and 1, respectively[10].

High Seebeck coefficients are crucial to achieving high figures of merit and power factors. However, the contribution of the electrical conductivity should not be underestimated. For hopping conductors, there is a log dependence on the carrier concentration, whereas the electrical conductivity scales directly with carrier concentration. Therefore, there can be significant variation in the magnitudes of electrical conductivity for different materials. As shown in this section, one way to achieve high Seebeck coefficients and preserve electrical conductivity is to introduce disorder to the system. The complications in heavily disordered systems, in which mobility edges become relevant, may alter the band structure relative to what would be expected of a typical-doped semiconductor. As in the case of the electrical conductivity, such a result would also affect the thermopower. This is briefly discussed below for SBN.

2.7 Strontium Barium Niobate (SBN) and the Tungsten Bronze Structure

2.7.1 The Tungsten Bronze Structure

The tungsten bronze structure was first reported by Wöhler in 1824, for Na_xWO_3[65]. This material had a metallic luster and could be made metallic or semiconducting depending on the amount of Na in the chemistry[65]. Magneli was the first to resolve the structure of this bronze through X-ray diffraction[66]. Since then, many compounds have been found to crystallize in the tungsten bronze structure with most of the chemistries being alkali, alkali-earth, rare-earth, or lead tungstates, titanates, niobates, and tantalates[65, 67–70]. In general, tungsten bronzes encapsulate a group of ternary oxide compounds that crystallize in large, complex unit cells with the key motif of distorted, corner-sharing oxygen-octahedra[65]. The structure shares some similarity with the perovskites in that the periodicity of the structure can be traced by the translational symmetry of the corner-sharing octahedra with other atoms filling in the channels between them. The tungsten bronzes exhibit a wide range of properties that allow for diverse applications. For example,

tungsten bronze systems have shown semiconductivity, metallic conductivity, superconductivity, high permittivity, high piezoelectric or pyroelectric coefficients, and/or ferroelectricity[65, 68, 71–73].

Tungsten-bronze structures exist in several crystal systems, namely cubic, tetragonal (type I and type II), hexagonal, and orthorhombic[72]. The difference between the tetragonal-I and tetragonal-II types is in the rotation of the corner-sharing octahedra within the unit cell. Na_xWO_3 will go from type I to type II with decreasing Na content[72]. Figure 2-8 depicts the difference between type I and type II. For the Na_xWO_3 tungsten-bronze, type I is metallic and type II is semiconducting at ambient temperatures[72]. Moreover, the type I also exhibits superconductivity at around 0.57 K. As the Na content is increased, the transition temperature, T_c, increases exponentially up until the type II transition[72].

In this work, only the type I tetragonal tungsten bronze will be reviewed because it is the pertinent crystal structure of SBN. As a ferroelectric, the point group is 4mm; the prototype centrosymmetric point group is 4/mmm[74].

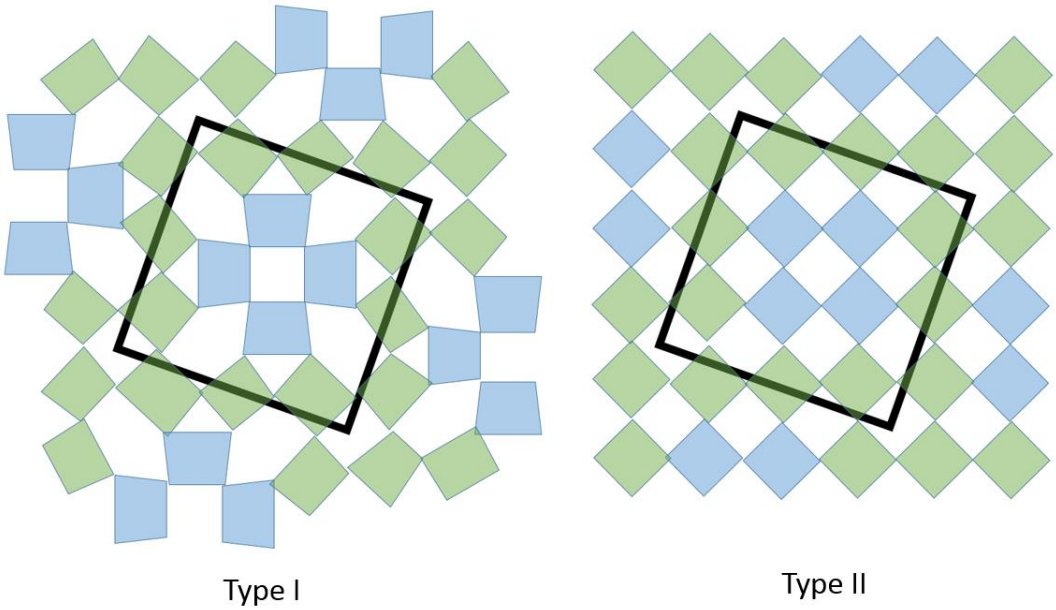

Figure 2-8. Planar projection (a-b plane) view of the difference between type I and type II tetragonal tungsten bronzes. The blue octahedra are the portions which can be rotated to go from type I to type II. The distortion of the octahedra of the type II projection have been eliminated to emphasize the order relative to type I. Redrawn from Ngai et al[72].

The unit cell of the tetragonal tungsten bronze is large compared to the perovskites, with $a = b \approx 12.5$ Å and $c \sim 3.4$ Å. To represent the unit cell size and the occupancy of each atom, the general chemical formula is usually written as:

$$[A1_2A2_4C_4][B1_2B2_8]O_{30}$$

where A1, A2, C, B1, B2, and O refer to the unique positions in which the types of cations can occupy within the unit cell[52, 75]. Figure 2-9 shows the crystal structure of the SBN tungsten bronze with these positions labeled. From Figure 2-9, some features of the structure can be used to explain the general properties that may be encountered in the tetragonal tungsten bronzes.

2.7.2 The A-sites in the Tetragonal Tungsten Bronze Structure

The numerous positions in the tungsten bronze structure offers exceptional flexibility in tailoring properties. While any of the atomic positions in the tungsten bronze structure can be manipulated (e.g. vacancies or composition), the A-site is arguably the most versatile. Jamieson has attributed the diversity in characteristics of these compounds primarily by the size and charge of the cations and the occupancy of the A-site[68]. Two ways in which the A-site occupancy affects the properties of SBN will be discussed. The first is the preferential site occupancy of Sr and Ba atoms as the composition changes. The second is how many of the A-sites are occupied. The latter is a central focus of this work and it will be discussed in detail in the results chapter. The general chemical formula for the tungsten bronze as shown above refers to a "stuffed-bronze" in which all sites are occupied. Only small cations such as Li^+ can occupy the C sites (e.g. $K_6Li_4Nb_{10}O_{30}$)[70, 75]. The other special designations are the "filled" and "unfilled" bronzes, which have all 6 A-sites occupied and 5 out of 6 A-sites occupied, respectively. SBN is typically studied in the unfilled composition; good piezoelectric and pyroelectric coefficients, permittivities, and electro-optic properties have been reported[76]. In the unfilled case, the chemical formula may be simplified to $Sr_{1-x}Ba_xNb_2O_6$.

In the tungsten bronzes, most non-transition metal cations, including Sr and Ba, occupy the A-sites. Figure 2-9b illustrates the difference between the A1 and the A2 sites. The A1 site is a square channel while the A2 site is a larger, distorted pentagonal channel.

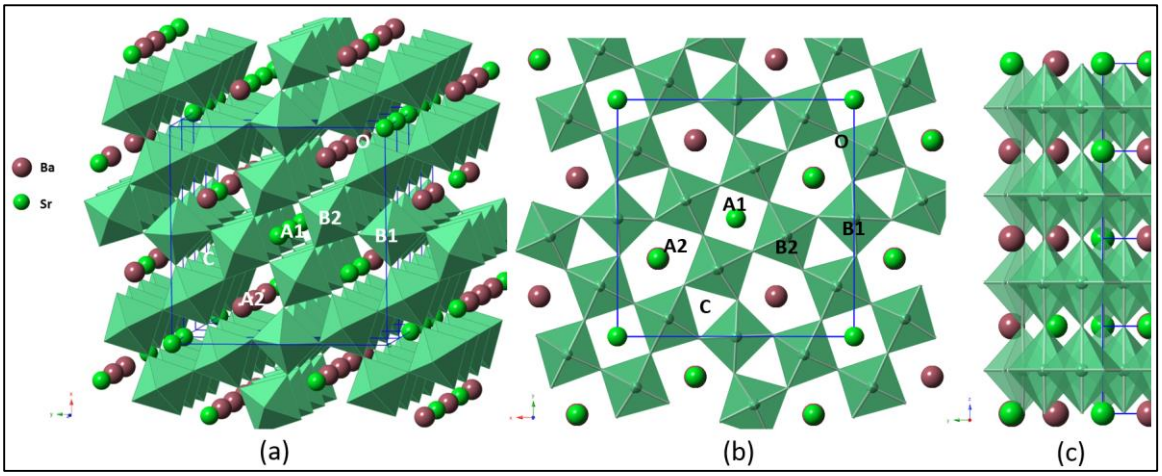

Figure 2-9. (a) Tilted view showing multiple unit cells of the SBN tungsten bronze. Octahedra are shown. (b) a-b plane planar projection (// c-axis). Octahedra are translucent to show how the Nb-O-Nb bond angles differentiate two types of Nb atoms: B1 and B2. (c) b-c planar projection (//a-axis) showing the unique c-axis (the length of the unit cell in the a-b plane is not shown). Figures are drawn from Crystal Maker® using X-ray data reported by Sunshine et al.[77].

Originally, Jamieson reported the A2 site to be the smaller of the two, depicted as a tri-capped prism with a coordination of 9, and the A1 to be a larger rectangular prism with a coordination of 12[68]. However, Leffler found that this was inconsistent with the observed preferential A2 occupancy for the larger Ba atom; this was demonstrated by the fact that less than 5% of the A1 sites are occupied by Ba.[78]. The results in the Rietveld refinement showed that the average bond lengths of Sr-O and Ba-O at the A2 site was indeed longer than the A1 site (2.84 and 2.76 Å, respectively)[78]. The longer average bond lengths on the A2 site implied a larger tunnel. More recent works have accepted that A2 is the larger site, with A1 and A2 sites to be 12 and 15 coordinated, respectively[73, 79].

The size differences in the A1 and A2 site impose preferential site occupancies for atoms of different sizes. It was stated earlier that Ba, being the larger atom was seldom found at the smaller A1 site. The preferential site occupancy for Sr, however, was shown

to depend on the composition; as the Sr content is decreased, there is a preference for occupying the A2 site, leaving the A1 sites vacant[78, 80]. SBN transitions from a relaxor ferroelectric to a normal ferroelectric with decreasing Sr content[71, 80]. For high Sr contents in SBN ,a strong frequency dispersion of the dielectric constant is shown near the temperature of maximum relative permittivity, T_{max}[74]. This is shown in Figure 2-10. An introduction to relaxor ferroelectrics is provided by Cross (reference 74.) For the relaxor composition of $Sr_{0.75}Ba_{0.25}Nb_2O_6$, Ballman et al. had shown that the Curie temperature, which in this context refers to the onset of bulk spontaneous polarization, is approximately 340 K[81]. The Burns temperature (which only applies to relaxors), in contrast to the Curie temperature, is an indication of the onset of nucleation of nano-polar regions on much smaller length scales. For the unreduced $Sr_{0.60}B_{0.40}Nb_2O_6$ composition, this was reported by Bhalla et a. to be about 625 K[82].

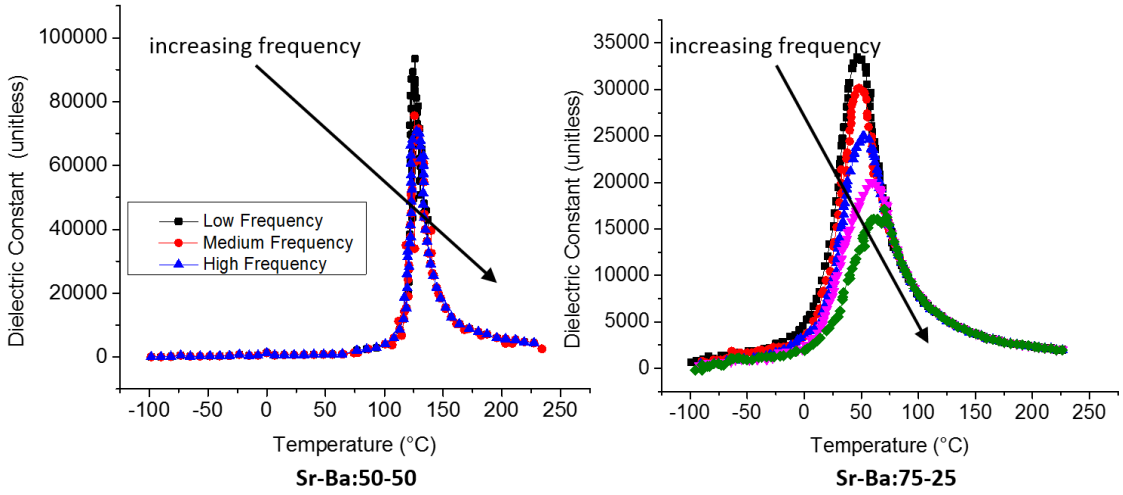

Figure 2-10. Onset of relaxor characteristics with increasing Sr content for the unfilled SBN. Relaxor ferroelectrics show a strong frequency dispersion and a broadening of the dielectric peak that is a reflection of compositional disorder or chemical inhomogeneity. Replotted from Huang et al.[71].

The way in which the A-site is occupied may also have steric consequences. For example, the unfilled SBN tetragonal tungsten bronze does not form a complete solid solution across the entire composition. The pseudo-binary phase diagram developed by Carruthers and Grasso shows that for $Sr_{1-x}Ba_xNb_2O_6$ (the unfilled SBN), the approximate solubility for x is $0.20 \leq x \leq 0.80$[83]. Extending beyond these limits shows that the

strontium and barium end members are orthorhombic, as shown in Figure 2-11. Trubelja et al. attributes the orthorhombic phase to a consequence of the A-site cations' steric effects on the NbO_6 octahedra[80].

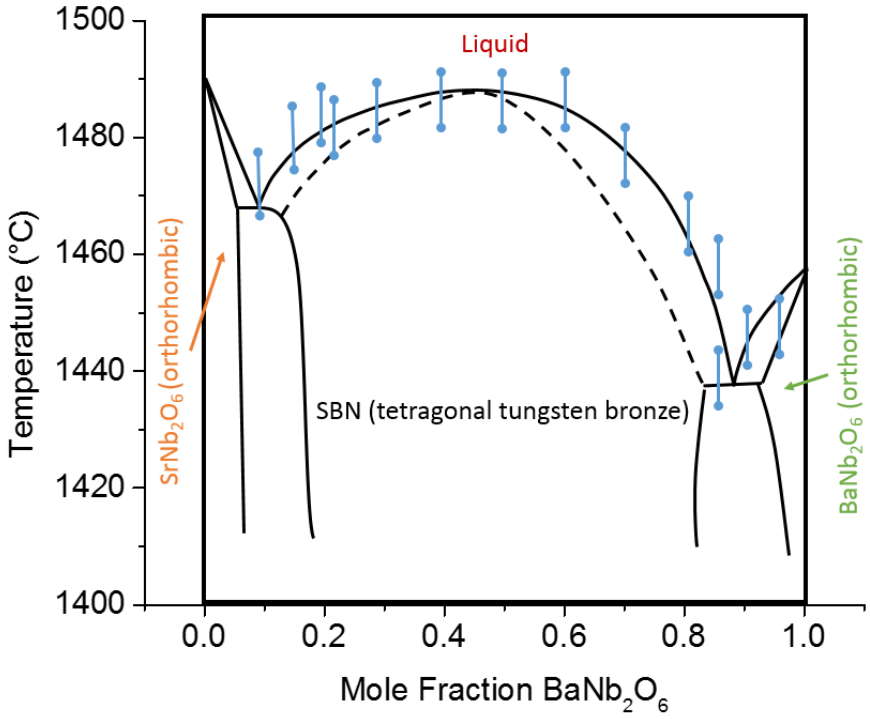

Figure 2-11. The unfilled SBN pseudo-binary phase diagram. Solid solution extends to about $0.20 \leq x \leq 0.80$. The end members are orthorhombic phases. The blue lines with circular end-caps represent error bars. Replotted from Carruthers and Grasso[83].

A-site occupancy is also expected to affect the c-axis of the structure. Figure 2-8c shows that another structural feature of the tetragonal tungsten bronzes is the unique c-axis. In ferroelectric tetragonal SBN, this is the only polar direction[52, 74, 80]. This c-axis view also shows that the Nb-O-Nb bond angle in this direction is nearly 180°. Following the band model proposed by Goodenough for the sodium tungsten bronzes, the near-180° bond angle should provide the most overlap between the d and p orbitals of the transition metal and oxygen, respectively, making this axis the high electrical conductivity direction[84]. However, steric effects associated with the A-site occupancy is thought to result in octahedral tilts; increasing the Ba content would result in more "upright" octahedra[80]. Jamieson has stated that these tilts can vary the near-180° bond angle $\pm 8°$ [68].

It is possible the deviation from the ideal bond angle due to tilting may affect electrical conductivity. In addition, tilting affects other properties. Relaxor ferroelectrics tend to possess a high degree of disorder, and the relaxor behavior in SBN is attributed to the fluctuating distribution of Ba and Sr atoms in both A-sites[74]. This is consistent with the site occupancy of Sr changing with increasing Sr content as discussed above, where less Sr leads to higher A1 vacancy. In SBN, Trubelja et al. has suggested that the minimization of tilting with increasing Ba content results in a more-ordered polarization vector that collectively points closer to [001], which may also explain the normal ferroelectric behavior at higher Ba contents.

In contrast, the Nb-O-Nb bond angles along the a-b plane do not show the consistent ~180° bond angle. Stephenson has calculated the angles associated with the pentagonal channel and the triangular channel of tetragonal $Ba_6Ti_2Nb_8O_{30}$ along the a-b plane to be 87°, 87°, 118°, 119°, and 129° $\pm$4° for the pentagonal A2 site and 58°, 61°, and 61°$\pm$4° for the triangular C site, respectively[85]. The comparison of the c-axis and the a-axis has shown that useful properties can be found in the c-axis direction.

2.7.3 Strontium Barium Niobate as a Thermoelectric

SBN has only recently been studied as a thermoelectric, when Lee et al. investigated the relationship between ferroelectricity and thermoelectricity[86]. SBN single crystals showed promise of high zTs due the glass-like thermal conductivity reported in other relaxor ferroelectrics (e.g. PMN)[14, 87]. It is believed that the high concentration of nano-polar regions in such a material would effectively scatter phonons[14, 87]. Single crystal relaxor ($Sr_{0.65}Ba_{0.35}Nb_2O_6$) SBN was shown by Fischer et al. to possess low thermal conductivities of $\sim 1.0\ \frac{W}{m-K}$T at 100 K [88]. Choy et al. reported single crystal thermal conductivities at higher temperatures in a more Ba-rich composition, which extrapolated well to Fischer's values. This is shown in Figure 2-12. At 500K, a thermal conductivity of $\sim 2.0\ \frac{W}{m-K}$ was reported, showing that there was no significant increase at higher temperatures[89].

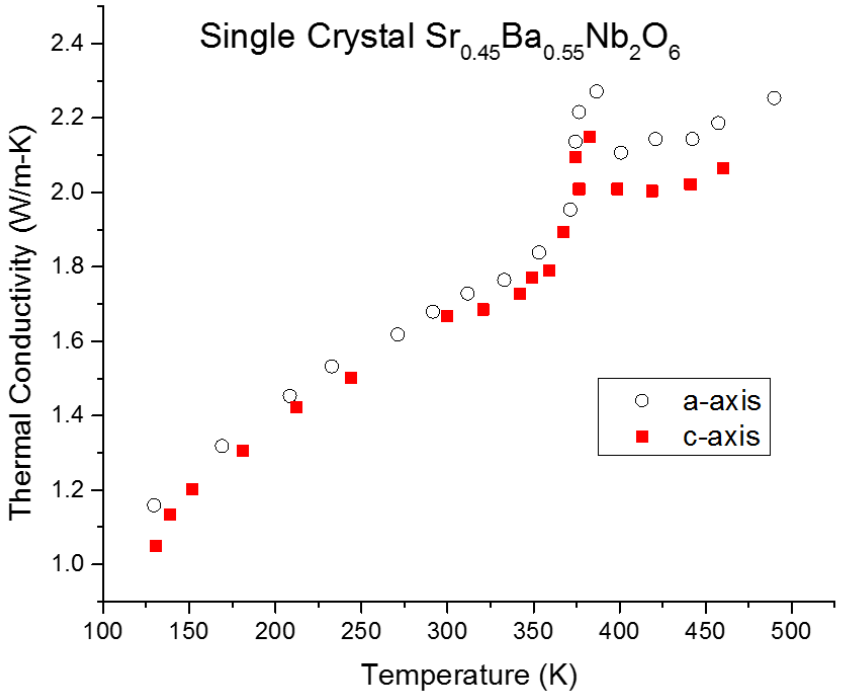

Figure 2-12. Thermal conductivity of $Sr_{0.45}Ba_{0.55}Nb_2O_6$ single crystals up to 500 K. Both the c-axis and a-axis exhibit low thermal conductivities that are in the same magnitude as the bismuth tellurides. Replotted from Choy et al.[89].

Lee et al. showed that SBN also possessed an anisotropic thermopower that was greater along the c-axis[86]. In conjunction with the anisotropy in the electrical conductivity and thermal conductivity, this means that the c-axis is also the high zT axis. SBN was made electrically conductive under reducing atmospheres under the following defect reaction:

$$null \leftrightarrow V_0^{\cdot\cdot} + \frac{1}{2}O_2 + 2e^- \qquad \textbf{(Eq 2.35)}$$

The anisotropy of the thermopower and power factor of oxygen-deficient SBN is shown in Figure 2-13. A higher thermopower parallel to the c-axis relative to the a-axis is observed regardless of the reduction condition. For lower partial pressures of oxygen, there is a decrease in the magnitude of the Seebeck coefficient due to an increased carrier concentration. Figure 2-13b illustrates the high power factor in SBN is the c-axis. Because the thermopowers shown in Figure 2-13a at 10^{-14} atm pO_2 for both the a and c-

axis are of a similar magnitude, it can be inferred from Figure 2-13b that the ratio of electrical conductivity between the a and c-axis is around an order of magnitude. Figure 2-13c shows the power factors of SBN along the c-axis in a variety of different reducing atmospheres. This figure reveals a dramatic increase in the power factor to $\sim 40.8 \frac{\mu W}{cm-K^2}$ from 10^{-12} to 10^{-14} atm pO_2. The increase is due to an increase in the electrical conductivity. This can be inferred from Figure 2-13a, which shows a large decrease in magnitude of the Seebeck coefficient from 10^{-12} to 10^{-14} atm pO_2. The anomalous increase in electrical conductivity is accompanied by the precipitation of an NbO_{2-x} secondary phase.

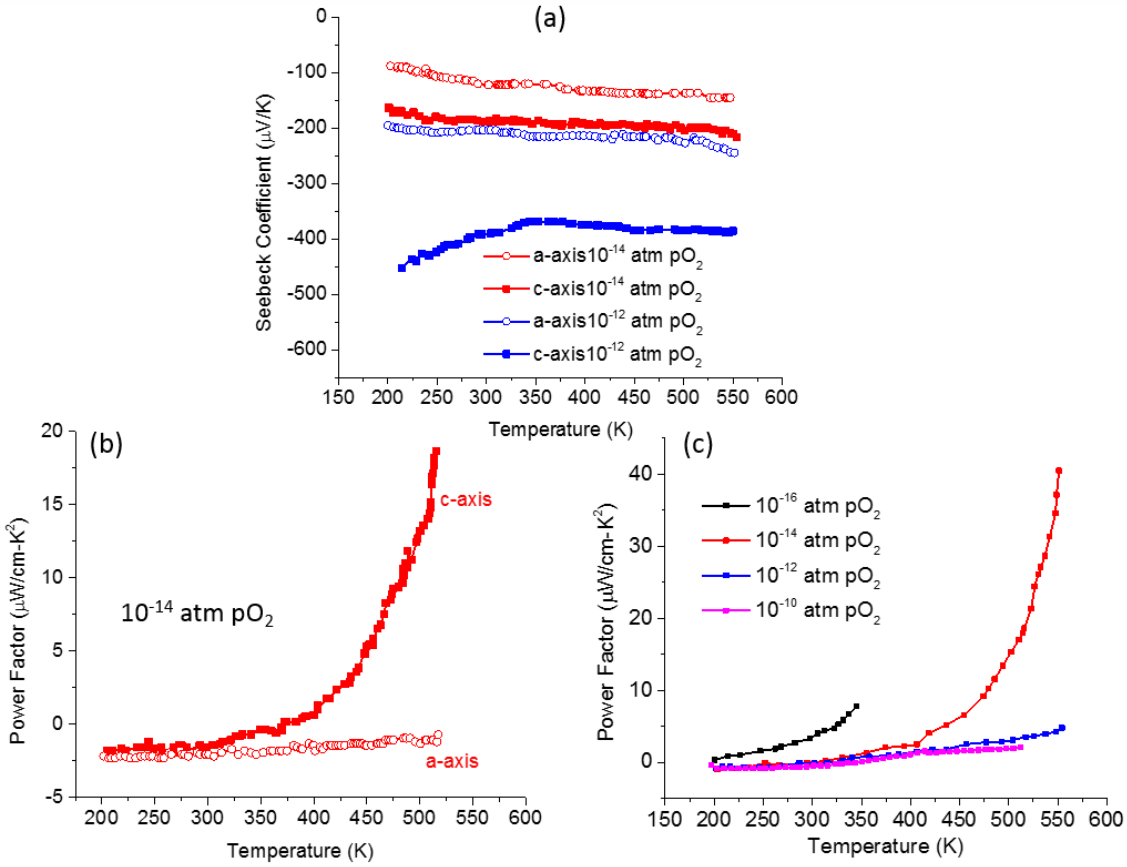

Figure 2-13. (a.) Seebeck coefficients of SBN along the a and c-axis under two reducing conditions. (b.) Power factor of SBN reduced under 10^{-14} atm pO_2. (c.) Power factors of SBN along the c-axis showing anomalous power factor increase from 10^{-12} to 10^{-14} atm pO_2. Replotted from Lee et al.[86].

The figure of merit for SBN has been reported to be $\sim 0.5 - 1.12$ at 550 K for single crystals, owing to the high power factors and low thermal conductivities that were reported by Lee et al. and Choy et al, respectively[14]. The upper bound of zT rivals that of $NaCoO_2$. For this reason, SBN showed promise as a thermoelectric oxide. As an n-type oxide, SBN would also complement the p-type $NaCoO_2$ in devices.

Lee et al. also investigated the conduction mechanisms by modeling the temperature dependence of the thermopower. It was reported originally that for the samples reduced using 10^{-16} atm pO_2, there was little change in the thermopower with temperature, suggesting a hopping mechanism even up to 550 K. For samples reduced at 10^{-14} atm pO_2 (Figure 2-13a), the thermopower had a weak dependence on temperature at below 325 K. The thermopower becomes invariant, similar to the case reported in the sample reduced at 10^{-16} atm. This suggested that there was a change in the conduction mechanism to hopping[86]. Electron energy loss spectroscopy has shown that both the Nb^{4+} and Nb^{5+} states exist in these heavily reduced samples[86]. This is consistent with the conditions required for hopping conduction.

For the samples reduced at 10^{-12} atm, in which the anomalous conductivity increase does not occur, Figure 2-13a shows that the absolute value of the Seebeck coefficient decreases with increasing temperature below about 325 K. This is the expected relationship for the non-hopping semiconductor. Above this temperature, the thermopower was stated to be approximately invariant. The temperature at which these transitions occur coincides with the ferroelectric transition temperature of 340 K reported by Ballman[81]. The work suggests that polarization effects on the thermopower may be occluded by higher carrier concentrations. This thought is consistent with the idea that high carrier concentrations can suppress ferroelectricity[14].

Reduced SBN ceramics with varying compositions were investigated by Bock et al. In that work, the electrical conductivity was shown to exhibit the anomalous increase as the reducing atmosphere was changed from 10^{-12} to 10^{-14} atm pO_2 [59]. It was shown that the Seebeck coefficient had a measurable dependence on temperature, and should not be considered invariant as reported by Lee et al.. The thermopower is shown in Figure 2-14

for several compositions of SBN. The temperature dependence is made more obvious in Figure 2-14 due to the scaling of the plot.

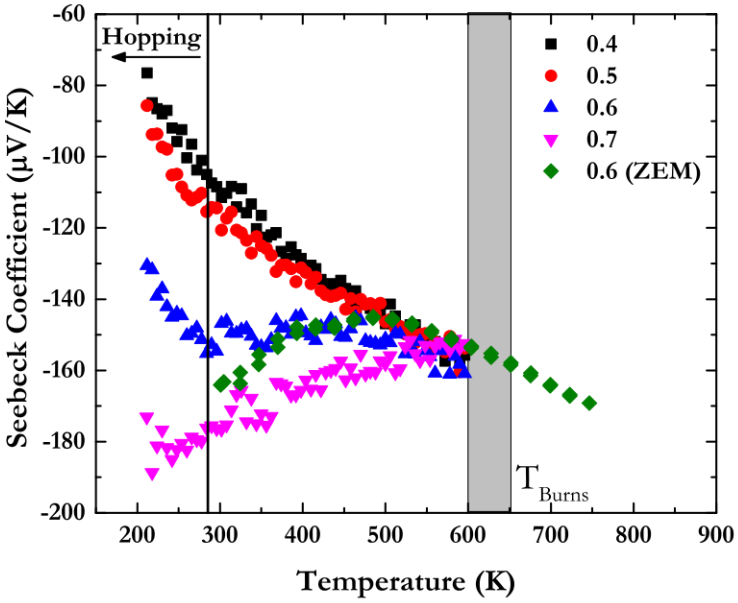

Figure 2-14. Thermopower dependence of unfilled atm $Sr_xBa_{1-x}Nb_2O_6$ for various values of x annealed at 10^{-14} atm. The green data points that extend to higher temperatures were taken at NASA Glenn Research Center. Source: Bock et al.[59].

Figure 2-14 provides two important insights: the first being that SBN may not be a hopping conductor above room temperature. Secondly, there is a difference in how relaxor polarization affects thermoelectricity relative to normal ferroelectrics[59]. The fact that there is an obvious temperature dependence to the thermopower is not consistent with the Heike model for hopping conductors. The compositions where $x = 0.4$ and $x = 0.5$ can be regarded as normal ferroelectric compositions in SBN. A linear (or possibly ln) dependence in the Seebeck coefficient with temperature was found in these compositions. For higher Sr compositions, a somewhat-parabolic trend was observed, with low temperatures showing a decrease in the absolute value of the thermopower with temperature. In the 60-40 composition ($x = 0.6$), the extended temperature data shows that the thermopower becomes more linear. The trends in Figure 2-14 show the compostions of SBN start to converge on approaching the Burns Temperature, suggesting that once there is no polarization, the materials will behave similarly.

An explanation for the trends observed in Figure 2-14 requires the use of a modified band structure of SBN. The assumption was that SBN was either a band-conducting semicondcutor or a hopping conductor. The thermopower trends are not entirely consistent with either of these models, but in fact is metal-like in that the magnitude depends linearly with temperature (Eq 2.29)[90]. Of course, the Seebeck coefficient would have to extrapolate to 0 at 0 K if this was true, and that is not the case with SBN.

Bock et al. mapped the conduction mechanisms at different temperature ranges. The nearest neighbor hopping mechansim was checked by plotting $\ln(\sigma T)$ vs. $\frac{1}{k_b T}$ (Eq 2.22). It was found that for the relaxor compositions, $x = 0.6$ and $x = 0.7$, the electrical conductivity data were consistent with hopping conduction from 300 to 400 K. Outside of this temperature range and composition, this hopping model was not satisfactory due to the deviation in linearity[59]. For temperatures below 300 K, all compositions annealed at 10^{-14} atm pO_2 were found to fit the "non-activated" hopping proposed by Emin. Thus at low temperatures, there is strong evidence that the reduced unfilled SBNs annealed at 10^{-14} atm pO_2 are hopping conductors only at low temperatures. A different scheme (i.e. a disordered band conductor) must be considered for higher temperatures.

Similar behavior in the conductivity was reported in the La-doped $BaTiO_3$ thin films of Gilbert et al., where hopping behavior was coupled with an increasing absolute value of Seebeck coefficients with temperature[90]. In that work, the measured activation energies suggested that the carrier mobilities were activated, which is inconsistent with metals. The fact that the thermopower did not scale with $\frac{1}{T}$ (Eq 2.30 and 2.31) disagreed with the picture of a high-mobility semiconductor. The model that was suggested was an Anderson-localization-modified band structure. Anderson localization is a phenomenon that occurs in materials with a large degree of disorder[54]. This gives rise to mobility edges that localize carriers unless they are able to be excited over these mobility edges[54]. Hence, this type of band conduction has a thermally activated-mobility.

As a consequence of the crystal field splitting (due to octahedral coordination of the transition metal) in conjunction with the electron correlation energy, U, the impurity band (either from doping or oxygen vacancies) now consists of an upper and lower

Hubbard band[90]. The upper and lower Hubbard bands correspond to the states in the t_{2g} band[54, 90, 91]. For SBN, $BaTiO_3$, and $SrTiO_3$. the Fermi level is located just under the conduction band and within the lower Hubbard band. The pseudo-gap is a consequence of the mobility edges.

In the work of Gilbert et al., the lower Hubbard band was located near the empty Ti 3d conduction band of $BaTiO_3$ and with sufficient doping, would partially overlap with a mobility-edge separation[90]. This band structure was consistent with the photoemission spectra reported by Robey et al.[91].

The schematic band structure shown by Bock et al. for these reduced SBNs, originally proposed by Gilbert et al. for La-doped $BaTiO_3$, is illustrated in Figure 2-15 along with the proposed mobility edges. At low temperatures, the thermal energy, k_bT, is insufficient to excite carriers out of the mobility edges. This is consistent with a localized hopping behavior at low temperatures. However, at sufficiently high temperatures (greater than 450 K), carriers can reach the Nb 4d conduction band via the overlapping Hubbard band. Despite being a band conductor at elevated temperatures, the mobility edges result in a thermally activated mobility, and hence thermally activated conductivity.

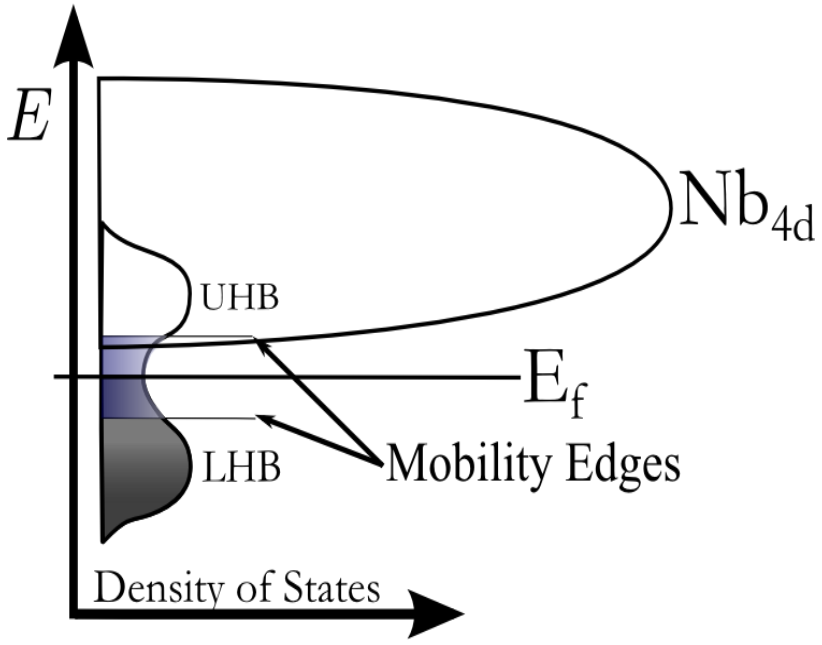

Figure 2-15. The proposed band structure for reduced SBN. Source: Bock et al.[59].

Provided this model is true, then the thermopower dependence of temperature agrees well with the models devised by Mott as noted by Bock et al.. When mobility edges are present, Mott and Cutler proposed that a material could exhibit a linear thermopower dependence with temperature at low temperatures[92]. If there is excitation above the mobility edge into the conduction band, then a $\ln(T)$ dependence would be observed[61]. Due to the lack of data over an extended temperature range, whether SBN obeyed a linear temperature or $\ln(T)$ dependence could not be concluded[59]. The unified and consistent model of Bock et al. provides a good reference point for thermoelectric trends (e.g. temperature dependences and magnitudes) for the filled SBN system. Two other important reference points can be taken away from their work. One is that a power factor of about $3.4\,\frac{\mu W}{cm-K^2}$ was achieved in 10^{-14} atm-annealed 60-40 Sr-Ba ceramics and the other being that samples reduced at either 10^{-14} or 10^{-16} atm demonstrated maximum conductivities in the temperature range of about 550 K and 800 K[59].

2.8 References

[1] G.J. Snyder and E.S. Toberer, "Complex Thermoelectric Materials," *Nat. Mater.*, **7** [2] 105–14 (2008).

[2] H.J. Goldsmid, *Applications of Thermoelectricity*. Methuen, London, England, 1960.

[3] H.J. Goldsmid, *Thermoelectric Refrigeration*. Plenum Press, New York, NY, 1964.

[4] R.E. Newnham, *Properties of Materials : Anisotropy, Symmetry, Structure: Anisotropy, Symmetry, Structure*. Oxford University Press, Oxford, 2004.

[5] H.J. Goldsmid, *Introduction to Thermoelectricity*. Springer Science & Business Media, Berlin, Germany, 2010.

[6] H.S. Lee, *Thermal Design: Heat Sinks, Thermoelectrics, Heat Pipes, Compact Heat Exchangers, and Solar Cells*. John Wiley & Sons, Hoboken, NJ, 2010.

[7] F.J. Donahoe, *Theoretical Bound on the Thermoelectric Figure of Merit*, *Electr. Eng.*, **79** [6] 488–490 (1960).

[8] H. Littman and B. Davidson, "Theoretical Bound on the Thermoelectric Figure of Merit from Irreversible Thermodynamics," *J. Appl. Phys.*, **32** [2] 217–219 (1961).

[9] M.C. Nicolaou, "Thermoelectric Figure of Merit of Degenerate and and Nondegenerate Semiconductors;" PhD Thesis, Northeastern University, 2008.

[10] I. Terasaki, "Layered Cobalt Oxides: Correlated Electrons for Thermoelectrics;" pp. 51–70 in *Thermoelectr. Nanomater. SE - 3*. Edited by K. Koumoto and T. Mori. Springer Berlin Heidelberg, 2013.

[11] N.R. Kristiansen and H.K. Nielsen, "Potential for Usage of Thermoelectric Generators on Ships," *J. Electron. Mater.*, **39** [9] 1746–1749 (2010).

[12] D. Rowe, *CRC Handbook of Thermoelectrics*. CRC Press, Boca Raton, FL, 2010.

[13] T. Okuda, K. Nakanishi, S. Miyasaka, and Y. Tokura, "Large Thermoelectric Response of Metallic Perovskites: $Sr_{1-x}La_xTiO_3$ ($0 \leq x \leq 0.1$)," *Phys. Rev. B,* **63** [11] 113104–1 – 113104–4 (2001).

[14] S. Lee, J.A. Bock, S. Trolier-McKinstry, and C.A. Randall, "Ferroelectric-thermoelectricity and Mott Transition of Ferroelectric Oxides with High Electronic Conductivity," *J. Eur. Ceram. Soc.*, **32** [16] 3971–3988 (2012).

[15] C. Wood, "Materials for Thermoelectric Energy Conversion," *Reports Prog. Phys.*, **51** 459–539 (1988).

[16] F.J. Strieter, "Growth of Single Crystal Bismuth Telluride," *Adv. Energy Convers.*, **1** 125–127 (1961).

[17] D. Teweldebrhan, V. Goyal, and A.A. Balandin, "Exfoliation and Characterization of Bismuth Telluride Atomic Quintuples and Quasi-two-dimensional Crystals," *Nano Lett.*, **10** [4] 1209–1218 (2010).

[18] M. Ashida, T. Hamachiyo, K. Hasezaki, H. Matsunoshita, M. Kai, and Z. Horita, "Texture of Bismuth Telluride-Based Thermoelectric Semiconductors Processed by High-pressure Torsion," *J. Phys. Chem. Solids*, **70** [7] 1089–1092 (2009).

[19] Y. Pei, Z.M. Gibbs, A. Gloskovskii, B. Balke, W.G. Zeier, and G.J. Snyder, "Optimum Carrier Concentration in n-Type PbTe Thermoelectrics," *Adv. Energy Mater.*, **4** [13] 1–12 (2014).

[20] G.S. Nolas and G.A. Slack, "Thermoelectric Clathrates," *Am. Sci.*, **89** [2] 136–141 (2001).

[21] T. Takabatake, K. Suekuni, T. Nakayama, and E. Kaneshita, "Phonon-glass Electron-crystal Thermoelectric Clathrates: Experiments and Theory," *Rev. Mod. Phys.*, **86** [2] 1–51 (2014).

[22] C.B. Vining, W. Laskow, J.O. Hanson, R.R. der Beck, and P.D. Gorsuch, "Thermoelectric Properties of Pressure-sintered $Si_{0.8}Ge_{0.2}$ Thermoelectric Alloys," *J. Appl. Phys.*, **69** [8] 4333–4340 (1991).

[23] G.M. Fradkin and V.M. Kodyukov, "Radioisotope Thermoelectric Generators," *Sov. At. Energy*, **26** [2] 193–198 (1969).

[24] D.A. Wright, "Materials for Direct-conversion Thermoelectric Generators," *Metall. Rev.*, **15** [1] 147–160 (1970).

[25] R.R. Heikes, R.W. Ure, and S.J. Angello, *Thermoelectricity, Science and Engineering*. Interscience Publishers, New York, NY, 1961.

[26] J.Q. Guo, H.Y. Geng, T. Ochi, S. Suzuki, M. Kikuchi, Y. Yamaguchi, and S. Ito, "Development of Skutterudite Thermoelectric Materials and Modules," *J. Electron. Mater.*, **41** [6] 1036–1042 (2012).

[27] E.A. Skrabek and D.S. Trimmer, "Properties of the General TAGS System;" pp. 267–275 in *CRC Handb. Thermoelectr.* CRC Press: Boca Raton, FL, 1995.

[28] L.-D. Zhao, S.-H. Lo, Y. Zhang, H. Sun, G. Tan, C. Uher, C. Wolverton, V.P. Dravid, *et al.*, "Ultralow Thermal Conductivity and High Thermoelectric Figure of Merit in SnSe Crystals.," *Nature*, **508** [7496] 373–7 (2014).

[29] I. Terasaki, "Physics of the Thermoelectric Oxide $NaCo_2O_4$: A Guide to New Thermoelectric Oxides," *Twenty-First Int. Conf. Thermoelectr. 2002. Proc. ICT '02.*, (2002).

[30] D.M. Smyth, *The Defect Chemistry of Metal Oxides*. Oxford University Press, New York, NY, 2000.

[31] I. Terasaki, Y. Sasago, and K. Uchinokura, "Large Thermoelectric Power in $NaCo_2O_4$ Single Crystals," *Phys. Rev. B*, **56** [20] R12685–R12687 (1997).

[32] Y. Takahashi, Y. Gotoh, and J. Akimoto, "Single-crystal Growth, Crystal and Electronic Structure of $NaCoO_2$," *J. Solid State Chem.*, **172** [1] 22–26 (2003).

[33] S. Horii, I. Matsubara, M. Sano, K. Fujie, M. Suzuki, R. Funahashi, M. Shikano, W. Shin, *et al.*, "Thermoelectric Performance of Magnetically c -Axis Aligned Ca-based Cobaltites," *Jpn. J. Appl. Phys.*, **42** [Part 1, No. 11] 7018–7022 (2003).

[34] K. Fujita, T. Mochida, and K. Nakamura, "High-temperature Thermoelectric Properties of $Na_xCoO_{2-\delta}$ Single Crystals," *Jpn. J. Appl. Phys.*, **40** [7R] 168–171 (2001).

[35] M. Ito, T. Nagira, D. Furumoto, S. Katsuyama, and H. Nagai, "Synthesis of $Na_xCo_2O_4$ Thermoelectric Oxides by the Polymerized Complex Method," *Scr. Mater.*, **48** [4] 403–408 (2003).

[36] N. Mott, *Conduction in Non-crystalline Materials*. Oxford University Press (UK), 1993.

[37] D.J. Singh, "Electronic Structure of $NaCo_2O_4$," *Phys. Rev. B*, **61** [20] 13 397–13 402 (2000).

[38] W. Koshibae, K. Tsutsui, and S. Maekawa, "Thermopower in Cobalt Oxides," *Phys. Rev. B*, **62** [11] 6869–6872 (2000).

[39] G. Xu, R. Funahashi, M. Shikano, I. Matsubara, and Y. Zhou, "Thermoelectric Properties of the Bi-and Na-substituted $Ca_3Co_4O_9$ System," *Appl. Phys. Lett.*, **80** [20] 3760–3762 (2002).

[40] S. Walia, S. Balendhran, H. Nili, S. Zhuiykov, G. Rosengarten, Q.H. Wang, M. Bhaskaran, S. Sriram, *et al.*, "Transition Metal Oxides – Thermoelectric Properties," *Prog. Mater. Sci.*, **58** [8] 1443–1489 (2013).

[41] M. Ohtaki and R. Hayashi, "Enhanced Thermoelectric Performance of Nanostructured ZnO: a Possibility of Selective Phonon Scattering and Carrier Energy Filtering by Nanovoid Structure;" pp. 276–279 in *Thermoelectr. 2006. ICT'06. 25th Int. Conf.* IEEE, 2006.

[42] H. Kaga, Y. Kinemuchi, S. Tanaka, A. Makiya, Z. Kato, K. Uematsu, and K. Watari, "Fabrication of a- and c-axis Oriented ZnAlO by a High Magnetic Field via Gelcasting," 2–5 (2006).

[43] H. Kaga, Y. Kinemuchi, S. Tanaka, A. Makiya, and Z. Kato, "Fabrication of c-axis Oriented ZnAlO by a High Magnetic Field via Gelcasting and its Thermoelectric Properties," (2006).

[44] H. Kaga, Y. Kinemuchi, S. Tanaka, A. Makiya, Z. Kato, K. Uematsu, and K. Watari, "Preparation and Thermoelectric Property of Highly Oriented Al-doped ZnO Ceramics by a High Magnetic Field," *Japanese J. Appl. Physics, Part 2 Lett.*, **45** 88–91 (2006).

[45] Z.L. Wang, "Zinc Oxide Nanostructures: Growth, Properties and Applications," *J. Phys. Condens. Matter*, **16** [25] R829–R858 (2004).

[46] S. Lee, G. Yang, R.H.T. Wilke, S. Trolier-McKinstry, and C.A. Randall, "Thermopower in Highly Reduced n-type Ferroelectric and Related Perovskite Oxides and the Role of Heterogeneous Nonstoichiometry," *Phys. Rev. B*, **79** [13] 134110–1 – 134110–8 (2009).

[47] S. Ohta, T. Nomura, H. Ohta, and K. Koumoto, "High-temperature Carrier Transport and Thermoelectric Properties of Heavily La-or Nb-doped $SrTiO_3$ Single Crystals," *J. Appl. Phys.*, **97** [3] 34106–1 – 34106–4 (2005).

[48] J. Ravichandran, W. Siemons, D.-W. Oh, J.T. Kardel, A. Chari, H. Heijmerikx, M.L. Scullin, A. Majumdar, *et al.*, "High-temperature Thermoelectric Response of Double-doped $SrTiO_3$ Epitaxial Films," *Phys. Rev. B*, **82** [16] 165126–1 – 165126–5 (2010).

[49] S. Funahashi, T. Nakamura, K. Kageyama, and H. Ieki, "Monolithic Oxide–metal Composite Thermoelectric Generators for Energy Harvesting," *J. Appl. Phys.*, **109** [12] 124509–1 – 124509–4 (2011).

[50] S.O. Kasap, *Principles of Electronic Materials and Devices*, 3rd ed. McGraw Hill, New York, NY, 2006.

[51] A.R. West, *Basic Solid State Chemistry*, Second. John Wiley & Sons Inc, Hoboken, NJ, 1999.

[52] A.J. Moulson and J.M. Herbert, *Electroceramics: Materials, Properties, Applications*. John Wiley & Sons, West Sussex, England, 2003.

[53] R.E. Hummel, *Electronic Properties of Materials*. Springer Science & Business Media, New York, NY, 2000.

[54] P.A. Cox, *Transition Metal Oxides: an Introduction to their Electronic Structure and Properties*. Oxford University Press, New York, NY, 2010.

[55] E.K.H. Salje, A.S. Alexandrov, and W.Y. Liang, *Polarons and Bipolarons in High-T_c Superconductors and Related Materials*. Cambridge University Press, New York, NY, 2005.

[56] A.J. Lewis, "Use of Hydrogenation in the Study of the Transport Properties of Amorphous Germanium," *Phys. Rev. B*, **14** [2] 658–668 (1976).

[57] D. Emin, "Phonon-Assisted Jump Rate in Noncrystalline Solids," *Phys. Rev. Lett.*, **32** [6] 303–307 (1974).

[58] E. Gorham-Bergeron and D. Emin, "Phonon-assisted Hopping due to Interaction with Both Acoustical and Optical Phonons," *Phys. Rev. B*, **15** [8] 3667–3680 (1977).

[59] J.A. Bock, S. Trolier-McKinstry, G.D. Mahan, and C.A. Randall, "Polarization-based Perturbations to Thermopower and Electronic Conductivity in Highly Conductive Tungsten Bronze Structured (Sr,Ba)Nb_2O_6: Relaxors vs Normal Ferroelectrics," *Phys. Rev. B*, **90** [11] 115106–1 – 115106–8 (2014).

[60] W.D. Callister and D.G. Rethwisch, *Materials Science and Engineering: An Introduction*, 8th ed. John Wiley & Sons, Hoboken, NJ, 2009.

[61] N.F. Mott and E.A. Davis, *Electronic Processes in Non-Crystalline Materials*. Oxford University Press, New York, NY, 2012.

[62] D. MacDonald, *Thermoelectricity: an Introduction to the Principles*. Dover Publications, Mineola, New York, 2006.

[63] H.K. Rockstad, R. Flasck, and S. Iwasa, "Seebeck Coefficient in Amorphous Chalcogenide Films," *J. Non. Cryst. Solids*, **8-10** 326–330 (1972).

[64] P.M. Chaikin and G. Beni, "Thermopower in the Correlated Hopping Regime," *Phys. Rev. B,* **13** [2] 647–651 (1976).

[65] P.G. Dickens and M.S. Whittingham, "The Tungsten Bronzes and Related Compounds," *Q. Rev. Chem. Soc.*, **22** 30–44 (1968).

[66] A. Magnéli, "The Crystal Structure of Tetragonal Potassium Tungsten Bronze," *Ark. Kemi*, **1** [3] 213–221 (1949).

[67] G. Hagg and A. Magneli, "Recent Structure Investigations of Oxygen Compounds of Molybdenum and Tungsten," *Rev. Pure Appl. Chem,* **4** 235–249 (1954).

[68] P.B. Jamieson, "Ferroelectric Tungsten Bronze-Type Crystal Structures. I. Barium Strontium Niobate $Ba_{0.27}Sr_{0.75}Nb_2O_{5.78}$," *J. Chem. Phys.*, **48** [11] 5048–5057 (1968).

[69] M.H. Francombe and B. Lewis, "Structural, Dielectric and Optical Properties of Ferroelectric Lead Metaniobate," *Acta Crystallogr.*, **11** [10] 696–703 (1958).

[70] D.C. Arnold and F.D. Morrison, "B-cation Effects in Relaxor and Ferroelectric Tetragonal Tungsten Bronzes," *J. Mater. Chem.*, **19** [36] 6485–6488 (2009).

[71] W.H. Huang, D. Viehland, and R.R. Neurgaonkar, "Anisotropic Glasslike Characteristics of Strontium Barium Niobate Relaxors," *J. Appl. Phys.,* **76** [1] 490–496 (1994).

[72] K.L. Ngai and T.L. Reinecke, "Structural Instabilities and Superconductivity in the Alkali Tungsten Bronzes," *J. Phys. F Met. Phys.*, **8** [1] 151–160 (1978).

[73] X.H. Zheng and X.M. Chen, "Dielectric Ceramics with Tungsten-bronze Structure in the $BaO–Nd_2O_3–TiO_2–Nb_2O_5$ System," *J. Mater. Res.*, **17** [07] 1664–1670 (2002).

[74] L.E. Cross, "Relaxor Ferroelectrics," *Ferroelectrics,* **76** [1] 241–267 (1987).

[75] F.W. Ainger, J.A. Beswick, W.P. Bickley, R. Clarke, and G. V Smith, "Ferroelectrics in the Lithium Potassium Niobate System," *Ferroelectrics,* **2** [1] 183–199 (1971).

[76] R.R. Neurgaonkar and L.E. Cross, "Piezoelectric Tungsten Bronze Crystals for SAW Device Applications," *Mater. Res. Bull.*, **21** [8] 893–899 (1986).

[77] J.V. Hessen, B. Sunshine, S.A., Siegrist, T. Fiory, A.T., Waszczak, "Structure and Properties of Reduced Barium Niobium Oxide Single Crystals Obtained from Borate Fluxes," *Chem. Mater,* **3** [16] 528–534 (1991).

[78] M.P. Leffler, "A Study of Positional Disorder in Strontium Barium Niobate;" M.S. Thesis, Pennsylvania State University, 1989.

[79] X.L. Zhu, K. Li, and X.M. Chen, "Ferroelectric Transition and Low-Temperature Dielectric Relaxations in Filled Tungsten Bronzes," *J. Am. Ceram. Soc.*, **97** [2] 329–338 (2014).

[80] M.. Trubelja, E. Ryba, and D.K. Smith, "A Study of Positional Disorder in Strontium Barium Niobate," *J. Mater. Sci.*, **31** 1435–1443 (1996).

[81] A.A. Ballman and H. Brown, "The Growth and Properties of Strontium Barium Metaniobate, $Sr_{1-x}Ba_xNb_2O_6$, a Tungsten Bronze Ferroelectric," *J. Cryst. Growth*, **1** [5] 311–314 (1967).

[82] A.S. Bhalla, R. Guo, L.E. Cross, G. Burns, F.H. Dacol, and R.R. Neurgaonkar, "Measurements of Strain and the Optical Indices in the Ferroelectric $Ba_{0.4}Sr_{0.6}Nb_2O_6$: Polarization Effects," *Phys. Rev. B*, **36** [4] 2030 (1987).

[83] J.R. Carruthers and M. Grasso, "Phase Equilibria Relations in the Ternary System BaO-SrO-Nb_2O_5," *J. Electrochem. Soc.*, **117** [11] 1426–1430 (1970).

[84] O.G. D'yachenko, S.Y. Istomin, A.M. Abakumov, and E. V. Antipov, "Synthesis, Structure, and Properties of Mixed Niobium(IV,V) Oxides," *Inorg. Mater.*, **36** [3] 247–259 (2000).

[85] N.C. Stephenson, "The Crystal Structure of the Tetragonal Bronze, $Ba_6Ti_2Nb_8O_{30}$," *Acta Crystallogr.*, **18** [3] 496–501 (1965).

[86] S. Lee, R.H.T. Wilke, S. Trolier-McKinstry, S. Zhang, and C.A. Randall, "$Sr_xBa_{1-x}Nb_2O_{6-\delta}$ Ferroelectric-thermoelectrics: Crystal Anisotropy, Conduction Mechanism, and Power Factor," *Appl. Phys. Lett.*, **96** [3] 031910–1 – 031910–3 (2010).

[87] M. Tachibana and E. Takayama-Muromachi, "Thermal Conductivity and Heat Capacity of the Relaxor Ferroelectric $[PbMg_{1/3}Nb_{2/3}O_3]_{1-x}$ $[PbTiO_3]_x$," *Phys. Rev. B*, **79** [10] 100104–1 – 100104–4 (2009).

[88] E. Fischer, W. Hässler, and E. Hegenbarth, "Glass-Like Behaviour in the Thermal Conductivity of $Sr_{1-x}Ba_x(Nb_2O_6)$ Single Crystal," *Phys. status solidi*, **72** [2] K169–K171 (1982).

[89] C.L. Choy, W.P. Leung, T.G. Xi, Y. Fei, and C.F. Shao, "Specific Heat and Thermal Diffusivity of Strontium Barium Niobate ($Sr_{1-x}Ba_xNb_2O_6$) Single Crystals," *J. Appl. Phys.*, **71** [1] 170–173 (1992).

[90] S.R. Gilbert, L.A. Wills, B.W. Wessels, J.L. Schindler, J.A. Thomas, and C.R. Kannewurf, "Electrical Transport Properties of Epitaxial $BaTiO_3$ Thin Films," *J. Appl. Phys.*, **80** [2] 969–977 (1996).

[91] S.W. Robey, L.T. Hudson, C. Eylem, and B. Eichorn, "Substitution-induced Midgap States in the Mixed Oxides RxBa1− xTiO3− δ with R= Y, La, and Nd," *Phys. Rev. B*, **48** [1] 562–567 (1993).

[92] M. Cutler and N.F. Mott, "Observation of Anderson Localization In an Electron Gas," *Phys. Rev.*, **181** [3] 1336–1340 (1969).

Chapter 3

Experimental Procedure

The sintering of powders was used to fabricate ceramic (polycrystalline) samples of different compositions in the SBN system. Powders were fabricated by a conventional solid-state reaction process without additional binders, surfactants, or dispersants. This process is favorable due to low processing costs with large yields that can sinter to appropriate densities for electrical measurements. This section will outline the details for powder processing, green body formation, sintering and density measurements. Characterization techniques such as particle size measurement, X-ray diffraction (XRD), electron microscopy, electrical conductivity, Seebeck coefficient, and the Hall measurement will also be described.

3.1 Powder Processing and Synthesis

Solid state reaction of powders was used to fabricate ceramic samples using a process similar to that described for preparation of 5-site filled SBN ceramics in previously reported work[1–4]. Raw powders of high purity were used as starting materials: 99.9% wt% $SrCO_3$ (Sigma-Aldrich), 99.9 wt% Nb_2O_5 (Alfa Aesar), and 99.9 wt% $BaCO_3$ (Alfa Aesar), respectively. Stoichiometric compositions of SBN for 6-site filling (filled bronze) were batched for compositions of varying Sr and Ba ratios at intervals of 20 mole%. The notation 0:100 will be used to describe the Ba end member, and 100:0 the Sr end member, respectively. Each batch was measured on a mass balance with a resolution of 0.0001 g. The raw powders were then transferred into a rounded-bottom Nalgene ® bottle with ZrO_2 milling media of varying sizes ranging from 1 to 5 mm in diameter. 200 proof ethanol was used as the milling liquid. Ball-mill processing conditions are well-documented in the literature and nano-sized powders can be achieved using this process[5, 6]. However, in this

study, nano-sized powders were not necessary; the only requisite was for aggregates to be broken up to particle sizes between 0.1 and 1 μm. It was found that a volume ratio of 1:1:1 for the media, the powders, and the ethanol was able to consistently meet this goal. The setup is shown in Figure 3-1. The raw powders were intimately mixed using the Nalgene® bottle for 24 hours by rotational motion using a roller mill at 200 RPM.

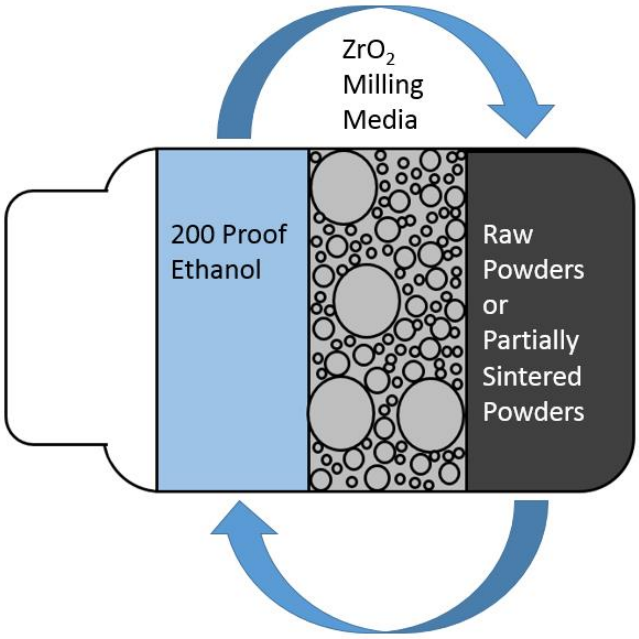

Figure 3-1. Setup for intimate mixing of high purity starting oxide powders. The volume ratio for media, powder, and liquid was 1:1:1 respectively. A mixture of sizes was used for the milling media.

After milling for 24 hours, the suspension was poured through a strainer and into a commercial glass pan in order to separate the milling media. The pan was then covered with aluminum foil and placed in a drying oven at 80°C for 12 hours. The aluminum foil was lifted at the corner in order for the ethanol to evaporate efficiently. The glass dish was then removed from the oven unless the evaporation of the ethanol was not completed within 12 hours. A rubber spatula was then used to transfer the powder from the glass pan into a number 50 (300 μm mesh size) sieve. The powder mixture was then sieved; the process also broke up weakly bonded agglomerates formed during drying, such that a high surface area was achieved in order to prepare for the next step.

The sieved powder mixture was then placed into alumina boats and calcined in air in a box furnace at 850°C for 8 hours at a ramp rate of 5°C/min to remove the carbon. Figure 3-2 shows the XRD pattern after calcination with carbonates absent.

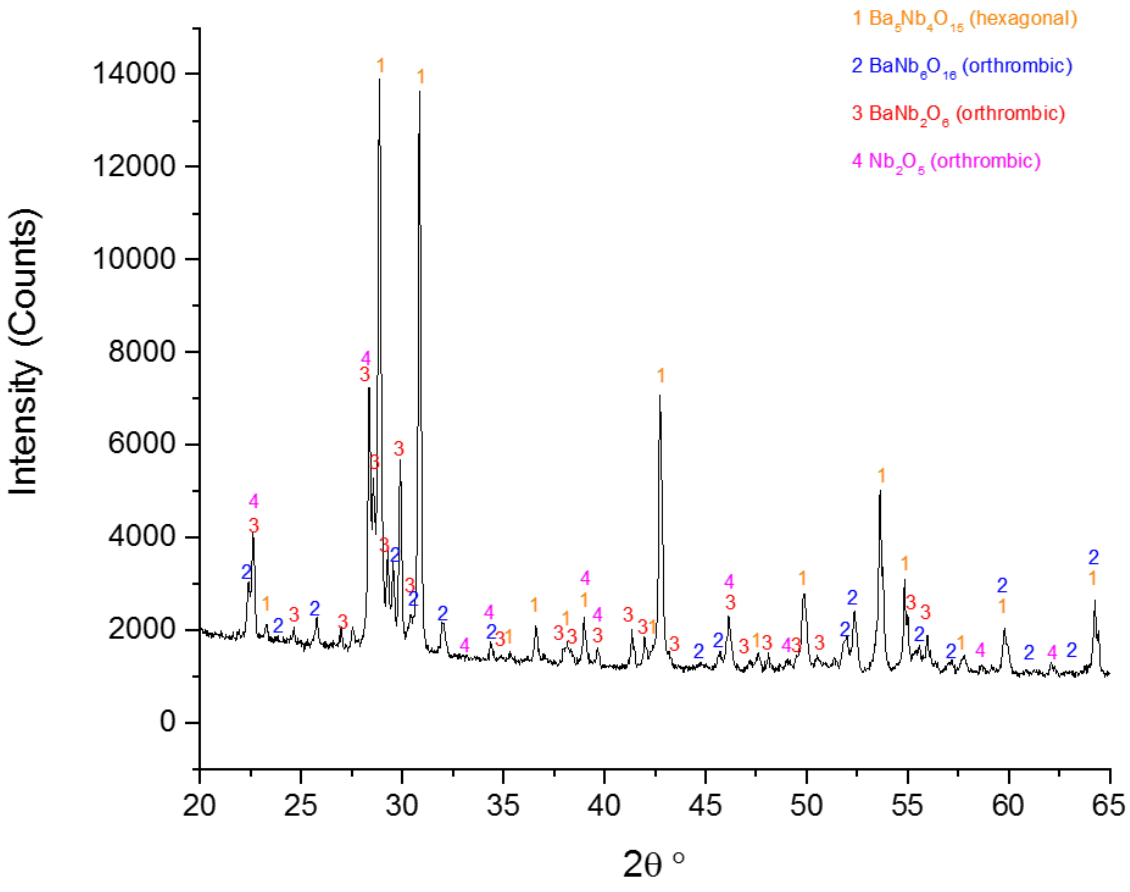

Figure 3-2. No evidence of carbonates after 850°C air calcination of powder mixture. Many of the oxides identified have overlapping diffraction peaks.

At 850°C, the powder has not sintered and does not need to be milled. This powder mixture was then reacted into the tungsten bronze phase under a reducing atmosphere. For this task, the powder was placed into a 90 x 17 x 11.5 mm alumina combustion boat and into a tube furnace with reducing gas capabilities. A schematic of the tube furnace is shown in Figure 3-3.

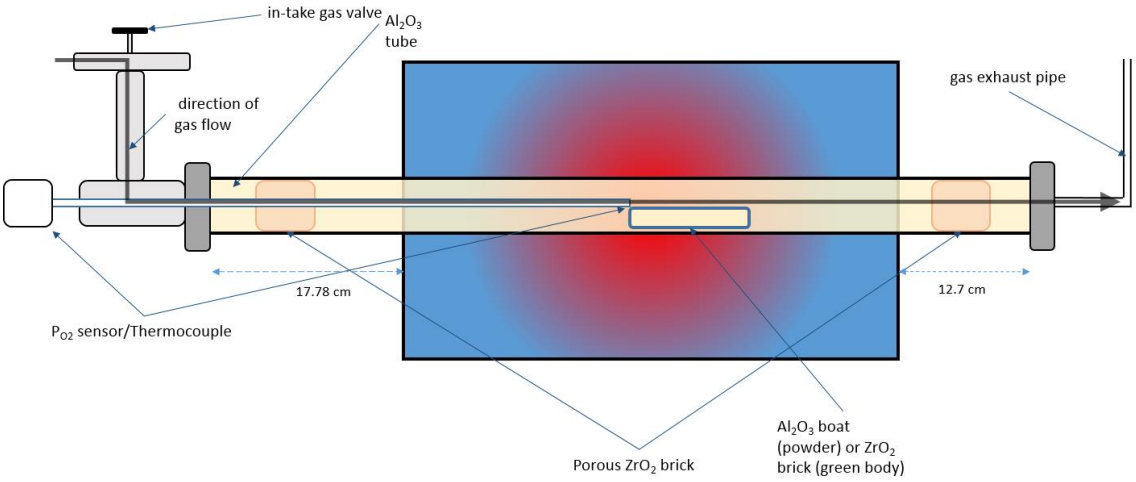

Figure 3-3. The reducing tube furnace system used in powder processing and sintering. The reducing atmosphere was controlled by H_2 gas and water vapor carried by inert Ar gas. An R-type thermocouple coupled with a ZrO_2 oxygen-sensor probe was inserted along the gas-intake end.

A smaller boat of 12.4 x 25 x 100 mm was used because significant distance deviation from the furnace's hot zone (either by too large a boat or shifting of the tube within the furnace) may lead to an oxygen-gradient as a consequence of inadequate temperatures as shown in Figure 3-4.

Figure 3-4. The degree-of-reduction gradient depicted by color gradient when too far away from hot zone.

The alumina boat was pushed along the tube towards the tip of thermocouple with a hooked metal rod from the exhaust side. A porous ZrO_2 brick was placed into each end of the tube. A small fan was also placed externally at each end. The purpose of this was to insulate the ends from the heating elements and to cool the ends such that thermal

expansion of the tube near the ends was minimized, reducing the chance of atmospheric leakages. The ends of the tube were sealed with endcaps. The in-take endcap also houses the oxygen and temperature sensor, as shown in Figure 3-3.

The reducing capabilities of the furnace were controlled by the use of H_2, "wet" (water vapor-carrying) Ar, and "dry" Ar using a total flow rate of 500 cm^3/min. This flow rate for the tube maintains a pressure of 1 atm within the furnace. The "dry" Ar acts as a carrier gas. The partial pressure of oxygen can then controlled by the equilibrium reaction[7]:

$$H_2\,(g) + \frac{1}{2}O_2\,(g) \leftrightarrow H_2O\,(g) \qquad \textbf{(Eq 3.1)}$$

The corresponding law of mass action expression is then:

$$K(T) = \frac{pH_2 pO_2^{\frac{1}{2}}}{pH_2O} \qquad \textbf{(Eq 3.2)}$$

where p denotes partial pressures. There is a standard free energy of formation, $\Delta G°$, associated with Eq 3.1 and it can be related to the equilibrium constant in Eq 3.2. It is given as follows:

$$\Delta G° = RTln(K) \qquad \textbf{(Eq 3.3)}$$

The standard state of the free energy for the forward reaction in Eq 3.1 is given (in J/mol) as[7]:

$$\Delta G°(T) = -247500 + 55.85T \qquad \textbf{(Eq 3.4)}$$

Eq 3.4 is valid for the temperature range from 298 to 2000 K. The equilibrium constant is temperature dependent as indicated in Eq 3.2. From Eq 3.3 and Eq 3.4, the temperature dependence of K(T) can be expressed as:

$$ln(K) = -\frac{\Delta G°(T)}{RT} \qquad \textbf{(Eq 3.5)}$$

where R= 8.314462 J/mol-K. Table 3.1 shows values of ln(K) by substitution of values of T into Eq 3.4. Plotting the natural logarithm of K vs 1/T will give the linear expression of ln(K) as a function of T:

Table 3.1 Tabulated values of ln(K) vs 1/T

Temperature (K)	Reciprocal Temperature (K^{-1})	Calculated Standard Gibbs Free Energy (J/mol)	ln(K)	K
300	0.00333	-230745	-92.5075	6.67587E-41
600	0.00167	-213990	-42.8951	2.34897E-19
900	0.00111	-197235	-26.3577	3.57274E-12
1000	0.00100	-191650	-23.0502	9.75946E-11
1200	0.00083	-180480	-18.0890	1.39336E-08
1500	0.00067	-163725	-13.1277	1.9893E-06
1800	0.00056	-146970	-9.8202	5.43406E-05

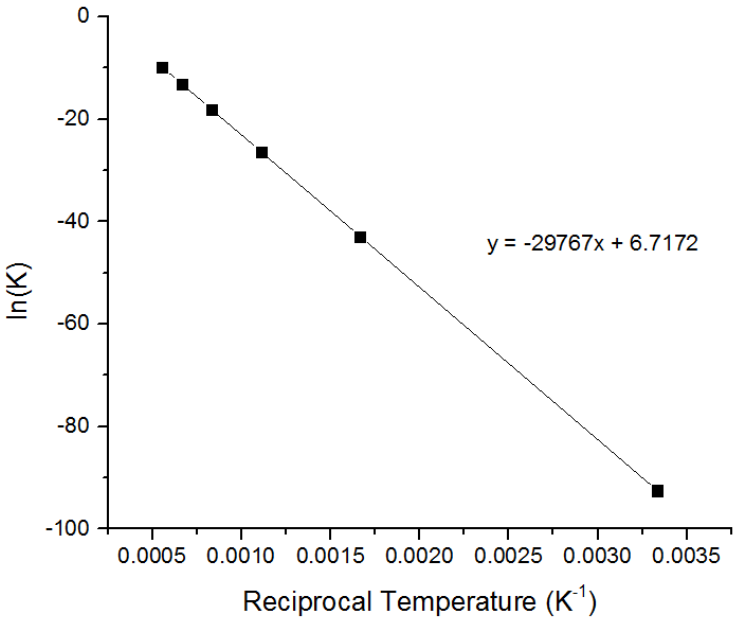

Figure 3-5. The linear relationship between the natural log of the equilibrium constant plotted against the reciprocal of absolute temperature. The linear trend gives the values for the constants A and B in Eq 3.5, which can be used to calculate K as a function of T.

Plotted in this way, the equilibrium constant can then be expressed linearly as:

$$ln(K) = A - \frac{B}{T} \quad \textbf{(Eq 3.6)}$$

where $A = 6.7172$ and $B = -29767$. Knowing the value of K at different temperatures then allows calculation of the partial pressures at different temperatures, and hence the flow rates for the gases for a desired pO_2. This calculation was also verified with a ZrO_2 sensor.

The reaction or second calcination was performed at 1300°C for 10 hours using a ramp up and ramp down of 5°C/min under a gas flow of 12.5 cc/min H_2 and 487.5 cc/min dry (equivalent to 2.5% H_2 in Ar.) The gas flow rates are manually adjusted by a MKS Instruments® mass flow controller. The reduced powder was then removed from the alumina boat with a metal spatula. Hard scraping was avoided to reduce Fe contamination. The partially sintered powder was then placed into another Nalgene® bottle with ethanol and ZrO_2 milling media as described during the mixing step (Figure 3-1). This bottle was then put into a large plastic canister and placed into a high-energy vibratory mill for a total of 36 hours. After the first 18 hours, the Nalgene® bottle was taken out and vigorously shaken by hand for 10 seconds and placed back into the mill for the remaining 18 hours. This process eliminates any potential unmilled aggregates near the bottom of the bottle as a consequence of unequal contact with the media. The slurry was then placed in an 80°C oven for drying for 12 hours or until all of the ethanol has been removed. The powder was then sieved using a number 325 (45 μm mesh size) sieve. Figure 3-6 shows the overall process for powder synthesis

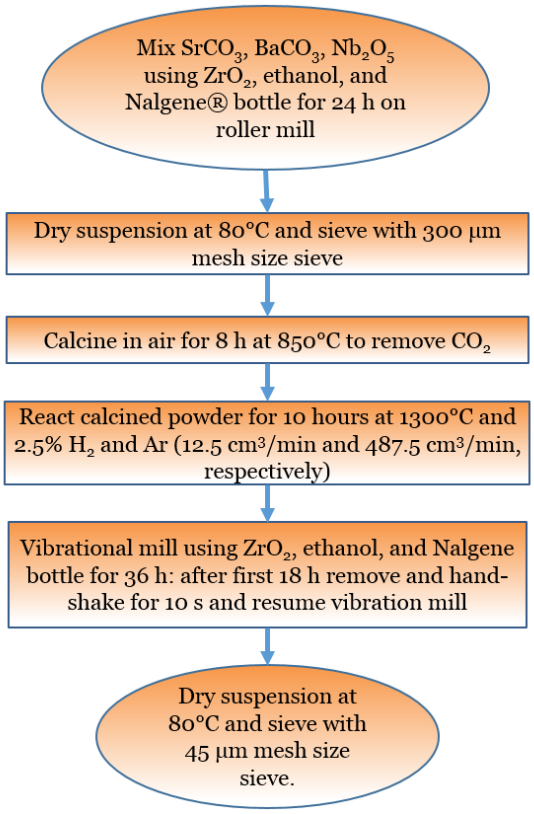

Figure 3-6. Overview of steps for powder synthesis before sintering. This processing method for the powders yields densities > 95% after sintering. Additives such as binders, dispersants, and surfactants were not required to achieve this density.

3.2 Particle Size Measurement

Particle sizes were measured using a Malvern Nanosizer® ZS instrument that utilized dynamic light scattering. The instrument, as reported by the manufacturer, is suitable for measurements from 0.6 nm to 6 µm. The final reduced powders were dispersed in de-ionized water and ultrasonicated for 50 minutes, or until the dispersion showed no signs of settled particulates, whichever occurred first. The dispersion was extracted using plastic pipettes into glass cuvettes and measured. A refractive index of 2.3, as reported in the literature, was used for all powders[8]. Three measurements were taken to assess the error in the measured particle size distribution.

3.3 Green Body Formation, Sintering, and Annealing

The reduced powders were formed into circular green bodies by hydraulic pressing through a die followed by cold isostatic pressing (CIP.) A stainless steel die of 12 mm inner diameter was used in the uniaxial hydraulic press. Stearic acid dissolved in acetone was used as the lubricant. Powders were measured on a mass balance to 1.150g (2.75 mm thickness) or to 0.600g (1.38 mm thickness) and uniaxially pressed at 2 ksi (13.8 MPa) for 30 seconds. The resulting pellet was ejected by pressing on the opposite side of the die. A low pressure of 2 ksi was used, since the hydraulic press was only used to form the shape. High uniaxial pressures can cause density gradients to develop during the sintering process[9]. The uniaxially pressed pellets were then vacuum-sealed in a nitrile glove or plastic covering and isostatically pressed at 29 ksi (199.9 MPa) for 30 seconds. The holding vessel was patted dry before removing the isostatically pressed pellets. The resulting green body takes the form of a high-strength circular pellet.

The green bodies were sintered in the reducing furnace described in the powder synthesis section. The green bodies were placed on top of a porous ZrO_2 brick and pushed as close as possible to the thermocouple. The green bodies were sintered at 1350°C for 5 hours using a ramp up and ramp down rate of 5°C/min under a gas flow of 2.5% H_2 in Ar (12.5 cm^3/min and 487.5 cm^3/min, respectively.) In samples that underwent annealing after sintering, these samples were annealed for 30 hours at 1300°C at 5°C/min ramp up/down using either 2.5% H_2 in Ar or an annealing atmosphere of 1.02×10^{-14} atm pO_2 (30, 20, and 450 cm^3/min, for H_2, wet Ar, and dry Ar, respectively.) The process for green forming and the sintering profile are shown in Figure 3-7.

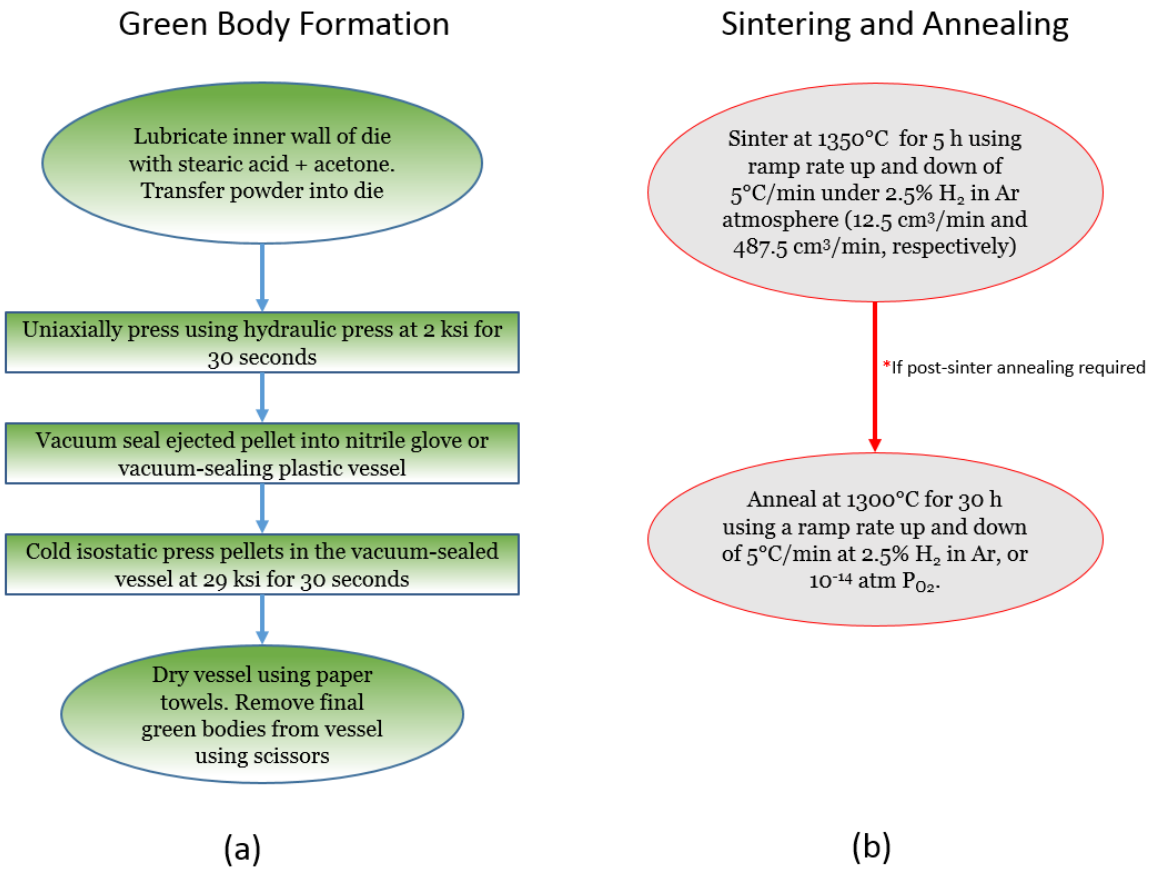

Figure 3-7. (a) Green body formation by two step dry-pressing and (b) sintering and post-sinter annealing profiles.

3.4 Density Measurements

The densities of pellets were measured using the Archimedes method. At room temperature, the density of DI water was assumed to be 1.0g/cm^3 such that the mass and volume in cm^3 can be used interchangeably. A specialized configuration involving a beaker of water and an overhanging sample holder was used to conduct the Archimedes density measurement as shown in Figure 3-9.

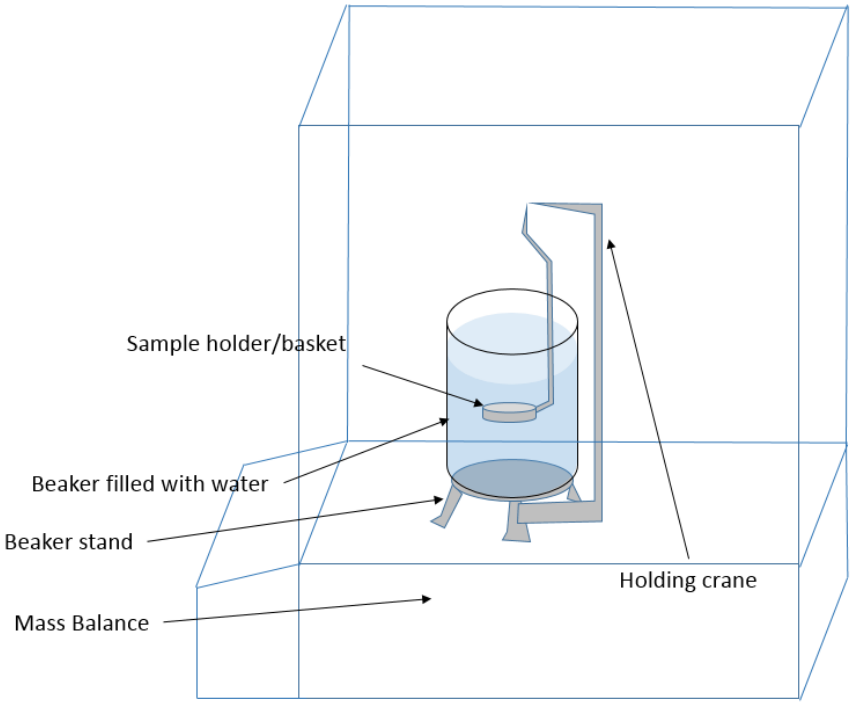

Figure 3-9. Archimedes setup for determining densities.

The following equation was used to determine densities[10]:

$$\rho = \frac{D}{S - I} \qquad \textbf{(Eq 3.7)}$$

where ρ is the measured density in g/cm^3, D is the dry weight of the sample, S is the water-saturated weight of the sample, and I is the immersed-water-saturated weight

As-sintered pellets were dried in an oven for 120°C for 20 minutes in order to evaporate any moisture. This dry weight is the D in Eq 3.7. To obtain S, the samples were placed into a beaker of boiling water heated by a hot plate for 2 hours or until all air bubbles from the sample surface were eliminated. Any water adhering to the samples that was not absorbed by surface porosity was patted away with a damp paper towel before measuring the mass. The immersed-saturated weight, I, was measured by using the setup in Figure 3-9. The saturated sample was placed into the basket that will measure the weight of the sample under the influence of the buoyant force. The subtraction of S and I will yield the volume of the sample with the surface porosity taken into account via water displacement.

Theoretical densities were calculated by the following equation:

$$\rho_{th} = \frac{MZ}{V_c N_A} \quad \textbf{(Eq 3.8)}$$

where ρ_{th} is the theoretical density, M is the molar mass of the tungsten bronze for a given composition, Z is the number of chemical formula units per unit cell, V_c is the unit cell volume obtained from XRD, and N_A is Avogadro's number. From Eq 3.7 and 8, the relative density can then be calculated as follows:

$$\rho_{rel}(\%) = 1 - \left(\frac{\rho_{th} - \rho}{\rho_{th}} \times 100\right) \quad \textbf{(Eq 3.9)}$$

3.5 Sample Preparation

Four types of samples were prepared from the sintered pellet: electrical conductivity, Seebeck, Hall, and microstructure. The circular pellets were mounted using Crystalbond™ glue onto an alumina sheet. A 0.2 mm thick diamond saw blade spinning at 30 rpm was used to cut sections of the pellet into rectangular prisms. The Seebeck samples were cut to the dimensions of 1 x 1 x 5 mm. The Hall and electrical conductivity samples were larger to facilitate electroding and were usually cut from the center of the pellet. The side wedges were used for characterization of the microstructure. Figure 3-8 shows a general guide for the types and size of samples cut from a single pellet.

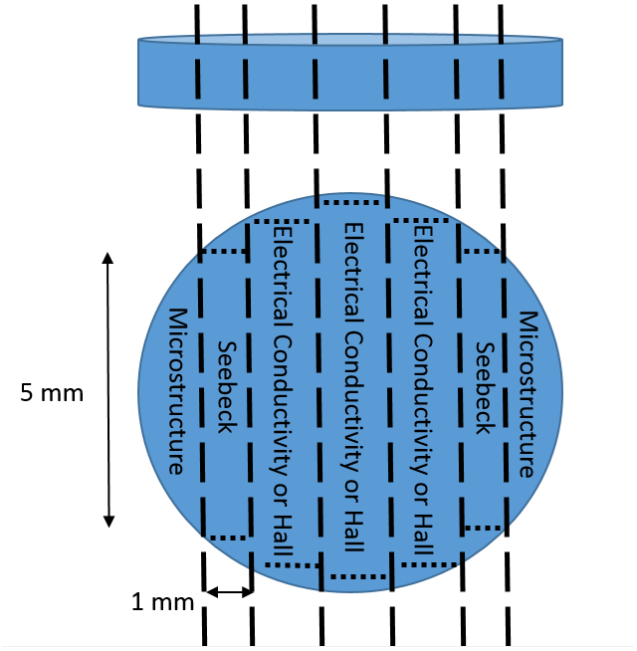

Figure 3-8. Four types of samples cut from a sintered pellet. Only the Seebeck samples require a specific dimension.

With the exception to the pieces cut for electron microscopy, the samples were ground on all 6 faces with 400 grit (~ 22 µm) and then 600 grit (~ 14 µm) SiC paper using a grinding wheel. This flattens the surfaces and leaves enough surface roughness for robust adhesion of sputtered electrodes. Samples were ultra-sonicated in DI water between grit size changes for 30 seconds. Samples were removed from the steel grinder-stages using acetone, followed by another ultra-sonication in DI water for 30 seconds.

Microstructural samples were prepared by grinding and polishing of the cross-sectional surface, e.g. the interior face. These samples were ground using 240, 320, 400, 600 grit (52, 35, 22, 14 µm, respectively) SiC and polished with 800 (10 µm) and 1000 (5 µm) grit SiC. The samples were ground until the previous grit size scratches disappeared. The samples were then polished with the 800 grit SiC for 5 minutes or until scratches from the previous grit disappeared. Polishing with the 1000 grit was performed for 10 minutes, which should yield a mirror-like surface, or until scratches from the previous grit disappeared. Between each grit size change, the samples were ultra-sonicated in DI water for 30 seconds.

3.6 Electron Microscopy and Energy Dispersive Spectroscopy

Electron micrographs were taken using an FEI™ Quanta 200 environmental Scanning Electron Microscope (ESEM) with an auxiliary Oxford Instruments® Energy Dispersive Spectrometry (EDS) detector as well as another FEI™ SEM (NanoSEM 600) using a field emission source (FESEM.) In all cases, samples were loaded on to SEM stage stubs using double-sided carbon tape. Sputter coating was not used. Micrographs on the ESEM were taken using the high vacuum mode, a working distance of ~ 11 mm, and 20 kV with a probe current of 3.0 nA. Micrographs taken on the FESEM used a working distance of ~ 2 mm, 2.5 kV accelerating voltage, and a probe current of 18 pA. EDS results were analyzed with the Aztec® software. Settings for EDS characterization were as follows: 25 kV accelerating voltage, a probe current of 4.7 nA, and a working distance of 12 mm. A 5-site SBN of 61:39 Sr:Ba single crystal was used as an external standard for quantitative work.

Transmission electron microscopy micrographs were taken using the FEI™ Titan G3 microscope under the scanning transmission electron microscopy (STEM) mode operated at 300 kV. The EDS attachment was used for elementally mapping the micrographs.

3.7 X-ray Diffraction

X-ray diffraction was performed using the Bragg-Brentano geometry on a PANalytical Empyrean system. In all diffraction experiments, a Cu target under an accelerating voltage of 45 kV and current of 40 mA utilized. A Ni filter was used to minimize the K_β radiation. Additional accessories include a 10 mm beam mask, a ½° anti-scatter slit, and an attachable beam knife that serves to minimize the background at low

diffraction angles. Settings for the goniometer were as follows: scan range from 5-70° 2θ, a time step of 100 seconds, and a step size of 0.0263°.

For powder XRD, the flat-stage attachment was used. The powders were mixed with a Ni standard (Alfa Aesar) at about 10wt%. The mixing process consisted of using a mortar and pestle until the powder was a uniform color. The mixed powder was then loaded onto a specially-oriented flat "zero-background" Si stage with a circular depression. For bulk samples, the multi-stage attachment was used. Here, instead of using Si, a "zero-background" quartz crystal was used. The height of the sample surface was calibrated to mm relative to the X-ray source using a height-aligning tool.

All XRD data analysis such as Rietveld refinements and peak identification were performed on Jade® 2010.

3.8 Electrical Conductivity

Electrical conductivity measurements as function of temperature were performed using a 4-point probe technique. The advantage of this technique over the 2-point probe technique is that contributions from the lead and contact resistances are minimized. The conductivity of the sample was calculated by measuring the resistance due to the potential drop between the two inner electrodes for a rectangular specimen. Figure 3-10 shows the 4 point-probe geometry.

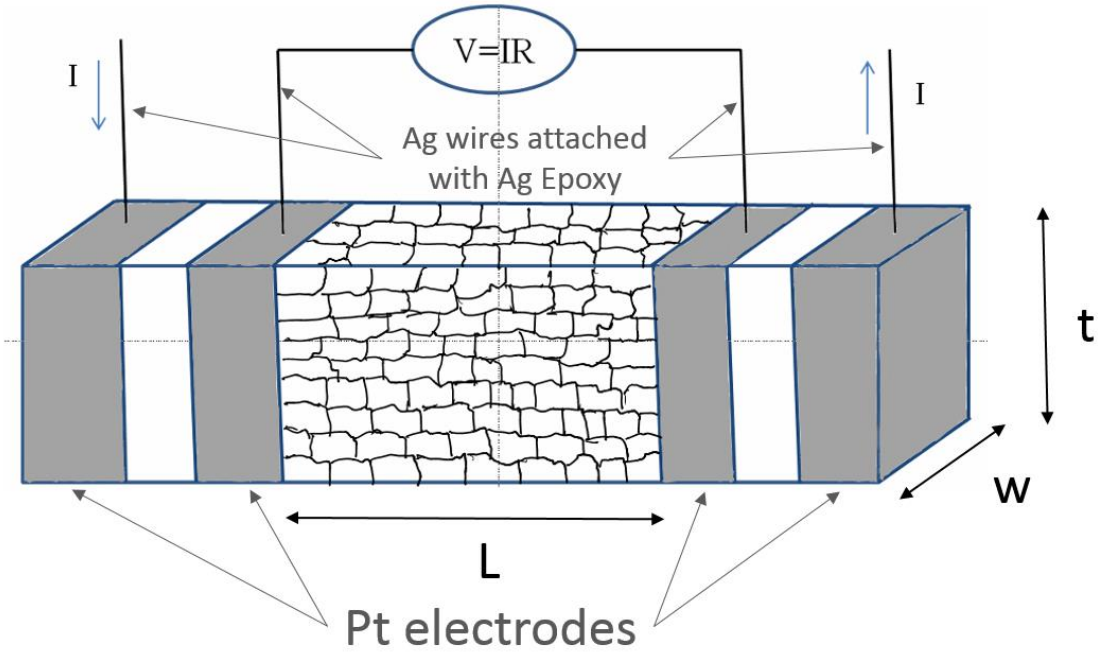

Figure 3-10. 4-point probe setup for measuring electrical conductivities. Current was supplied to the outer electrodes and the potential drop was measured across the two inner electrodes.

A Quorum Technologies® sputter system was used to sputter 100 nm of Pt onto the samples. The sample was masked using Kapton tape. Epo-Tek® Ag epoxy (resin + hardener in 1:1 ratio) was used to attach Ag wires onto the electrodes. The Kapton tape was left on the sample from the sputtering so that the Ag epoxy can be applied without causing unintentional shorting. The Ag epoxy was cured at 120°C for 15 minutes.

Electrical conductivities were measured using two different systems: one for temperatures of 200°C and below and another for 25°C to 700°C. The low temperature measurements used a combination of a Hewlett Packard® LCR meter, a Keithley® digital multimeter (DMM) with cold-junction compensator for temperature measurement, and a liquid N_2-compatible enclosure. The Ag wires of the sample were soldered onto the leads of the sample box that attached to the oven door. The oven door connects to the LCR meter and the DMM. The Pennsylvania State University's GADD software was used to record the resistance and temperature. A heating and cooling rate of 2°C/min was used and the cooling measurement was reported.

For high temperature measurements, a reducing furnace was used. A Tektronix® Keithley DMM and 4-point probe apparatus with K-type thermocouple were used. The Ag wires of the sample were twisted separately around the four independent Pt leads of the apparatus for good contact. The furnace controller was programmed to heat at 2°C/min from room temperature to 700°C, hold for 1 h at 700°C, and then cool at 2°C/min. A gas flow of 15 cm^3/min of H_2 and 485 cm^3/min N_2 was used to create the reducing atmosphere during the measurement. Electrical resistance and temperatures were logged using the EXCEL-Link add-on to Microsoft® Excel. The measurement on cooling is reported since there was a hysteresis between the heating and cooling curves. This was thought to be a consequence of polymer degradation of the silver epoxy at higher temperatures or possible oxidation. Subsequent measurements on the same sample did not show the hysteresis.

The electrical conductivity was calculated by the resistance as measured on either of the low T or high T systems using the dimensions shown in Figure 3-10. The conductivity is then:

$$\sigma = \left(\frac{Rwt}{L}\right)^{-1} \qquad \textbf{(Eq 3.10)}$$

where σ is the electrical conductivity, R is the measured resistance, w is the width, t is the thickness, and L is the distance between the two inner electrodes. Comparison of the low T system and high T system for the Ba end member is shown in Figure 3-11. There was good overlap between the two systems, suggesting that 2 °C/min was adequate to avoid any discontinuity due to thermal equilibrium.

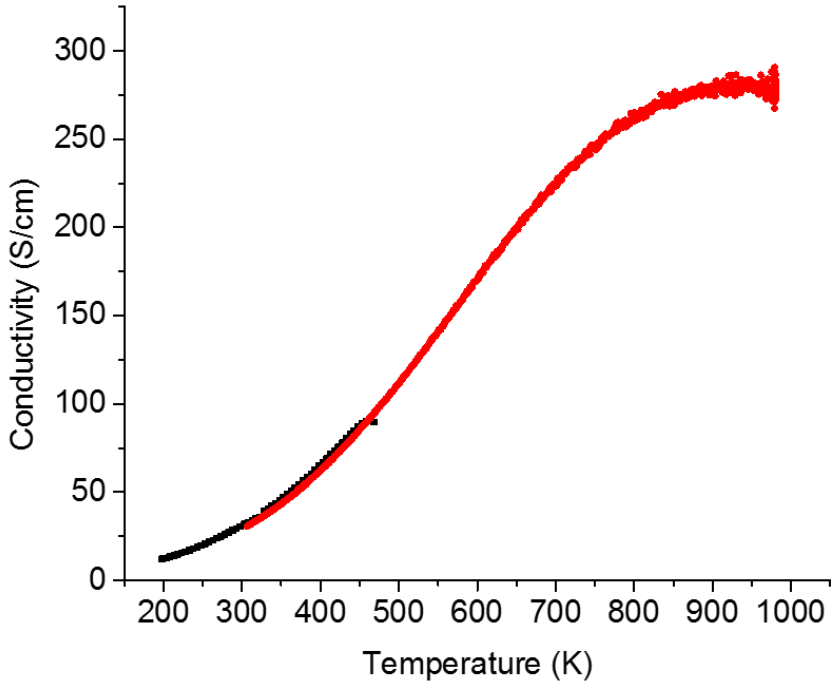

Figure 3-11. The overlapping of electrical conductivity of the low T system (black) and the high T system (red) for one case of fabricated Ba end member (BNO) as-sintered. Sample was sintered under 2% H_2 in N_2 for 2 h at 1300°C.

3.9 Seebeck Coefficient

Seebeck measurements were performed on a commercial MMR-Tech ® Seebeck system. The system's three major components are an SB-100 controller, a K-20 controller, and a vacuum chamber that houses the connections between the sample stage, heater, and electronics. Ti-Pt (30 nm, 100 nm, respectively) electrodes were sputtered onto Seebeck samples using a Kurt Lesker® CMS-18 sputter coater. The samples were attached to a commercially-supplied alumina circuit board-stage using Ted Pella® Ag conductive paste as shown in Figure 3-12. The paste was cured at 120 °C for 15 minutes. The K-20 controller controls the overall temperature of the measurement while an SB-100 controller both powers a localized auxiliary heater that creates the temperature gradient as well as measures the thermoelectric voltages.

The theory of operation is as follows: a reference (constantan alloy) with a known Seebeck coefficient dependence on temperature, is used to assess the Seebeck coefficient of the sample. This assumes that the temperature gradient along the reference and the sample are the same. (This is the rationale behind symmetrical sample loading on the stage as well as the necessity of the specific dimensions of the Seebeck sample). If this is true, then the Seebeck coefficient of the sample is given as:

$$\alpha_S = \frac{V_S}{\Delta T_{PS}} = \frac{V_S}{\Delta T_{PR}} = \frac{V_S \alpha_R}{V_R} \qquad \textbf{(Eq 3.11)}$$

where α_S and α_R is the Seebeck coefficient of the sample and reference, respectively; V_S and V_R are the thermoelectric voltages of the sample and reference, respectively; and ΔT_{PS} and ΔT_{PR} are the temperature gradients of the sample and reference, respectively.

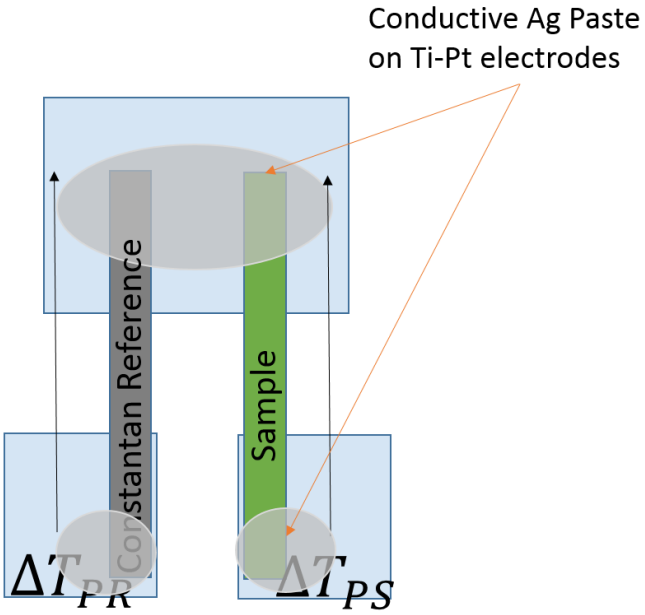

Figure 3-12. Sample loading on the MMR-Tech® Seebeck stage to help achieve equal temperature gradients.

The alumina stage was inserted into the vacuum chamber according to operating procedures and secured with thermal grease and a copper clip to ensure good thermal contact under a vacuum environment. The chamber was vacuum-sealed using a pump to ~ 2 mTorr. An integrated software package was used to program the measurement.

3.10 Hall Measurement

The carrier concentration was measured using the Hall effect on a Quantum Design® PPMS system. Hall samples were electroded with Pt using the Quorum® sputter coater as outlined in the electrical conductivity section. Five electrode contacts were made on each Hall sample. For more resistive samples, painted Ga-In electrodes were used.[1]The composition of the Ga-In alloy was approximately 50-50 by volume % and was adjusted with incrementally more Ga such that the alloy could melt on a 80°C hot plate, but solidify at room temperature.

Ag wires were attached to these 5 electrodes with Ag epoxy. Figure 3-13 shows the setup for the Hall measurement. Samples were soldered onto a "Hall Puck" (i.e. the sample stage) which possessed 10 leads. The puck was loaded into the temperature-controlled vacuum chamber and sealed to an atmosphere of ~ 5 mTorr. The temperature was maintained at 300.00 K and a current of 5000 mA AC source was used throughout the measurement. The rationale was to minimize stray thermoelectric voltages from temperature gradients. Samples were measured twice, starting from a magnetic field of 80000 Oe to -80000 Oe and then from -80000 Oe back to 80000 Oe at a rate of 100 Oe/s. Hall resistances (R_{XY}) were measured every 10000 Oe. The relative magnetic permeability of the samples was assumed to be unity. Sienko et al. and Kupka et al. have shown that the magnetic susceptibilities for sodium, potassium, and rubidium tungsten bronzes are on the order of magnitude of 10^{-6}, which implies a relative permeability close to unity [11, 12]. It can be shown that for a relative permeability of unity, the induced magnetic field B, can be equated to the auxiliary magnetic field H if the units of gauss (10^{-4} tesla) and oersted are used, respectively[13].

The carrier concentration n, was calculated from the slope of the Hall resistance and the applied magnetic field:

[1] More resistive samples showed noisy Hall measurements. There was evidence of non-Ohmic contacts using Ti electrodes on less conductive samples as observed on an oscilloscope relative to that of the samples reduced at 10^{-16} atm pO_2. Ga-In electrodes were favored over Ti-Pt sputtered electrodes since Hall measurements were undertaken at room temperature. They also had the added convenience of shorter implementation times and the ability to be easily replaced should the electrodes fall off or wear away.

$$R_{XY} = B_Z \times \frac{1}{ned} \qquad \textbf{(Eq 3.12)}$$

where R_{XY} is the lateral Hall resistance that is derived from current flowing in the X-direction (I_X) and Hall voltage measured in the Y-direction (see Figure 3-13), B_Z is the applied magnetic field in the Z-direction, n is the carrier concentration, e is the elementary charge, and d is the thickness along the Z-direction.

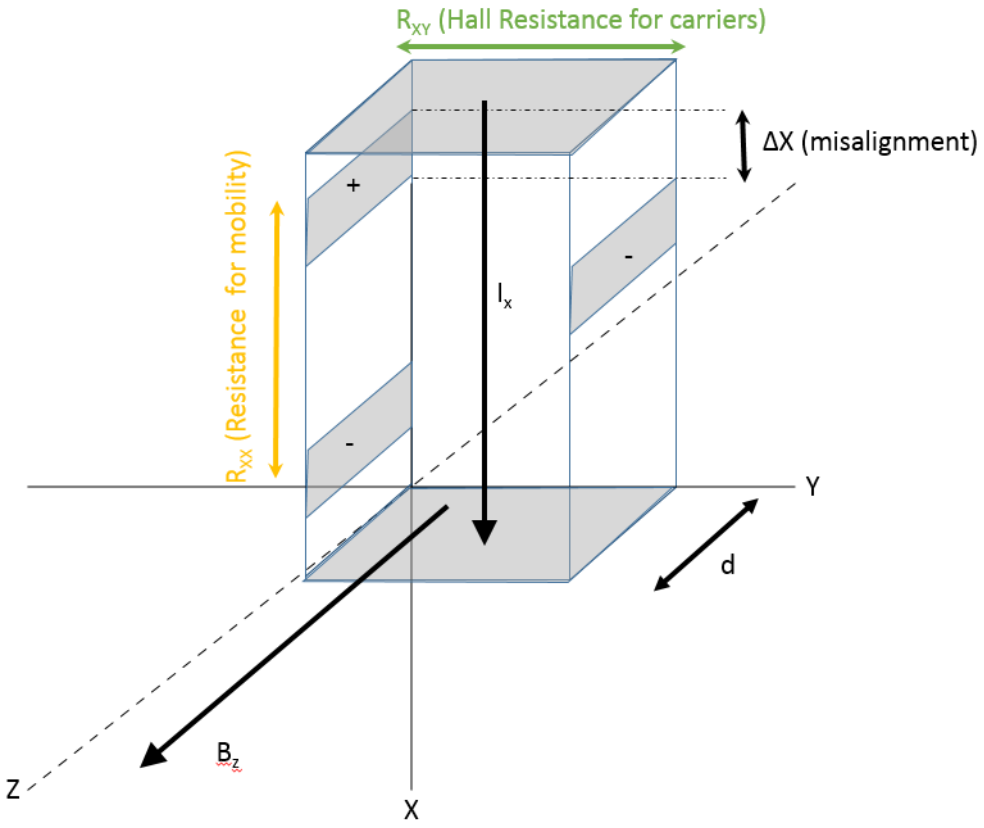

Figure 3-13. Experimental Hall geometry with respect to rectangular sample. Areas shaded in grey are electrical contacts (Pt electrode, Ag epoxy and Ag wire.)

A plot of Eq 3.12 would ideally show a straight line with slope $K = \frac{1}{ned}$. However, a spurious voltage (or resistance) contribution from R_{xx} may be present due to the misalignment or size difference of the + and – R_{XY} electrodes. The misalignment is shown in Figure 3-13 as ΔX. The misalignment voltage constitutes the largest source of spurious voltage within the measurement. However, it is not dependent on the magnetic field and so

it can be accounted for by the subtraction of the two measurements at opposite signs of the magnetic field. The correction process was done as follows:

Let $R_{YX}^{+}{}'$ and $R_{YX}^{-}{}'$ be the Hall resistance as-measured at a positive magnetic field and a negative magnetic field, respectively, and R_{YX} be the true Hall resistance. Because of the misalignment due to ΔX, there will be a contribution to $R_{YX}^{+}{}'$ and $R_{YX}^{-}{}'$ with a value of R_{XX}:

$$R_{YX}^{+}{}' = \mathrm{R_{YX}} + R_{XX} \qquad \textbf{(Eq 3.13)}$$

$$R_{YX}^{-}{}' = -\mathrm{R_{YX}} + R_{XX} \qquad \textbf{(Eq 3.14)}$$

Subtracting Eq 3.13 and 14 yields:

$$R_{YX}^{+}{}' - R_{YX}^{-}{}' = 2R_{YX} \qquad \textbf{(Eq 3.15)}$$

Dividing Eq 3.15 by two will yield the true Hall resistance.

When the true Hall resistance is plotted against the magnetic field, the resulting data points should form a straight line and have a Hall resistance of ~ 0 at ~ 0 field. The carrier concentration was then obtained by fitting the points to a line and taking the slope using Eq 3.12.

3.11 References

[1] H.-Y. Lee and R. Freer, "The Mechanism of Abnormal Grain Growth in $Sr_{0.6}Ba_{0.4}Nb_2O_6$ Ceramics," *J. Appl. Phys.*, **81** [1997] 376–382 (1997).

[2] J.A. Bock, S. Trolier-McKinstry, G.D. Mahan, and C.A. Randall, "Polarization-based Perturbations to Thermopower and Electronic Conductivity in Highly Conductive Tungsten Bronze Structured (Sr,Ba)Nb_2O_6: Relaxors vs Normal Ferroelectrics," *Phys. Rev. B*, **90** [11] 115106–1 – 115106–8 (2014).

[3] C. Duran, S. Trolier-Mckinstry, and G.L. Messing, "Fabrication and Electrical Properties of Textured $Sr_{0.53}$,$Ba_{0.47}Nb_2O_6$ Ceramics by Templated Grain Growth," **13** 2203–2213 (2000).

[4] S. Lee, R.H.T. Wilke, S. Trolier-McKinstry, S. Zhang, and C.A. Randall, "$Sr_xBa_{1-x}Nb_2O_{6-\delta}$ Ferroelectric-thermoelectrics: Crystal Anisotropy, Conduction Mechanism, and Power Factor," *Appl. Phys. Lett.*, **96** [3] 031910–1 – 031910–3 (2010).

[5] L.B. Kong, W. Zhu, and O.K. Tan, "Preparation and Characterization of PZT from High-energy Ball Milling Powders," *Mater. Lett.*, [February] 232–239 (2000).

[6] D.J. Fatemi, V.G. Harris, V.M. Browning, and J.P. Kirkland, "Processing and Cation Redistribution of MnZn-ferrites via High-energy Ball-milling," *7th Jt. MMM-Intermag Conf. Abstr. (Cat. No.98CH36275)*, **6867** [1998] 1–4 (1998).

[7] D.R. Gaskell, *Introduction to the Thermodynamics of Materials, Fifth Edition*. CRC Press, New York, NY, 2008.

[8] P. Tayebati, D. Trivedi, and M. Tabat, "Pulsed Laser Deposition of SBN:75 Thin Films with Electro-optic Coefficient of 844 pm/V," *Appl. Phys. Lett.*, **69** [8] 1023–1025 (1996).

[9] M.N. Rahaman, *Ceramic Processing*. Wiley Online Library, Boca Raton, FL, 2006.

[10] *Standard Test Methods for Density of Compacted or Sintered Powder Metallurgy (PM) Products Using Archimedes' Principle*. 2013.

[11] F. Kupka and M.J. Sienko, "The Magnetic Susceptibility of Tungsten Bronzes," *J. Chem. Phys.*, **18** [9] 1296–1297 (1950).

[12] M.J. Sienko and S. Macenness Morehouse, "Electrical and Magnetic Properties of Potassium Tungsten Bronze and Rubidium Tungsten Bronze," *Inorg. Chem.*, **2** [3] 485–489 (1963).

[13] W.D. Callister and D.G. Rethwisch, *Materials Science and Engineering: An Introduction*, 8th ed. John Wiley & Sons, Hoboken, NJ, 2009.

Chapter 4

Results and Discussion

4.1 Synthesis of the Filled Barium Niobate End Member Ceramic as a Model System

4.1.1 Introduction: Barium Niobate (BNO)

Significant progress in the refinement of the tungsten bronze structure occurred in the 1950s with the lead niobates[1–4]. The first instances of investigating the occupancy, site-filling, and distortions of non-alkali bronzes led to important correlations to electrical and dielectric properties of these structures. One of these non-alkali compositions was SBN, noted as a composition that crystallized in the unfilled state. Few references are available regarding the filled SBNs. However, there are at least three reported cases for the synthesis of the filled tetragonal tungsten bronze barium end member, BNO. Single crystal synthesis was reported by Sunshine et al., which formed as a side product during the synthesis of a rhombohedral $Ba_2Nb_{15}O_{32}$ phase as discussed in Chapter 1[1]. Synthesis of BNO ceramics have been reported by D'yachenko et al. and Hwang et al., in which vacuum-sealed ampoules with oxygen-getters and holding times of 48-100 hours were used[2, 3].

To enable systematic studies of the solid solution, a processing route was developed using the barium end member as a model system. The first goal was to demonstrate that phase pure BNO ceramics can be fabricated using a conventional solid-state processing method in lieu of vacuum ampoules. The second goal was to extrapolate the method to synthesizing other compositions of A-site filled SBNs.

4.1.2 Conditions for Conventional Solid State Sintering of BNO

The processing method outlined in Chapter 3 was the finalized process which yielded dense and phase-pure filled BNO. Unlike other tungsten bronzes such as the

unfilled SBNs, it was found that phase-pure BNO cannot be formed in air, but required an oxygen-deficient atmosphere. The phase-purity was checked by XRD and SEM for BNO ceramics fabricated under 2.5 % H_2 (12.5 cm^3/second) and N_2 (487.5 cm^3/second) as a carrier gas at 1300°C.

N_2 gas was used as the carrier gas prior to switching to Ar as discussed in the experimental procedure chapter. Calcining or sintering without the reducing atmosphere (e.g. in air) at 1300°C produced a mixture of oxides with the hexagonal $Ba_5Nb_4O_{15}$ as the primary phase. Figure 4-1 shows a partial pressure-temperature diagram for the formation of the filled tungsten bronze, BNO, from mixed oxides. The region of stability is consistent with the conditions for the onset of the anomalous increase of electrical conductivity found in the unfilled SBNs reported by Lee et al. and Bock et al.[4, 5]. The necessity of the reducing atmosphere for the formation of BNO is the first piece of evidence for A-site filling occurring within SBN filled-bronzes.

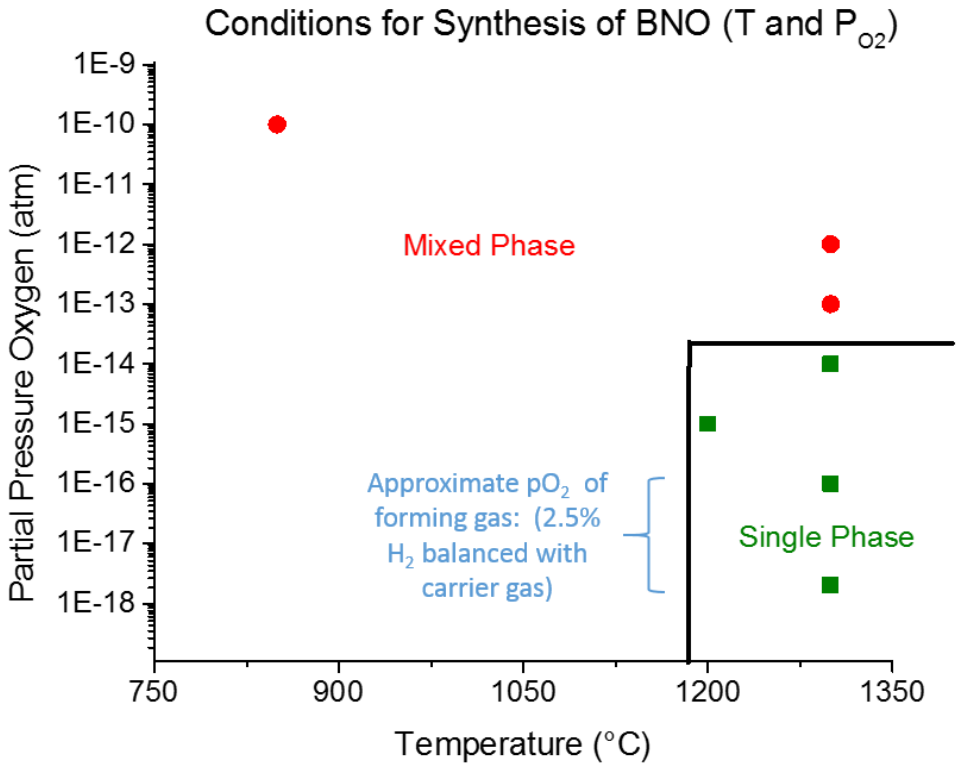

Figure 4-1. Diagram for synthesis conditions of filled BNO from raw powders. The filled tungsten bronze phase forms at elevated temperatures and require an oxygen partial pressure below10^{-14} atm. The region denoted in blue corresponds to the 2-2.5% H_2 discussed in the experimental procedure chapter.

Roller milling was used to break down the reacted aggregates into BNO powder. However, the sintering of these powders produced ceramics of inconsistent densities ranging from 80% to 97% that of the theoretical value. The Reynold's and Hough's rule for composites can be used to determine the electrical conductivity of a two phase composite and is given below:

$$\frac{\sigma_{composite} - \sigma_{matrix}}{\sigma_{composite} + 2\sigma_{matrix}} = \chi_{pore} \frac{\sigma_{pore} - \sigma_{matrix}}{\sigma_{pore} + 2\sigma_{matrix}} \qquad \textbf{(Eq 4.1)}$$

where σ is the conductivity of the phase denoted by the subscript and χ_{pore} is the volume fraction of the porosity[6]. Using Eq 4.1, a relative density of 95% would show a 7.3% decrease in conductivity and a density of 85% would show a 20.1% decrease relative to a fully dense sample. Therefore, a consistent density of 95% or greater is crucial.

Particle size is an important factor in achieving high densities in ceramics. The particle size distribution for BNO processed under two different milling methods is shown in Figure 4-3. Roller milling produced a significant concentration of particles larger than one micron, which result in poor sintering. Vibratory milling, as detailed in the experimental procedure, was necessary for the sintering of dense BNO ceramics. Vibratory milling yielded a larger fraction of smaller particles with a more consistent distribution. One disadvantage of vibratory milling is the higher concentration of contaminants due to media (in this case, ZrO_2). A sintering time of 2 hours, at 1300°C was adequate in yielding densities 95% or greater in BNO.

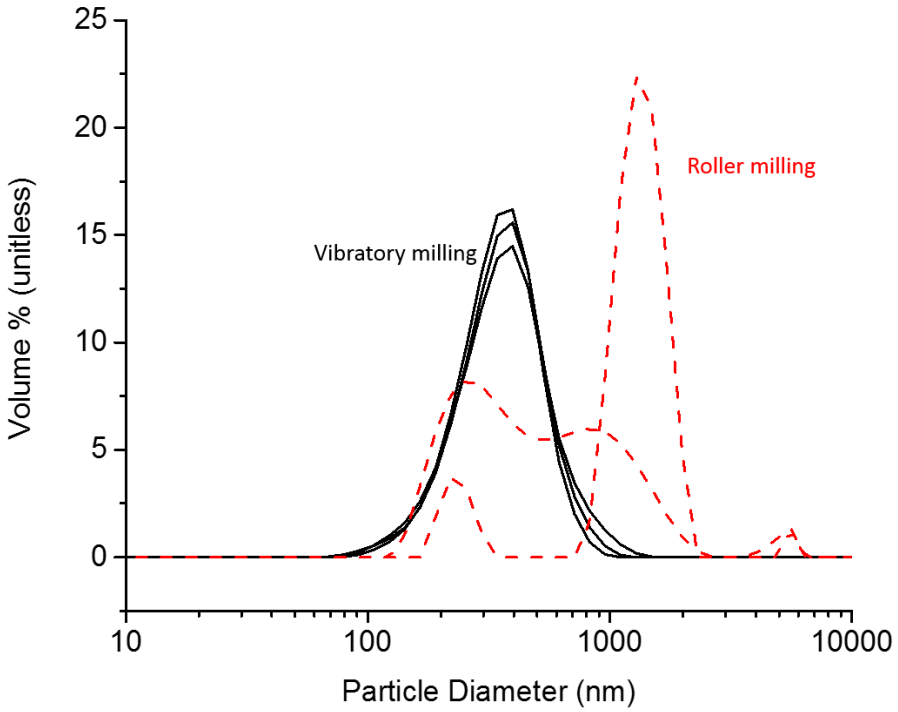

Figure 4-3. Comparison of particle size of BNO powder between roller milling and vibratory milling.

The second calcination (in which the powders are reacted to form BNO in a reducing atmosphere) yielded a small amount of a secondary phase; phase purity was shown after sintering. Figure 4-4 compares the pattern of the second calcination of the powder and the pattern after sintering. The secondary phase only shows one small, identifiable diffraction peak. The general resolution limit for phase detection using laboratory X-rays in Bragg-Brentano geometry is about 5-10 vol%[7, 8]. To confirm the identity of the secondary phase, a reaction was performed on the powders for less than 10 hours. The secondary phase is believed to be the hexagonal phase, $Ba_5Nb_4O_{15}$, since this phase was the last major phase that was identified before BNO became the primary phase. This phase was also present during the air calcination at 850°C during the carbon out-gassing step. The reason for the presence of the secondary phase in BNO is not completely clear, but it is likely due to kinetics being limited by cation motion.

Though the diffusion coefficients of SBN have not been reported, the general magnitude of the diffusion coefficient of cations in oxides (such as MgO or Al_2O_3) at

1300°C is on the order of 10^{-11} to $10^{-12}\,\frac{cm^2}{s}$ [9]. Using $x = \sqrt{Dt}$, with x being the diffusion distance, D, the diffusion coefficient, and t, the time, setting t to 10 hours, the diffusion distance is calculated to be around 6 to 2 µm. This is larger than the particle sizes measured in the powder. However, during this step, the powder is not compacted and individual particles may only be loosely in contact with each other, which increases the diffusion distance. The reason behind doing the second calcination in the powder state rather than as a pressed pellet was because it was hypothesized that exposure to the reducing atmosphere was the most important criteria in forming the BNO phase; a powder would provide larger surface areas. One reason to form a phase-pure powder before sintering was to eliminate the variation caused by kinetics.

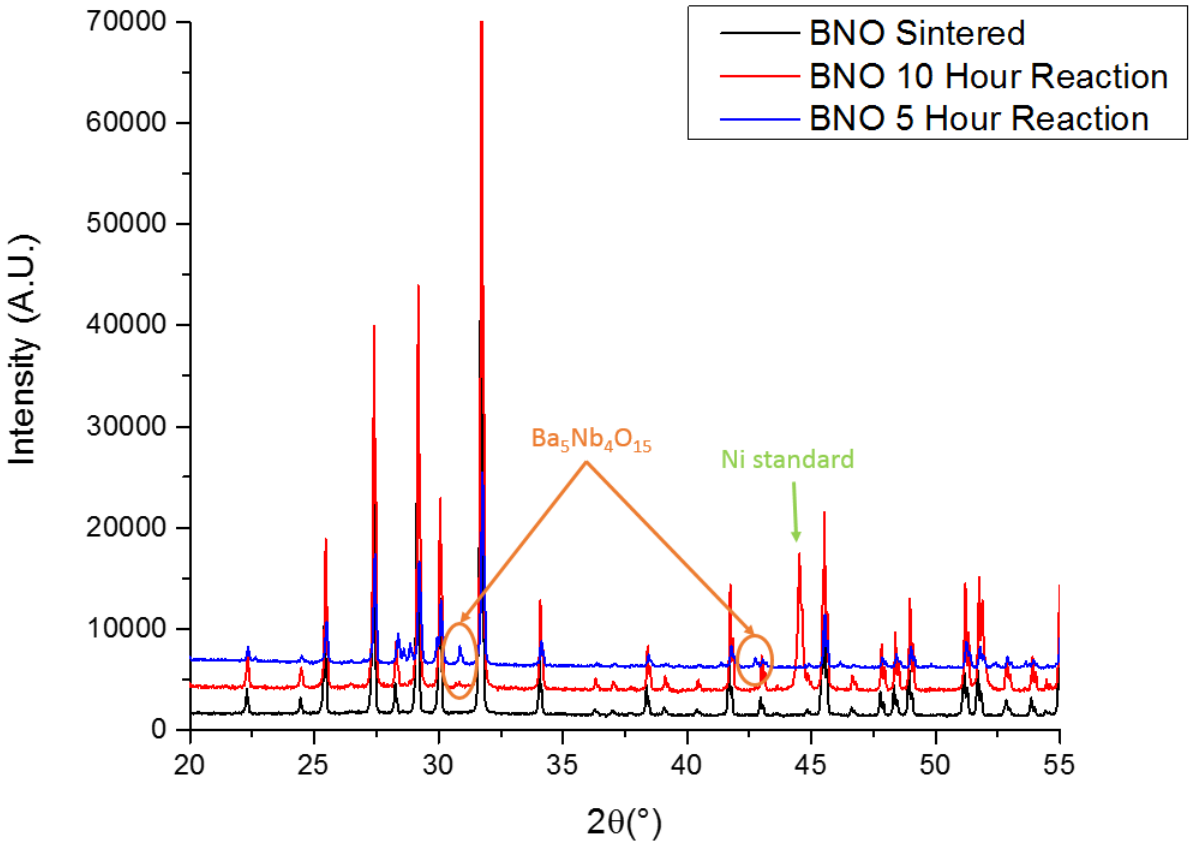

Figure 4-4. XRD pattern for BNO before and after sintering, showing that $Ba_5Nb_4O_{15}$ is the primary phase before transformation into tungsten bronze BNO. This secondary phase was also found during the air calcination at 850°C.

4.1.3 Investigations into the Cause for A-site Filling

It is evident from Figure 4-1 that the synthesis of BNO as a filled bronze requires a reducing atmosphere. However, it is not clear as to what is responsible for making the filled bronze phase stable. Given the importance of a reducing atmosphere, it is likely that oxygen defects play a role. One hypothesis for the stabilization of the filled bronze was that if oxygen vacancies were the primary defect species, then the overall swelling of the lattice due to the effective positive-positive charge repulsion of these vacancies would enlarge the volume of A-sites enough for Ba occupancy. Another hypothesis was that the removal of nearest-neighbor oxygens constituting the perimeter of the A-site could provide the necessary volume. Using the crystallographic information of BNO given by Hessen et al.,[1] and given the fact that the diameter of the A1 site is composed of antiparallel Ba-O bonds, the volume of the cage could be estimated by measuring the shortest bond lengths within the A1-site using Crystal Maker®. This is shown in Figure 4-5.

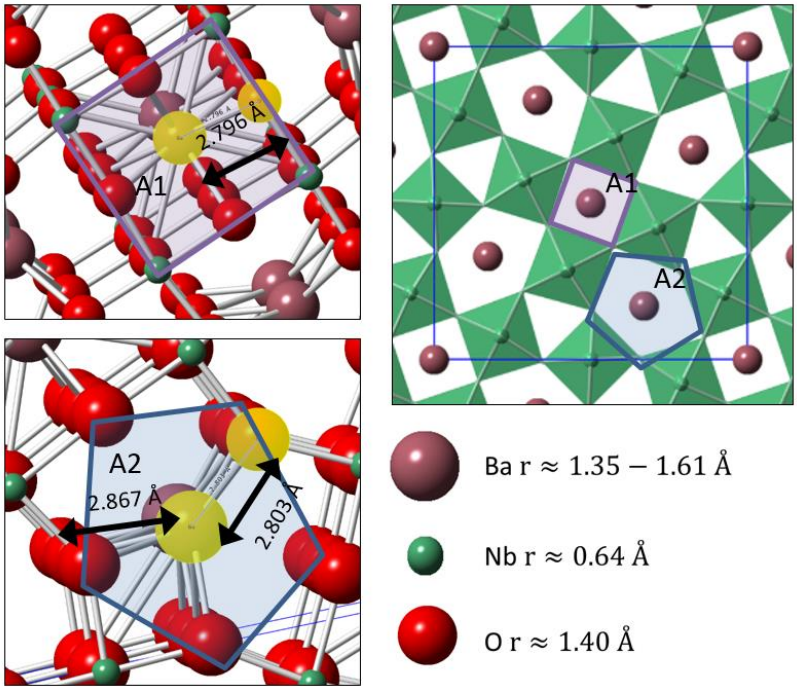

Figure 4-5. Nearest neighbor bond lengths of the A1 site and A2 site of BNO using crystallographic data reported by Hessen et al.[1]. Note that the smallest Ba-O bonds do not fall within the same plane and that the Ba radius depends on coordination number (ranging from 1.35Å for 6 coordination to 1.61Å for 12 coordination, respectively)

The A2 site was not considered in this evaluation because the Rietveld refinements by Trubelja et al. and Leffler et al. in the unfilled SBNs showed that Ba had a strong preference for the A2 site[11, 12]. It is thus presumed that the size of the A1 site is the limiting factor since the A2 site has been reported to be large enough to accommodate Ba.

For both cases, an effective available radius for the Ba ion was calculated by measuring the shortest Ba-O bond and then subtracting the oxygen radius. The concept is shown in Figure 4-6. This effective radius for the Ba was used to estimate the effective volume of the A1 site.

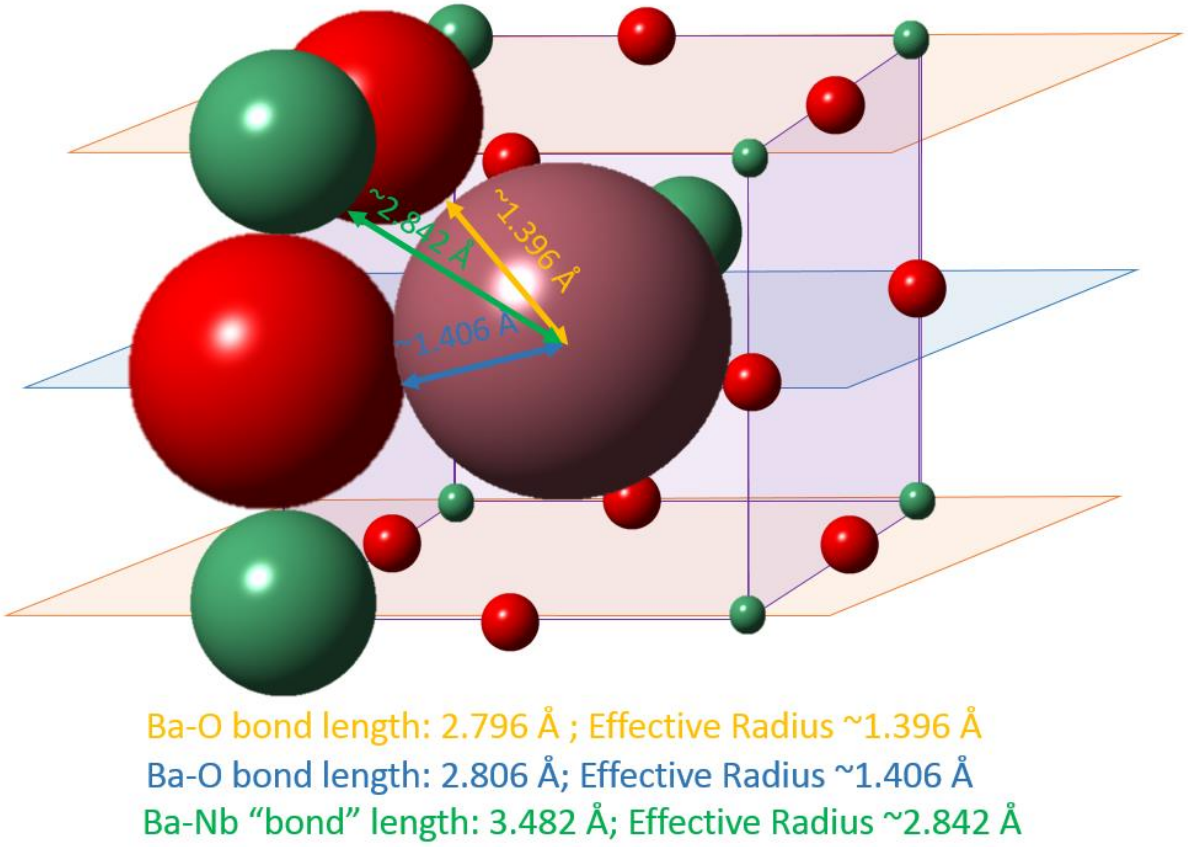

Figure 4-6. Concept of the effective Ba radius. The A1 site has two distinct Ba-O bond lengths. Other Nb and O atoms are down-scaled to better show the 12 coordination of the Ba at the A1 site.

To test the first hypothesis, BNO powder was annealed under 4 reducing conditions for 10 hours at 1300°C and XRD was used to refine the lattice parameters via Rietveld refinement. Crystal Maker® was then used to determine the size of the A1 site according to the lattice parameters. The results are shown in Table 4.1.

Table 4.1 Lattice Parameter-A1 Site Effective Ba Radius vs. pO_2

pO_2 (atm)	a = b (Å)	error (+/-)	c (Å)	error (+/-)	Refinement R-factor (%)	A1 site shortest Ba-O bond length (Å)	A1 site effective Ba radius (Å)
10^{-12}	12.5934	0.0005	3.9806	0.0002	4.94	2.7970	1.397
10^{-13}	12.6044	0.0002	3.9789	0.0001	4.60	2.7970	1.397
10^{-14}	12.6081	0.0003	3.9794	0.0001	5.10	2.7980	1.398
10^{-16}	12.6152	0.0003	3.9827	0.0001	5.50	2.8000	1.400
* not phase pure							
$Ba_6Ti_2Nb_8O_{30}$ (ceramic)	12.54		4.01		-	2.80	1.40

It can be seen that the lattice parameters increase with harsher reduction conditions, which is assumed to be a reflection of the swelling of the lattice due to oxygen vacancies. An anneal under 10^{-16} atm pO_2 and one under 10^{-12} atm (in which the powder is no longer single-phase), showed less than a 0.1 Å change in the *a* lattice parameter; the small changes are also observed in *c*. In these powder samples, the average lattice parameters were larger than those reported in the single crystal by Hessen et al.[1]. This is true even at higher pO_2 values in which the powder is no longer single-phase BNO. The effective Ba radius, as calculated in the right most column of Table 4.1, showed that the effective volume is too small to accommodate the Ba radius, unless the Ba coordination drops to ~ 7. If the oxygen vacancies are distributed homogeneously in the material, then it is unlikely that 5 oxygen vacancies can be clustered around a single A1 site.

Furthermore, Zheng et al. has reported another filled tungsten bronze with Ba occupying the A-sites [10]. This compound, $Ba_6Ti_2Nb_8O_{30}$ was an insulating material and had lattice parameters of 12.54 Å and 4.01 Å for *a* and *c*, respectively as shown at the bottom of Table 4.1[10]. Accordingly, the effective Ba radius is 1.40Å. The change in the effective Ba radius is small; only on the order of 0.01 Å relative to the highly reduced BNO samples in this work. An appropriate effective radius for Ba of 10-12 coordination for the A1 site would require *a* and *c* to change on the order of 1.0 Å.

To test the second hypothesis, direct removal of O atoms from the A1-site was used to assess the next shortest Ba bond length and, as previous, the O radius was subtracted to obtain an effective Ba radius. In this evaluation, the Ba coordination (and corresponding Shannon-Prewitt radius) is taken to be 10-12 since more than 2 oxygen vacancies around one site seems to be unrealistic. The results are shown in Table 4.2.

Table 4.2 Simulation of A-site Volumes as a Result of Oxygen Vacancies

Reference:	a = b (Å)	c (Å)	A1 site effective Ba radius (Å): No Oxygen Vacancies	A1 site effective Ba radius (Å): 1 Oxygen Vacancy	A1 site effective Ba radius (Å): 2 Oxygen Vacancies (Ba-Nb neighbor)
BNO Single Crystal	12.5980	3.9774	1.396	1.407	2.842

Figure 4-6 shows that shows that with no oxygen vacancies, the nearest neighbor of the A1 site is too small to accommodate the radius of Ba (orange line). Assuming the removal of this oxygen provides a minute amount of additional space, a subtle shift of the Ba in the direction of this additional space may be possible. If so, the next nearest neighbor will be the O that corresponds to the longer Ba-O bond length (blue line in Figure 4-6.) This would yield an effective radius of 1.407 Å. This is still too small for Ba of 10-12 coordination. However, if in the vicinity, this same O is also removed, the cage should now be open such that the Ba could potentially move towards the direction of a Nb neighbor

(green line in Figure 4-6.) With a Ba-Nb bond distance of 3.482 Å, the effective radius becomes 2.842 Å as shown in Table 4.2. Thus two vacancies clustered at the A1 may allow for Ba occupancy.

The conclusion that can be drawn here is that physical removal of oxygen enlarges the A1 site more than the lattice swelling. However, the role of charge compensation cannot be ignored because the $Ba_6Ti_2Nb_8O_{30}$ reported by Zheng et al. can be synthesized without oxygen vacancies. The cations and anions are balanced in $Ba_6Ti_2Nb_8O_{30,}$ if Ti is 4^+ and Nb is 5^+. However, for BNO, two of the Nb atoms would have to have a 4^+ oxidation to account for 6 Ba atoms, even if oxygen vacancies are not considered. The presence of Nb^{4+} in sufficiently-reduced unfilled SBN has been reported by Lee et al. and Dandeneau et al. via electron energy loss spectroscopy and in X-ray photoelectron spectroscopy, respectively[4, 13]. The role of the transition metal oxidation state would require further study.

4.1.4 Microstructure

Backscatter imaging (BSE) by SEM was utilized as an additional check for phase purity by searching for phase contrasts. The result is shown in Figure 4-7.

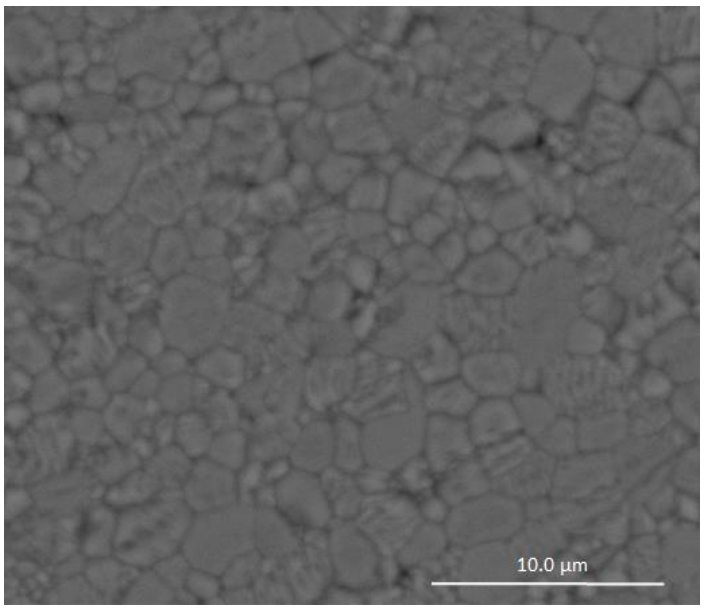

Figure 4-7 BSE SEM of a BNO sample sintered at 1300°C with a sintering time of 2 hours using N_2 as a carrier gas. Sample was thermally etched for 30 mins at 1200°C.

The image in Figure 4-7 shows that no obvious phase contrast is seen in the sample. Elemental analysis conducted by EDS (the detector use is capable of detecting ~0.05 wt%) shows that only Ba, Nb, and O was detectable, suggesting very little or no Zr or Al contamination from processing had been incurred. The microstructure revealed a bimodal grain size distribution in which large grains were surrounded by what appeared to be pockets of smaller grains.

Field emission scanning electron microscope (FESEM) images were taken for a similar BNO sample sintered for 5 hours at 1350°C using Ar as the carrier gas. This is shown in Figure 4-8.

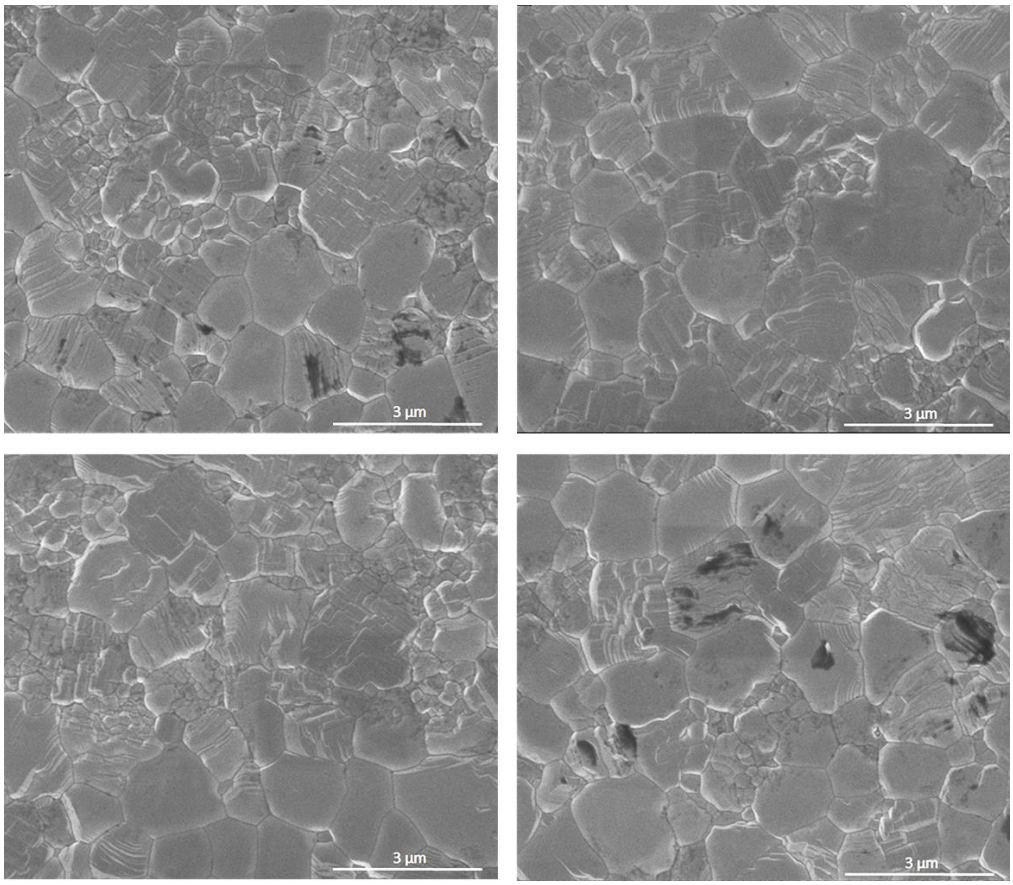

Figure 4-8. Secondary Electron FESEM images of BNO sintered under Ar and H_2 at 1350°C for 5 hours.

The higher resolution micrographs in Figure 4-8 confirmed the presence of pockets of smaller grains The average grain size in the BNO samples were calculated using the

line-intercept method developed by Mendelson[14]. In this method, lines are arbitrarily drawn onto the micrograph and the number of grain boundaries is counted. The average grain size is then:

$$\overline{D} = 1.56 \times \frac{L_T}{G_B} \quad \textbf{(Eq 4.2)}$$

where $\overline{D}$ is the average grain size in μm, L_T is the total length of lines in μm, $G_B$is the total number of grain boundaries crossed, and the factor, 1.56, is a geometrical correction for the assumption of tetrakaidecahedron-shaped grains[15]. Ten lines were drawn on the micrographs of BNO shown in Figure 4-8.

The calculated average grain size was 1.2 μm. Dark areas were likely undissolved Crystal Bond® glue that subsequently graphitized in the reducing atmosphere during the thermal etch. This was not expected to affect properties. A similar microstructure is expected for the other compositions of the filled SBNs. The high density of grain boundaries is not expected to affect electrical conductivities significantly in low-mobility hopping conductors since the nearest neighbor hopping distance is expected to be much smaller as discussed in Chapter 2[16].

4.1.5 Electrical Conductivity

The electrical conductivity is of interest in the present work because it is the variable that is primarily responsible for the high power factors reported by Lee et al. in SBN[4]. Electrical conductivities as a function of temperature were measured as outlined in the previous chapter. Figure 4-9 shows the results between two BNO samples that were sintered under two different conditions.

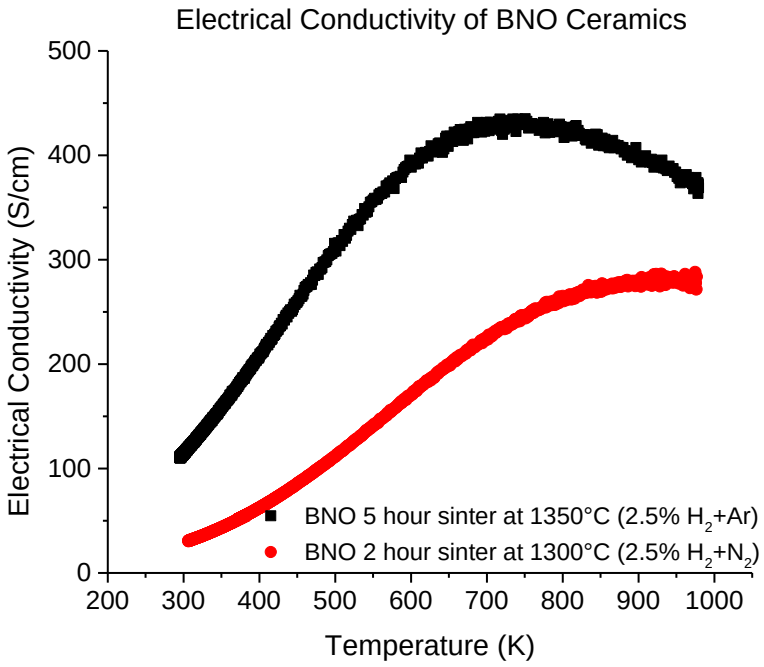

Figure 4-9. Electrical conductivity vs. temperature of BNO ceramics fabricated under two different sintering conditions.

Because nitrogen is relatively inert and the samples were phase pure, there was little reason to believe that the carrier gas had significant effect on the electrical conductivity. Thus, it is possible that the degree of reduction is responsible for the differences in the electrical conductivities. Both kinetics and thermodynamics are likely involved. Because the source powder was fabricated under 1300°C, it is not surprising that a ceramic sintered at a higher temperature would exhibit higher electrical conductivities than one sintered at 1300°C, since a higher defect concentration is expected at higher temperatures from an Arrhenius relation. Figure 4-9 also implies that oxygen activity continues to affect the electrical conductivity by almost a factor of two despite having reached the filled-bronze state. It is noted that the more reduced sample shows a maximum conductivity before subsequently decreasing. This behavior is also observed in the SBN samples reported by Lee et al. and Bock et al. as discussed in the literature review[5, 17].

The electrical conductivity in the BNO single crystal reported by Hessen et al. along the a-axis and c-axis at 300 K are 800 S/cm and 64000 S/cm, respectively[1]. The

conductivity parallel to the c-axis is one magnitude less than a typical metal such as Fe[18]. While several models for calculating the conductivity of a polycrystalline material based on its single crystal properties exist, the Reuss and Vought models are the most common and least restrictive.[19–22].

The Reuss model represents the upper bound properties of a polycrystalline sample. Likewise, the Voigt model represents the lower bound. Table 4.3 shows the predicted polycrystal conductivity at 300 K based on the values of the single crystal reported by Hessen et al.[1].

Table 4.3 Ceramic BNO Electrical Conductivity Predicted from Single Crystal

Model	Equation		Predicted Polycrystal Conductivity (S/cm) For BNO
Reuss (max upper bound)	$\sigma_{PC} = \frac{1}{3}(2\sigma_a + \sigma_c)$	Eq. 4.3	**22000**
Voigt (min lower bound)	$\frac{1}{\sigma_{PC}} = \frac{1}{3}\left(2\frac{1}{\sigma_a} + \frac{1}{\sigma_c}\right)$	Eq. 4.4	**12000**

	Temperature (K)	Conductivity (S/cm)
BNO Ceramic (this work) 2 hour sinter at 1300°C ~10^{-16} atm P_{O2} (Nitrogen)	**300**	**25**
	950 (max σ)	**275**
BNO Ceramic (this work) 5 hrs 1350 C ~10^{-16} atm P_{O2} (Argon) (*pellet sintered at half the thickness of the above sample)	**300**	**110**
	750 (max σ)	**440**

While it is generally not realistic for a polycrystal to approach the upper bound of a single crystal counterpart, it can be seen that the single crystal has two to three orders of magnitude greater electrical conductivity than the ceramics presented in this work at 300

K. Furthermore, the measured conductivities lie well below the lower limit established by the Voigt model, by about two orders of magnitude.

When comparing the electrical conductivities of the unfilled SBN ceramics and the SBN single crystal studied by Lee et al. and Bock et al., the data fall within the Reuss and Voigt bounds. This is shown in Table 4.4.

Table 4.4 Reduced, Unfilled SBN Ceramic Electrical Conductivity Predicted from Single Crystal

Model	Equation	Predicted Polycrystal Conductivity (S/cm) For Unfilled SBN 60-40
Reuss (max upper bound)	$\sigma_{PC} = \frac{1}{3}(2\sigma_a + \sigma_c)$	**363**
Voigt (min lower bound)	$\frac{1}{\sigma_{PC}} = \frac{1}{3}\left(2\frac{1}{\sigma_a} + \frac{1}{\sigma_c}\right)$	**101**

	Temperature (K)	Conductivity (S/cm)
Unfilled SBN 60-40 Single Crystal 1300°C ~10^{-14} atm P_{O2}	**550 (max σ)**	**a-axis 70**
	550 (max σ)	**c-axis 950**
Unfilled SBN 60-40 Ceramic~10^{-14} atm P_{O2}	**600 (max σ)**	**160**

The conductivity along the c and a-axes are ~ 950 S/cm and 70 S/cm, respectively, in the reduced 60-40 SBN single crystals and the Reuss and Voigt bounds predict 400 and 100 S/cm in the 60-40 polycrystalline samples, respectively [17].

The reason for the large discrepancy in the electrical conductivities between the ceramic and the single crystal of BNO is currently unknown. An error of over 80% in the single crystal data is required for the conductivities measured in this work to fall within the Reuss and Voight bounds. Even though processing method outlined in this work is

expected to be more reducing than the vacuum ampoules used by Hessen et al., it is possible there is a significant contribution to the resistivity due to grain boundaries. One further consideration is that the single crystal of BNO was a result of a by-product, and since further characterization had not been reported, it is unknown what impurities or nonstoichiometries were present[1].

In regards to the polycrystal models evaluated by Schulgasser, the maximum degree of anisotropy studied was low ($\eta = 2.5$) relative to that of SBN and BNO, where $\eta \approx 10$ and 55, respectively. Schulgasser comments that axially symmetric crystals with degrees of anisotropy greater than 2.5 are uncommon[19]. At $\eta < 2.5$, the Hashin-Shtrikman and Molneux models, which feature narrower bounds for more specific structures, deviate rapidly from the lower bound established by the Reuss model[19]. An evaluation of the Voigt and Reuss models in crystals of high η could be useful in explaining the large discrepancy in conductivity between the BNO ceramics here and the BNO single crystal reported by Hessen et al.[1].

4.2 A-site Filling in SBN

4.2.1 Fabrication of Filled Tungsten Bronze SBN Ceramics

Filled SBN compositions were synthesized using the same process used for the fabrication of BNO ceramics. Figure 4-10 shows the powder XRD results for the SBN compositions. It can be seen from the overlay of patterns in Figure 4-10 that compositions of 10-90, 20-80, 40-60, and 60-40 (Sr-Ba) showed no secondary phases after the calcination reaction that formed the tungsten bronze phase. However, the 80-20 composition showed a small peak that was believed to be a cubic phase of strontium niobate. However, the second highest intensity secondary peak for the $Sr_{1-x}NbO_3$ was too small to be identified. The secondary phase peak disappeared after sintering of the 80-20 filled bronze and so the consequences on electrical properties are likely minimal. The strontium end member, SNO was the only phase in which “XRD phase-purity” could not be achieved. This was consistent with recent results from Kolodiazhnyi in which

orthorhombic distortions were fitted to the pattern of SNO and yielded better refinements[23]. Reasons for the inability to achieve complete solid-solution in SNO would need further investigation. For the purposes of this study, solid solution was achieved up to the 80-20 composition. As such, further results are not reported for the SNO composition.

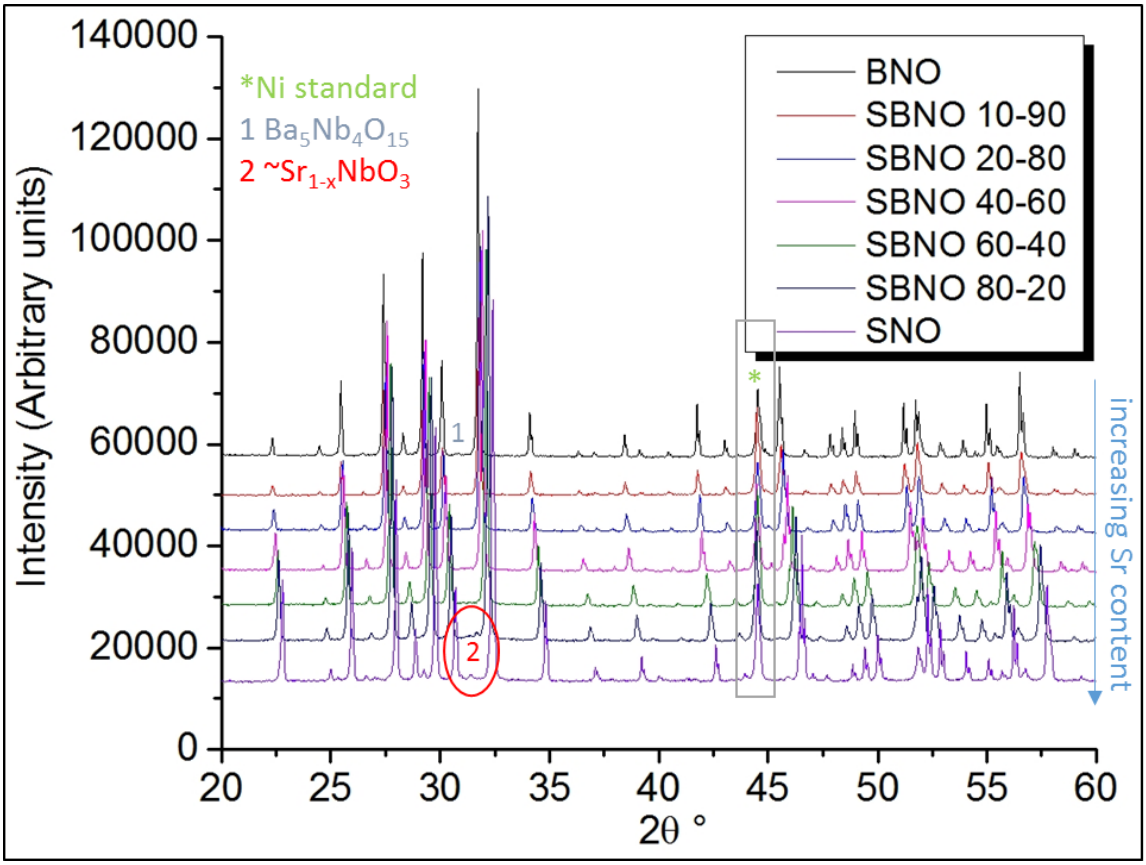

Figure 4-10. Powder XRD for compositions of SBN

The refined lattice parameter *a*, was then plotted as a function of Sr content. Doing so allowed the observation of Vegard's Law, which is generally obeyed in solid solutions. The results are shown in Figure 4-11. The decreasing lattice parameters and unit cell volume is consistent with the size of the atoms; as the larger Ba atoms are replaced with smaller Sr atoms within the solid solution, the unit cell size is expected to decrease. However, two distinct slopes are observed, meaning that there were two occurrences of Vegard's Law. The change in slope occurred between the compositions 20-80 and 40-60.

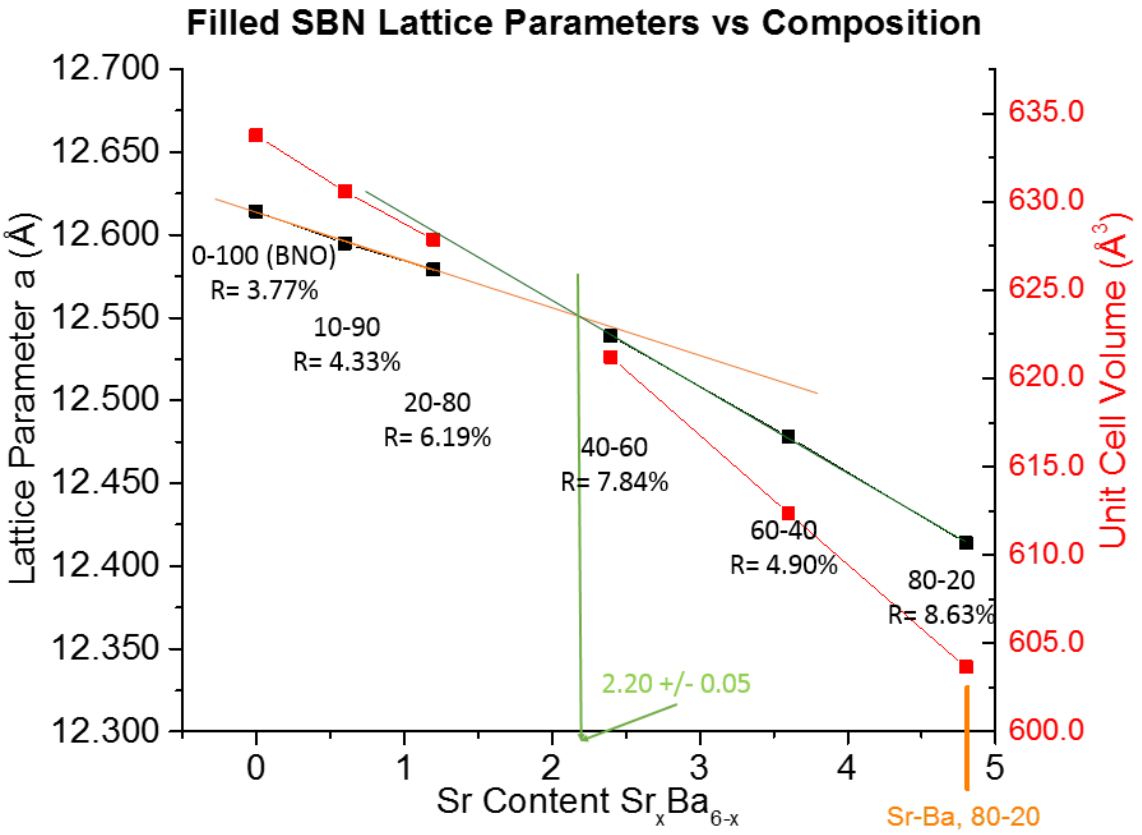

Figure 4-11. Lattice parameter and unit cell volume vs. Sr content. The green and orange lines trace the slope of the lattice parameters after doing a least-squares fit. R refers to the R-factor, an indication of "goodness of fit" of the calculated vs. experimental pattern after Rietveld refinement.

The change in slope is attributed to the preferential site occupancy of the two A-sites with increasing Sr content as was discussed in the literature review[11, 12, 24]. In the unfilled case, the occupancy of Ba in the A1 site is very low; it is either predominantly occupied by Sr or is vacant[11, 12]. Leffler showed that as the Sr content increases, there is a preferential occupancy for the A2 site. In the filled bronze case Ba is forced into the A1 site for BNO and low Sr compositions. As the Sr content increases, Sr atoms are likely to preferentially displace Ba from the A1 site since the A2 site is favored by Ba. The slope change would then occur if all of the A1 sites are occupied with Sr. If this is true, then the slope change would be expected to occur at $x = 2$, since 2 out of the 6 A sites are A1.

The two slopes intersect at about $x = 2.20$, which is slightly over the ideal value. Finding the intersection of the two slopes using the unit cell volume gives a statistically

insignificant decrease in x relative to using the a lattice parameters. In general, the tungsten bronze structure is complex and can accommodate large degrees of disorder. Leffler proposed the idea that the orientation of the octahedra can twist and minimize the volume of the A1 site[12]. In that work, it was shown that the Sr occupancy for the A1 site in an 50-50 unfilled SBN increased from 54% to 62% after annealing[12]. Since the XRD results of the present work were not from annealed samples, it is possible that some of the Sr were still occupying the A2 sites at $x = 2$.

The unit cell volume and lattice parameters continue to decrease as Sr replaced Ba atoms within the structure. In this regard, the unfilled and filled SBNs behave similarly in that both exhibit a form of preferential site occupancy. The deviation from a single instance of Vegard's Law in the filled SBNs was also found in the work of Kolodiazhnyi[24].

Initial sintering of the SBN compositions using nitrogen at 1300°C prompted the change to a higher sintering temperature and a switch to using argon as the carrier gas. This was due to the fact that NbN secondary phases were identified as the Sr content increased. This result was also seen in the work of Dandeneau et al. when reducing the unfilled SBN bronzes[13]. Sintering compositions where the Sr content was above 40-60 also showed poorer density, as is described below. Particle sizes were measured for several of the compositions as shown in Figure 4-12. The particle sizes and the distribution are very similar to that found in the BNO preparation methods.

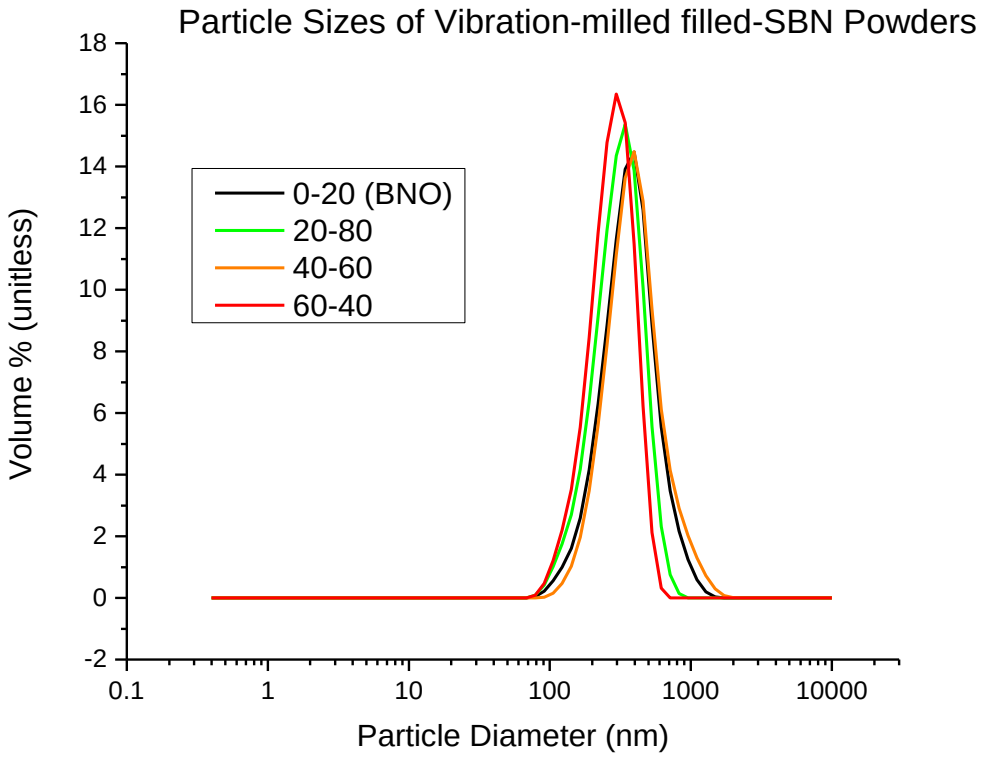

Figure 4-12. Particle size distribution for several compositions of filled SBN. BNO (black) serves as a reference.

Because similar particle size distributions were achieved in the filled SBN powders as those of the BNO, it was likely that a higher sintering temperature was required. This is a reasonable assumption as, Sr, being a smaller atom, would be more "refractory" than Ba. The Sr-O bond is expected to be stronger than the Ba-O bond, and so the melting temperature would increase, requiring a higher sintering temperature. The density improved with a 50°C increase in the sintering temperature as shown in Table 4.5. Because a 1350°C sintering temperature is expected to result in a more conductive ceramic than one sintered at 1300°C, the filled SBNs should be compared to a BNO sample sintered at 1350°C.

Table 4.5 Relative Density as a Function of Sintering Temperature and Composition

Composition (Sr-Ba)	Density sintered at 1300°C (g/cm^3)	Relative Density (1300°C)	Density sintered at 1350°C (g/cm^3)	Relative Density (1350°C)
0-100	5.73	0.98	5.60	0.96
20-80	5.59	0.97	5.50	0.96
40-60	5.43	0.96	5.45	0.96
60-40	4.71	0.85	5.27	0.95
80-20	4.13	0.75	5.10	0.93

4.2.2 Evaluation of A-site Occupancy using TEM and EDS

Compositions from BNO to 80-20 (Sr-Ba) were "phase pure" via XRD. However, as discussed in a later section, there existed cases in which inconsistent electrical conductivities were measured. A possible explanation was some degree of oxidation, either during processing or during the electrical conductivity measurement. In regards to the former, oxidation may occur during the cool down of the furnace. Similarly, reoxidation could occur during measurement of the electrical conductivity. In both cases, it is possible to oxidize the grain boundaries, which could inhibit electrical conductivity. The volume% of any secondary phase would be too small to be detected by XRD, and yet, could still remove cations from the A-sites, which would prevent the sample from being a truly filled-bronze. Of course, the same consequence is true for any possible secondary phases. Unlike BNO, in which successful syntheses had been reported, filled SBNs had not yet been adequately characterized.

Transmission electron microscopy (TEM) using STEM mode was used to investigate the grain boundaries of the 40-60 composition. This composition was investigated because there was one instance in which lower electrical conductivities than expected were measured. The cause of the low conductivity was suspected to be either NbN (when a H_2 and nitrogen atmosphere is used during processing) or possible oxidation at the grain boundaries. Because these filled bronzes require a reducing atmosphere to be phase-pure, oxidation at the grain boundaries would also imply mixed phases within the

vicinity. The data are courtesy of Dr. Hanzheng Guo of the Randall group from The Pennsylvania State University. The results are shown in Figure 4-13.

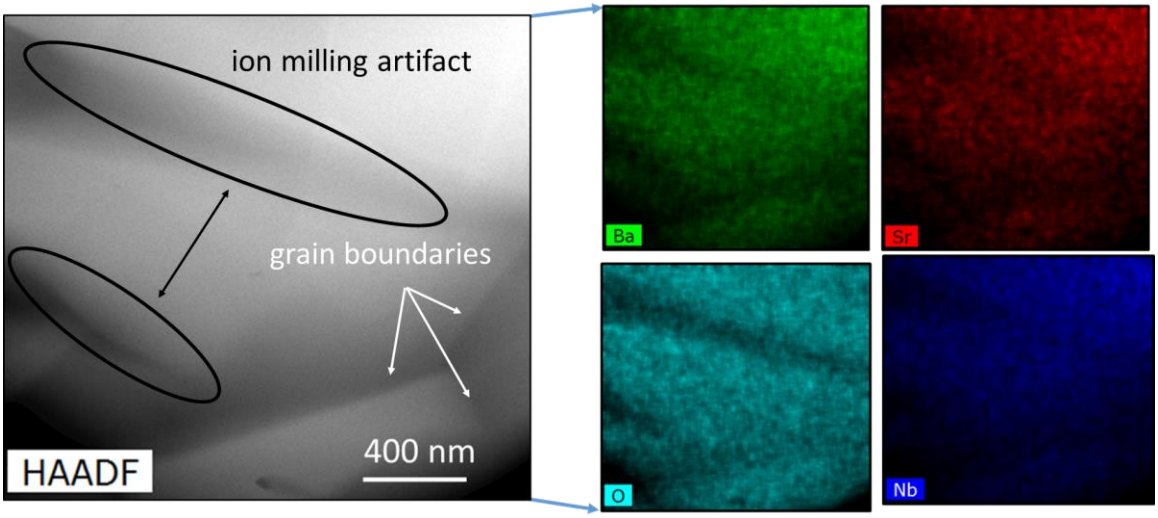

Figure 4-13. TEM micrograph and EDS elemental mapping of a 40-60 filled SBN composition after an electrical conductivity measurement.

From the TEM image in Figure 4-13, within the area observed, no evidence of secondary phases were identified in the grains. Larger area elemental maps (not shown) show Nitrogen signal. Furthermore, the elemental maps show a homogenous distribution of elements with no significant changes in the signals at the grain boundaries. To confirm the composition at the grain boundaries, several line scans at the grain boundary were averaged. This is shown in Figure 4-14. There is no statistically significant change in composition detectable at the grain boundaries. In particular, there are no relative changes in the Sr and Nb signals relative to the Nb signal that would be consistent with a change in the degree of filling at the grain boundaries.

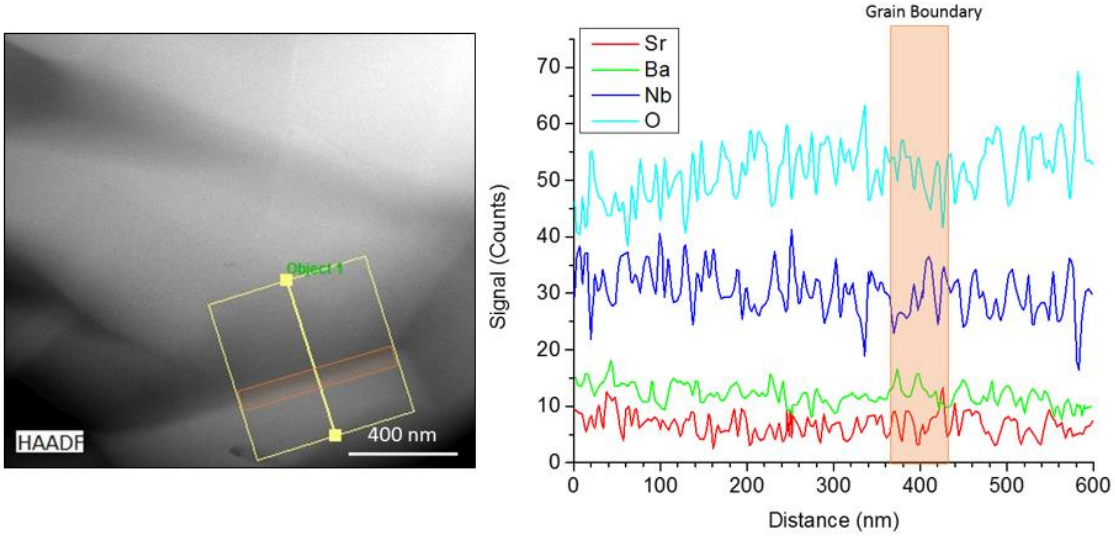

Figure 4-14. Line scan at grain boundary of filled 40-60 SBN.

Quantitative EDS using the SEM was used to independently determine the validity of A-site filling on a 60-40 composition. A 61-39 unfilled SBN single crystal was used as an external standard as outlined in the experimental procedure. The composition of a filled SBN ceramic, unfilled SBN ceramic (sintered in air), and an unfilled SBN ceramic (reduced at 1300°C at 10^{-12} atm pO_2, for which NbO_{2-x} did not precipitate) of 60-40 composition was quantified[2]. Aztec® software was used to calculate the atom % of each element. This number was then used to find the number of atoms of each element relative to the chemical formula (45 atoms for the unfilled SBN, and 46 atoms for the filled SBN.) Assuming that the Nb cation was the least mobile or least likely to volatilize, each instance of the chemical formula was normalized to 10 Nb atoms. The subsequent formula was then used to quantify the site filling based on the number of Sr and Ba atoms in the normalized chemical formula. The results are shown in Table 4.6.

[2] Without reduction, the unfilled SBN would exhibit charging with the given accelerating voltages used. The charging was shown to affect the EDS signal being measured, resulting in a lower cation signal.

Table 4.6. Quantitative EDS on SBN 60-40 Ceramics

Specimen	After normalizing to Nb	Ideal	Filling of A-site after Normalizing to Nb
Filled SBN 60-40 Ceramic	$Sr_{3.82}Ba_{2.39}Nb_{10}O_{30.06}$	$Sr_{3.6}Ba_{2.4}Nb_{10}O_{30-\delta}$	6.21 +/- 0.33
Reduced Unfilled SBN 60-40 reduced (No NbO_{2-x})	$Sr_{3.56}Ba_{1.51}Nb_{10}O_{29.35}$	$Sr_3Ba_2Nb_{10}O_{30-\delta}$	5.07 +/- 0.25

The results of Table 4.6 show that the filled SBN is within error of the ideal 6-site filling. The result of 5.07 for the unfilled SBN is also within error of ideal 5-site filling. This result demonstrates that EDS can differentiate the chemistry between an unfilled SBN and a filled SBN. The 6-site filling and 5-site filling results are consistent with XRD and the TEM results above.

4.2.3 Validity of A-site Occupancy: Electrical Conductivity

The model that full occupancy of the A-site is responsible for the large increase in the electrical conductivity when fired below a given pO_2 is based on the assumption that the occupancy is compensated by electrons. From the unfilled state of SBN, the defect reaction can be expressed as follows:

$$5(Sr,Ba)_A^{\times} + V_A^{\times} + 10Nb_{Nb}^{\times} + (30-\delta)O_O^{\times} \leftrightarrow 5(Sr,Ba)_A^{\times} + (Sr,Ba)_{V_A}^{\cdot\cdot} + 2e^{-} + 10Nb_{Nb}^{\times} + (30-\delta)O_O^{\times} \quad \textbf{(Eq 4.8)}$$

Here, the 6 A-sites are denoted by the subscript, *A*, and $V_A^{\times}$ refers to the empty A-site in the unfilled SBN. Due to the large number of vacant A-sites in a bulk sample, the electronic compensation was expected to be much larger than the compensation by oxygen vacancies.

This would be consistent with the sudden and dramatic increase in the electrical conductivity from 10^{-12} atm to 10^{-14} atm pO_2 shown by Lee et al.[4].

Using the lattice parameters obtained from the X-ray diffraction results and assuming full electronic compensation of the A-site filling, the model suggests an additional$\sim 10^{21}\,\frac{carriers}{cm^3}$. This high carrier concentration is also consistent with the high electrical conductivities of the BNO single crystal reported by Hessen et al.[1]. If the model is correct, then the following hypothesis is proposed: Regardless of composition, if A-site filling is achieved with phase purity, then the filled SBNs will show similar magnitudes in electrical conductivity.

Electrical conductivities for the filled SBNs are shown in Figure 4-15. The green line here is a reference to the unfilled 60-40 ceramic as measured by Lee et al.[17]. In general, there is considerable scatter in the maxima as well as in the room temperature conductivities. Most compositions showed similar conductivities (100-250 S/cm) as those previously reported by Bock et al. and Lee et al.[5, 17]. The lower conductivity observed in the 80-20 composition may be attributed to the less-than-ideal relative density of 93% as compared to the other compositions sintered at 1350°C. However, this does not completely account for the 100 to 200 S/cm difference in its maximum conductivity from the 60-40 composition. This is in contrast to only a 50 S/cm decrease in maximum conductivity on going from the 40-60 to 60-40 composition.

A maximum conductivity was reached in all samples except for the 20-80 composition. Despite being phase pure, it is believed that the 20-80 sample was oxidized during processing. The rationale for oxidation was because several (but sparse) instances of lower conductivities in other phase-pure compositions (not shown here) were observed[3].

[3] It was discovered that over time and over-tightening of the endcap screw through which the H_2 exits, a reasonably large leakage developed which lead to oxidation.

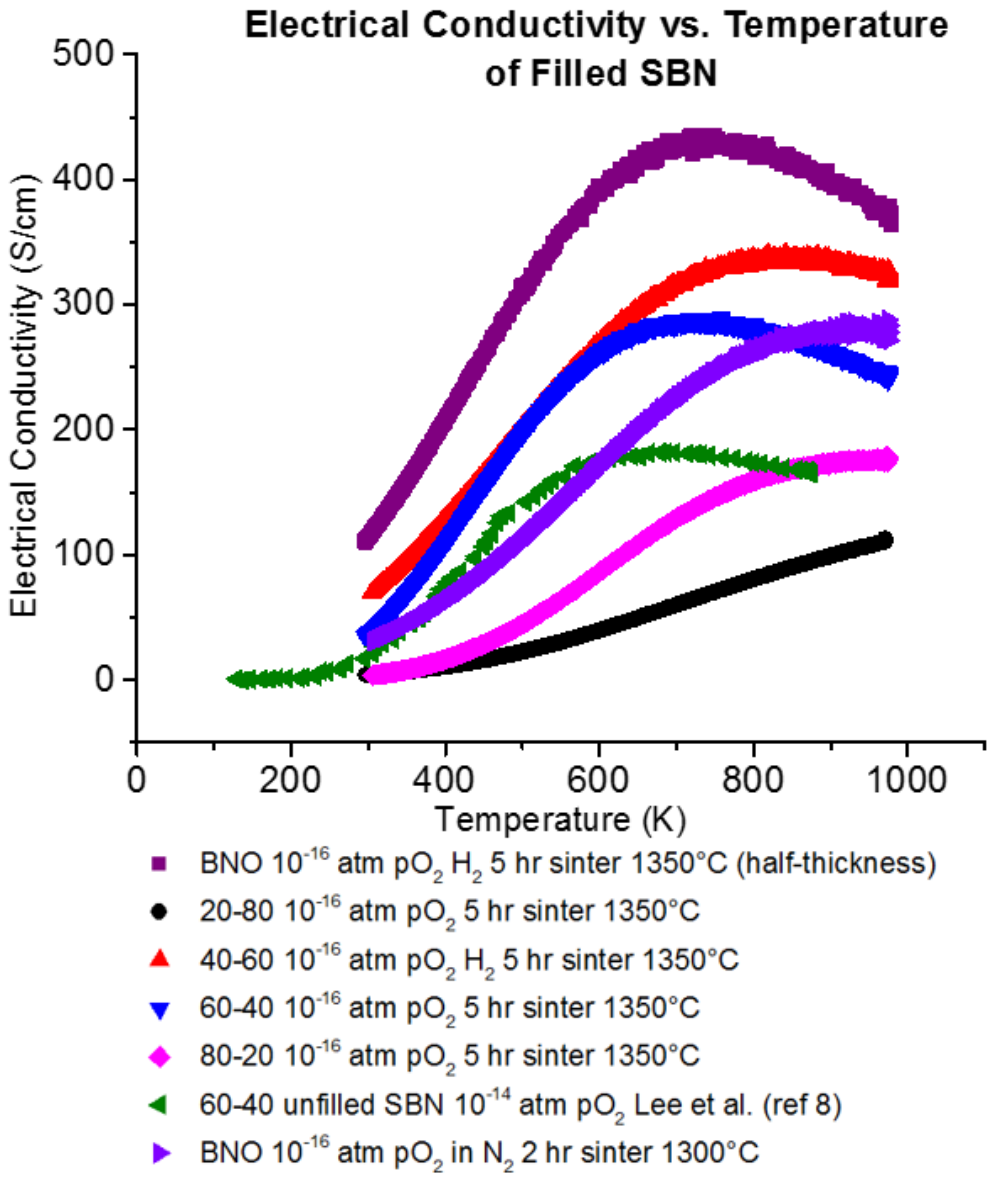

Figure 4-15. Electrical conductivities for the filled SBN compositions.

To confirm if oxidation occurred in the 20-80 sample, a new 20-80 composition was fabricated (at half the original thickness) and two measurements were conducted. The results are shown in Figure 4-16. The conductivities are high, consistent, and show a maximum, implying that the initial 20-80 sample was oxidized to a substantial degree.

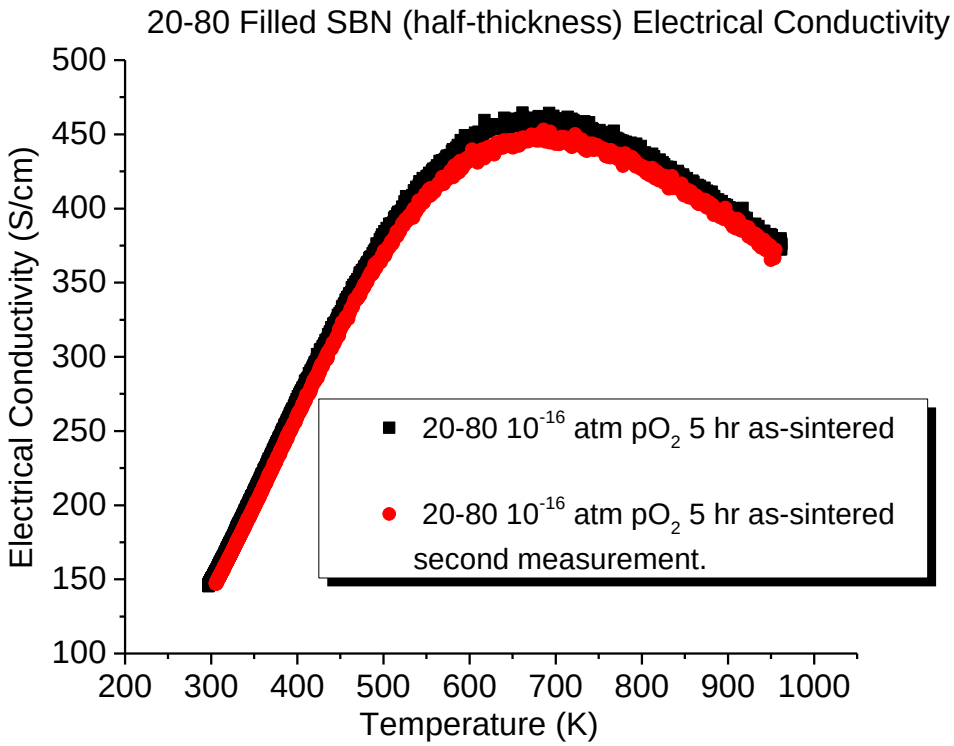

Figure 4-16. Ramp down conductivities of 20-80 filled SBN sintered at half-thickness.

The fact that the 20-80 sample was still phase pure and yet showed low electrical conductivities poses two possibilities: either there is a significant contribution from oxidized grain boundaries or the A-site filling does not directly provide carriers.[4] The latter is relevant to the A-site hypothesis: if there was phase purity, then all A-sites should be filled, resulting in a high carrier-concentration due to electronic compensation. The results in Figure 4-15 cannot differentiate which of these possibilities is correct.

To assess the validity of the A-site hypothesis that was proposed, a filled 60-40 composition and a BNO composition was annealed for 30 hours at 1300°C under 10^{-14} atm pO_2; this is the same condition for the onset of NbO_{2-x} precipitation in the unfilled SBNs. XRD confirmed that these two samples were still phase pure. The electrical conductivities

[4] The effects of grain boundaries on the conductivity have not been quantified. Impedance spectroscopy may be a useful avenue to quantify this. This will be especially useful since the low mobilities associated with hopping conduction, which would act as a limiting factor in electrical conductivity, is only valid at temperatures near room temperature.

were then measured. The results are shown in Figure 4-17. The conductivity for the 60-40 composition dropped by almost an order of magnitude and no longer showed a maximum. The conductivity of BNO decreased by almost two orders of magnitude. Despite the increase in resistivity, both samples remained black, implying a high number of carriers.

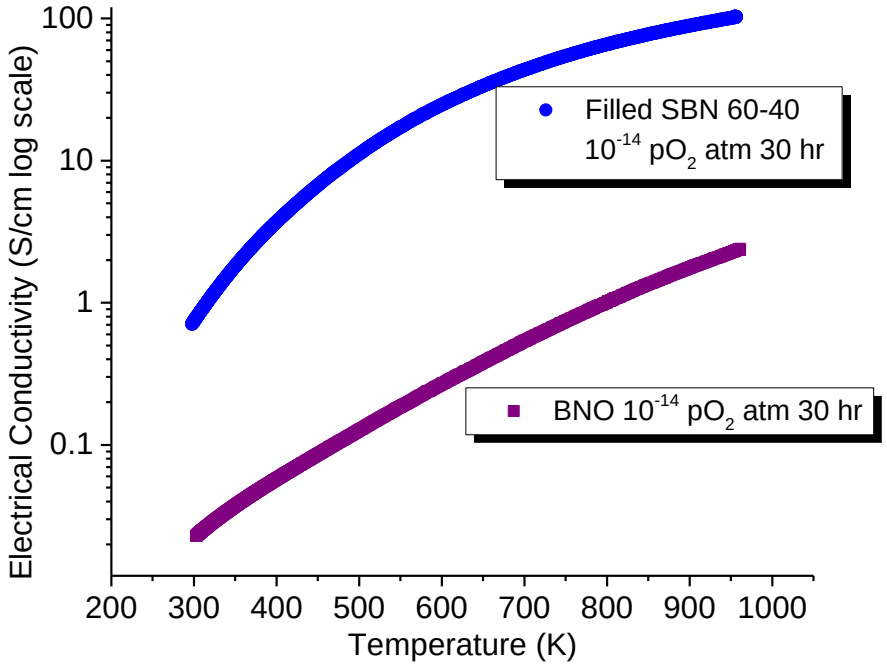

Figure 4-17. Electrical conductivities as a function of temperature for the phase-pure BNO and 60-40 filled SBN annealed at 10^{-14} atm pO_2. Note the log scale.

A conclusion regarding A-site filling and its effects on conductivity cannot be reached from Figure 4-17 alone. However the difference in carrier concentration between a filled and unfilled SBN annealed at 10^{-14} atm pO2, as will be discussed in section 4.3 below, suggests that A-site filling may not directly contribute carriers. According to the Mott criterion, having in excess of 10^{21} carriers/cm^3, one would normally expect this filled bronze to be metallic if a typical Bohr radius of a Sr or Ba oxide is used. The electrical conductivity here has a negative coefficient of resistivity, which implies the material has not been doped enough to render it metallic, but remains in the semiconducting regime.

For now, it can be said that the A-site filling plays an indirect role in increasing the electrical conductivity. The current speculation is that there is a change in how the defects are compensated after achieving site-filling. However, the effects of oxidized grain boundaries should still be considered. Further study is required to evaluate this hypothesis.

4.2.4 Electrical Conductivity

The scatter in electrical conductivity maxima in Figure 4-15 led to the speculation that the samples may not be fully equilibrated. As in the BNO samples, sample size seemed to have affected the electrical conductivities (Figure 4-9.) The kinetics may also be composition dependent, as demonstrated by Figure 4-15. To confirm this, a study was conducted examining the extent to which kinetics affected the electrical conductivity. The 40-60 composition was selected, and two sets of circular green bodies of 2.75 mm thickness ("thick") and 1.38 mm thickness ("thin") were sintered under 5 hours, 2 hours, annealed at 30 hours, at 1350°C and 1300°C under 10^{-16} atm pO_2. Each pair was processed under the same sintering or annealing schedule. The results are shown in Figure 4-18.

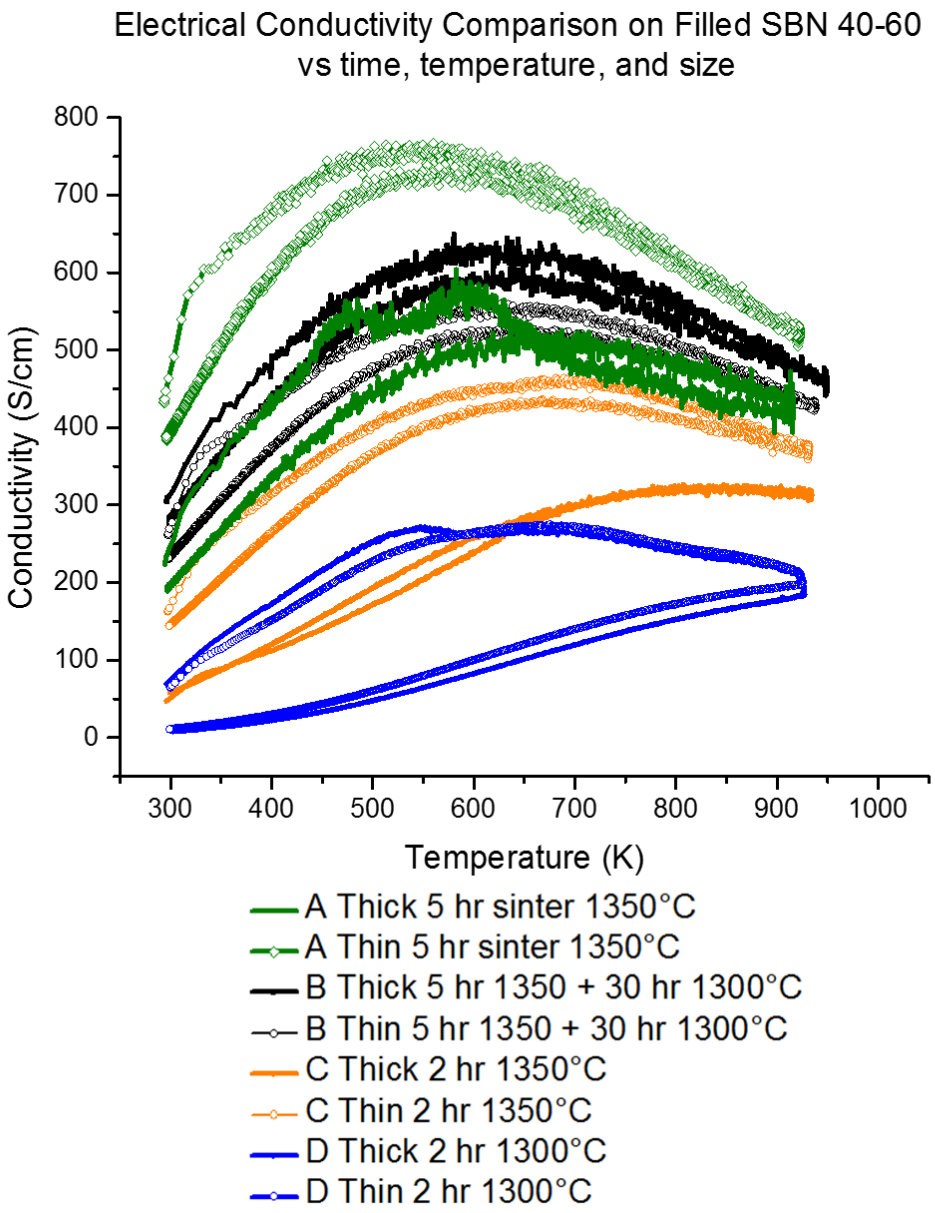

Figure 4-18. 40-60 filled SBN electrical conductivity comparing size of sample, time sintered or annealed and temperature. The ramp down (cooling) measurement is usually lower in magnitude and smoother than the ramp up[5]. Reduction atmosphere: 10^{-16} atm pO_2.

[5] The controller for this furnace automatically sets the ramp rate to maximum. Hence, if the temperature of the thermocouple and the sample are not equal due to the fast heating rate, the electrical conductivities during the ramp up may show noise within the measurement or erroneously higher conductivities.

Several insights in regards to the kinetic factors on electrical conductivity can be drawn from Figure 4-18. In the "A" samples shown in green, which are 5 hour as-sintered at 1350°C, it is clear that size plays a difference in the electrical conductivity of the samples in the present work. The room temperature conductivities and maximum conductivities in "thin A" are 400 and 700 S/cm, respectively and are almost larger than the "thick A" by a factor of 2.

Samples "B", in black, which represents the samples that have been sintered for 5 hours at 1350°C and then subjected to a 30 hour anneal at 1300°C show that the size of the green body during sintering matters less than the "A" samples. The two conductivities have similar room temperature conductivities (in the range of 250 to 300 S/cm.) Here, the "B" thick exhibits a slightly higher conductivity, which is counter-intuitive. The error propagated from geometry is on the order of +/- 0.010 cm, which only results in a +/- 30 S/cm error. The "B" samples then presumably fall within (or at least very close) error of each other. For a polycrystalline sample where grain boundaries provide a fast path for kinetics, a 30 hour anneal seems to be adequate in homogenizing samples in this size range.

The temperature in which the sintering or annealing takes place is expected to play a large role in the number of carriers present in the material. Assuming that oxygen vacancies are the primary defect species that controls the amount of carriers, an exponential or Arrhenius relationship is expected according to the Law of Mass Action[25]. The room temperature conductivity of the 5 hour as-sintered 1350°C sample ("A thin") is larger than both the conductivities of the samples subjected to the 30 hour anneal at 1300°C ("B" samples) by about a factor of 1.75. This suggests that despite the longer annealing time, the samples undergoing a 1300°C heat treatment are less reduced than a smaller sample sintered at 1350°C. This is consistent with lower temperatures being less reducing (following the Arrhenius relation.) Greater conductivities are expected if anneals were to take place at 1350°C rather than 1300°C.

The samples that are sintered at 2 hours at 1350°C ("C" samples) demonstrates that, like the 5 hour-as sintered samples, size affects the conductivity. Comparing "C thin" and "C thick", it is noted that size difference results in a factor of 2 difference in the conductivity at room temperature. This is similar to the "A samples" sintered under 5 hours.

In reduced SBN, it is presumed that the electrical conductivity will reach a maximum and then subsequently decrease with increasing temperature. This was discussed by Bock et al. to be due to the case when all carriers in the impurity band have been excited and phonon scattering effects begin to dominate. However, Figure 4-18 provides evidence that there are oxidation effects during the actual measurement. This may also contribute to the decrease in conductivity upon reaching higher temperatures. This can be seen in the "C thick" sample and the "D" samples, which are samples sintered at 2 hours under 1300°C; these three samples thus represent the least reduced samples in this experimental set. Measurements go up to 700°C, which is high enough for oxygen to be mobile. Since the measurements are done under forming gas, creating a more reducing environment at 700°C is not feasible in this experimental setup.

Samples "D" were processed under the same conditions as the calcination that formed the tungsten bronze powder. Both of the "D" samples possess the same electrical conductivities within error of one another. This is consistent with the calcination conditions; at 1300°C and 10^{-16} atm pO_2, no significant change in the oxygen activity within the material is expected and so the conductivities should be similar. This suggests that inconsistencies in the electrical conductivity are not due or limited to the motion of cations and their occupancy (which is consistent with the phase purity of the powder), but rather by the transport of oxygen. Oxygen (likely vacancies) are the primary defects that control the conductivity in SBN.

With regards to oxidation, all samples in this data set show some hysteresis resulting in a lower room temperature conductivity after heat to ~700°C. The hysteresis is consistent with oxidation during the measurement. Surprisingly, the "D" samples show the largest hysteresis. Since the "D" samples were the least reduced, it was expected that they would show the smallest hysteresis. The reason for the large hysteresis is currently unknown and it is unlikely the "D" samples are being "reduced" during ramp up and then "re-oxidized" during the ramp down.

Reduced SBN samples require an oxygen-deficient atmosphere at elevated temperatures to be stable, and hence operable. However, if they are oxidizing at their

operation temperatures, then their operational lifetimes will be cut drastically. An oxygen-deficient environment alone will not be enough to make these operable thermoelectrics.

4.2.5 Equilibrated Electrical Conductivities in the Filled and Unfilled SBNs

To give a comparison of the electrical conductivities in better equilibrated samples, compositions for which >95% density can be achieved consistently (this excludes 80-20) were remade as thinner pellets as sintered for 5 hours at 1350°C 10^{-16} atm pO_2. The ramp down results are shown in Figure 4-19.

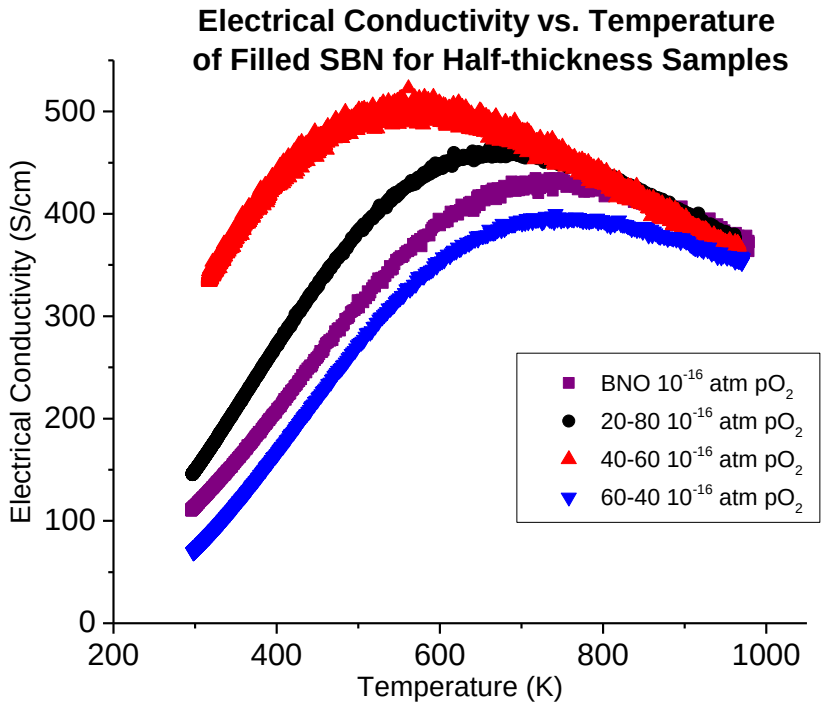

Figure 4-19. Ramp down electrical conductivities of SBN sintered at half thickness. Note that the 40-60 sample (in red) shown did not come from the same green body as the 40-60 composition in Figure 4-15.

The electrical conductivities converge at 970 K (~700°C) in these compositions when sintered under a less kinetically-limiting condition; unlike the conductivities shown in Figure 4-15. The 40-60 composition, as in Figure 4-15, demonstrates the highest

maximum electrical conductivity in the SBN solid solution as well as the highest room temperature conductivity at 330 S/cm. In these equilibrated samples, starting from BNO, the electrical conductivity increases with Sr content until reaching 60-40, where there is an overall decrease.

The variation in the electrical conductivity with composition invites speculation on the mobility of these materials as a function of composition. As discussed in the literature review, SBN at elevated temperatures is a thermally-activated-mobility band conductor and the c-axis in SBN is the high conductivity axis. The observation is consistent with the Goodenough model due to adequate orbital overlap for Nb-O-Nb bond angles near 180°[2]. Conduction through Nb and O orbitals may be possible since the Nb-O bond is about 45% covalent when Pauling electronegativities are considered. If the bond angle along the c-axis affects the electrical conductivity, it is assumed to be due to increased mobility of carriers, as octahedral tilting alone should not provide additional carriers.

Both Jamieson and Trubelja et al. comment on octahedral tilting as a function of composition: more Sr results in increased tilting[11, 26]. Therefore, it is expected that compositions with more Sr should exhibit lower conductivities. This expectation is not observed in the filled SBNs. Preliminary TEM diffraction (shown in Chapter 5: Figure 5-1) demonstrated that BNO did not show superlattice diffraction spots, implying an absence of octahedral tilting. Compositions of 20-80 and 60-40, however, do show super-lattice diffraction spots, indicating a degree of tilting in the filled bronzes, with 20-80 and 40-60 compositions showing higher electrical conductivities than BNO. Thus the correlation between electrical conductivity (mobility) and tilting is not clear. In regards to the hypothesis that degree of tilting affects carrier mobility, the effect of preferential site filling as a function of Sr content and its effects on tilting should also be considered. This requires further investigation. It is possible that the extent of oxidation is a function of composition. The different degrees of oxidation could be responsible for the differences in conductivity observed in Figure 4-19.

Despite having significantly lower conductivities in the filled SBNs relative to the unfilled SBNs annealed at 10^{-14} atm pO_2, when processed under forming gas conditions (10^{-16} atm pO_2), the filled bronzes show a higher electrical conductivity. This is shown in

Figure 4-20, in which an unfilled and filled 60-40 SBN were equilibrated under forming gas conditions with a 30 hour anneal at 1300°C. The results suggest a marked difference between a filled and unfilled bronze of SBN: either the defect compensation and/or the equilibrium concentrations of those defects differ at $10^{-14}$and 10^{-16} atm pO_2 or the mobilities are different between filled and unfilled bronzes.

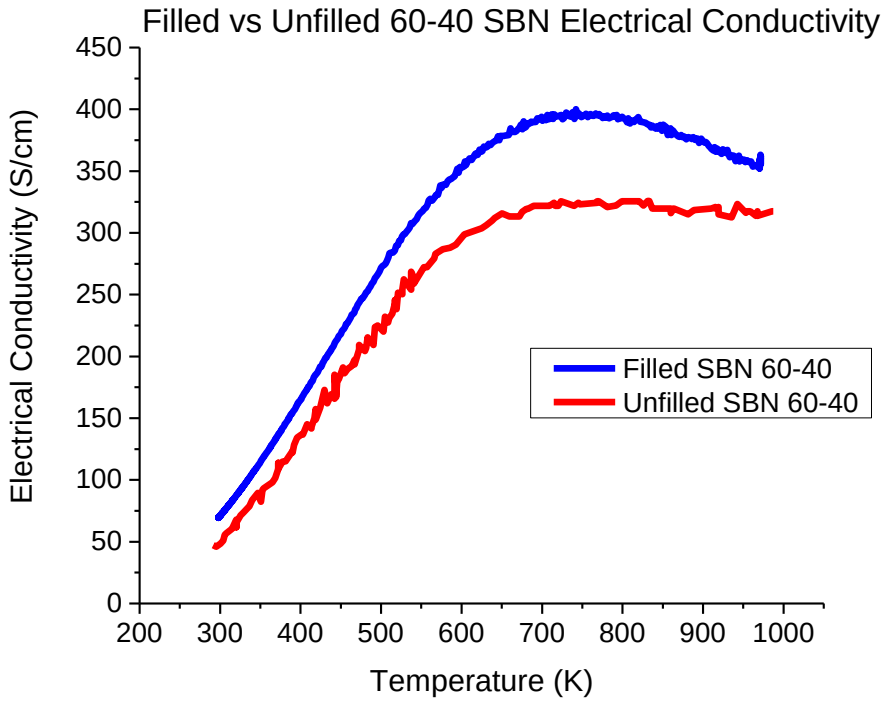

Figure 4-20. Electrical Conductivity comparison between filled and unfilled 60-40 SBN annealed for 30 hours at 1300°C under 10^{-16} atm pO_2.

4.3 Optimizing SBN as a Thermoelectric

4.3.1 Power Factors

Quantifying the power factor is crucial in assessing thermoelectric performance since they would directly indicate the processing conditions that should be used to optimize SBN, whether in the filled or unfilled case. The challenge in this work was in

obtaining accurate measurements of the Seebeck coefficient. It was found that it is difficult to quantify the instrumental error in the MMR® system. The operation relies on a small auxiliary heater to establish a temperature gradient. The assumption is that the temperature gradient between the sample being measured and the reference sample is the same. Since SBN has a low thermal conductivity, the actual temperature gradient for SBN may be greater than the temperature gradient across the reference sample (constantan wire.) If this is true, then the absolute value of the Seebeck coefficient of the material being measured will be erroneously low.

A NIST standard reference material (SRM) was used to approximate the standard deviation in the measurements as well as determine an overall "average" error. In general, a 22% error from the true value was observed. Figure 4-21 shows how this "global" error was calculated. Origin® was used to average multiple measurements on the SRM and then the averaged curve of the NIST SRM relative to the true value was used to quantify the 22% error. Since Bi_2Te_3 and SBN have a similar order of magnitude of thermal conductivity, the experimental error due to the temperature gradient is assumed to be similar. In Figure 4-21, the Seebeck coefficients are overestimated by about 22% throughout the measurement. The 22% error was propagated as a scalar.

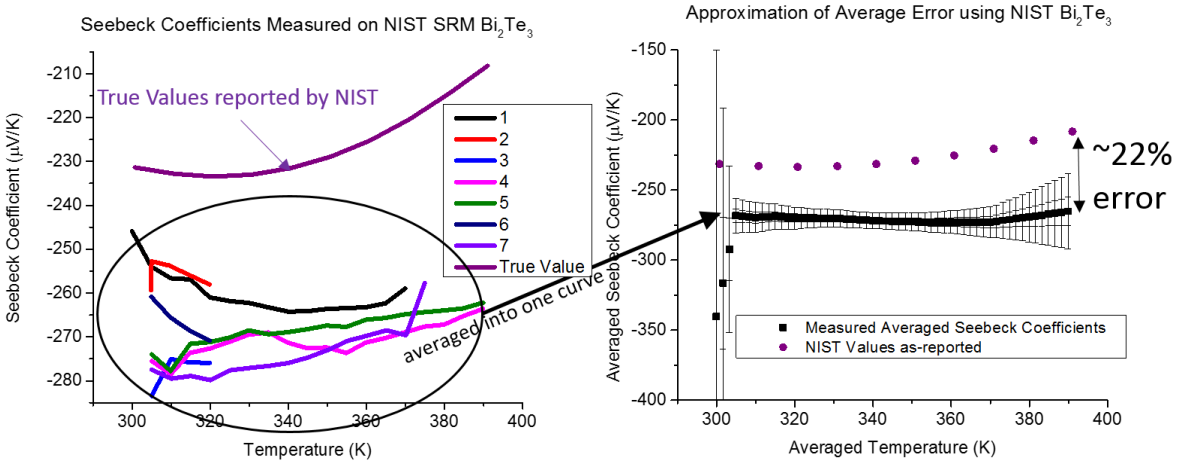

Figure 4-21. Approximation of the error in the MMR system based on NIST SRM.

This error from the NIST SRM measurement was then extrapolated to the Seebeck coefficients of the SBN samples. These samples used were the ones shown in Figure 4-15,

which were fabricated in “thick” pellets of 2.75 mm thickness. Assuming that the error in electrical conductivity is on average about 5%, the total error is about 33% for the power factor. The Seebeck coefficient and power factors for these samples are shown in Figure 4-22.

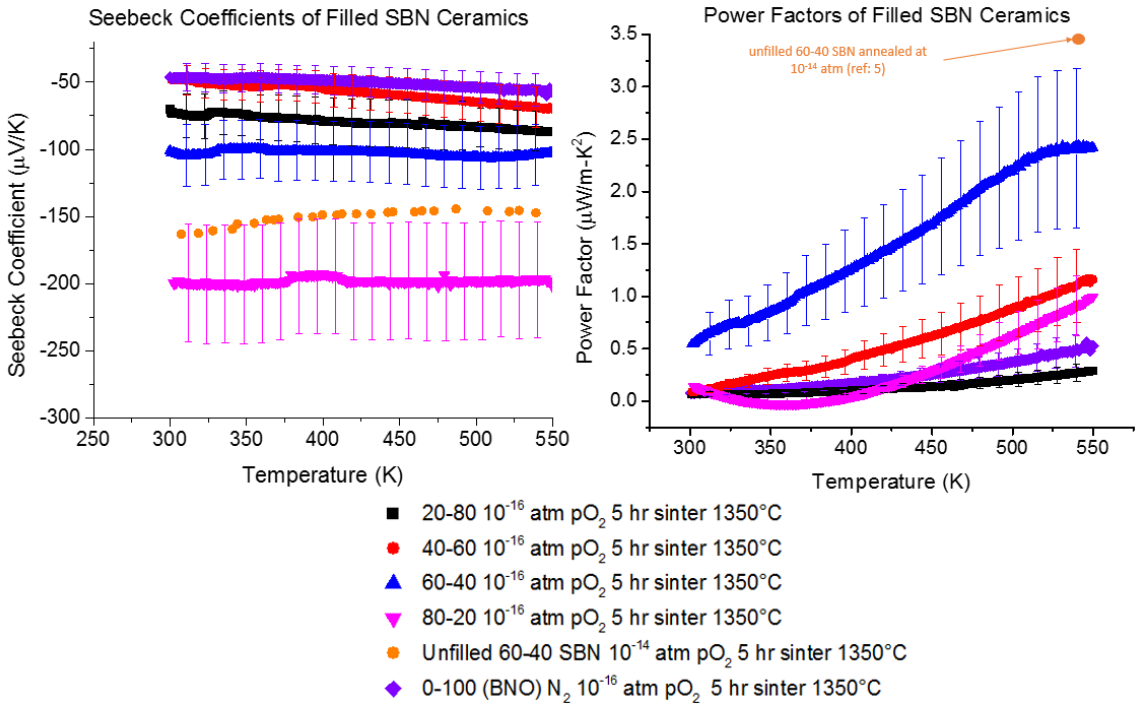

Figure 4-22. Seebeck coefficients and power factors of the filled SBN Ceramics. An error of 31.5% is assumed. Only 20 error bars are displayed for clarity. Orange reference point calculated form Bock et al.[5].

With exception to the BNO and 20-80 compositions, the Seebeck coefficients are consistent with the respective conductivities such that samples with higher electrical conductivities demonstrated lower absolute values of the Seebeck coefficient. The low Seebeck coefficient values on the 20-80 composition are believed to be because the sample was slightly oxidized as discussed earlier.

As for the BNO composition and its rather low Seebeck coefficients, the order within the crystal structure could be considered. With the framework of “entropy per charge carrier” (as discussed in the literature review), the Ba end member is believed to be the most “ordered” of the SBNs in that the Ba atoms occupy the A-sites without octahedral

tilting[27, 28]. Because there is no Sr, there is no entropy contributed by a solid solution. Assuming this hypothesis is true, then the 20-80 composition, with mostly Ba, is still ordered, leading to lower Seebeck values. However, the presence of Sr as well as the fact that Ba and Sr may still be randomly occupying the A-sites in this composition (demonstrated by not yet reaching the deviation in Vegard's Law as shown in Figure 4-11) would increase the entropy and give higher Seebeck coefficients.

The highest reported conductivity was found in the 40-60 composition, and the low Seebeck coefficients are consistent with this observation. It is expected that preferential site occupancy may be occurring here, and so the overall entropy in the material is decreased. However, the same idea cannot explain data for higher Sr compositions such as 60-40 and 80-20. These two compositions have the highest Seebeck coefficients, despite having less random site occupancy. If the disorder caused by structural distortions such as octahedral tilting increases with increasing Sr content, then perhaps it offsets the ordering from preferential site occupancy, and so may explain the higher values seen in the Seebeck coefficients.

In any case, the Seebeck coefficients in 60-40 and 80-20 have values that are consistent with their reported electrical conductivities. The three compositions that could be considered for optimizing SBN would be the 40-60, due to having the highest electrical conductivities; 80-20, for having the largest absolute value of Seebeck coefficients, and 60-40, the composition that is between these two extremes. Figure 4-22 shows that the highest power factor of $2.4\frac{\mu W}{cm-K^2}$ at 550K is from the 60-40 composition, as a result of the best compromise between the electrical conductivity and Seebeck coefficient in the filled SBNs. The optimal power factor observed in the 60-40 composition is consistent with the Seebeck and electrical conductivity data calculated from the work of Bock et al.[5].

It is noted that the power factor calculated from the data reported by Bock et al. showed that an unfilled SBN of 60-40 composition possessed a larger power factor of about $3.4\frac{\mu W}{cm-K^2}$. At least two considerations should be considered: one is the carrier concentration difference between the filled SBN of 60-40 annealed at 10^{-14} atm pO_2 and a filled SBN annealed at 10^{-16} atm pO_2; that latter is expected to be greater. The second

consideration is the presence of NbO_{2-x} as a secondary phase; it is possible that when this occurs, not all of the A-sites are occupied. The presence of a large number of A-site vacancies adds a third species in conjunction with Sr and Ba that would be expected to increase the overall disorder within the material. At 550 K, the absolute value of the Seebeck coefficient of the unfilled 60-40 SBN is greater by about $50\,\frac{\mu V}{K}$ than the filled 60-40 SBN[5].

4.3.2 Carrier Concentration: Hall Measurement and Thermogravimetric Analysis

Measuring the carrier concentration is one other way to determine an optimal reduction condition for SBN. This is assuming that SBN follows an optimal carrier concentration would be between 1.0×10^{19} and $10^{20}\,\frac{carriers}{cm^3}$, as is typical of most thermoelectrics[29]. Hall measurements using the Hall bar geometry method were used to measure the carrier concentrations of SBN as discussed in the experimental procedure. In order to investigate the importance of anisotropy and the effect of grain boundaries, a 61-39 single crystal of unfilled SBN and a 60-40 filled SBN ceramic were annealed under 1300°C for 30 hours at 10^{-16} atm pO_2. The results are shown in Figure 4-23.

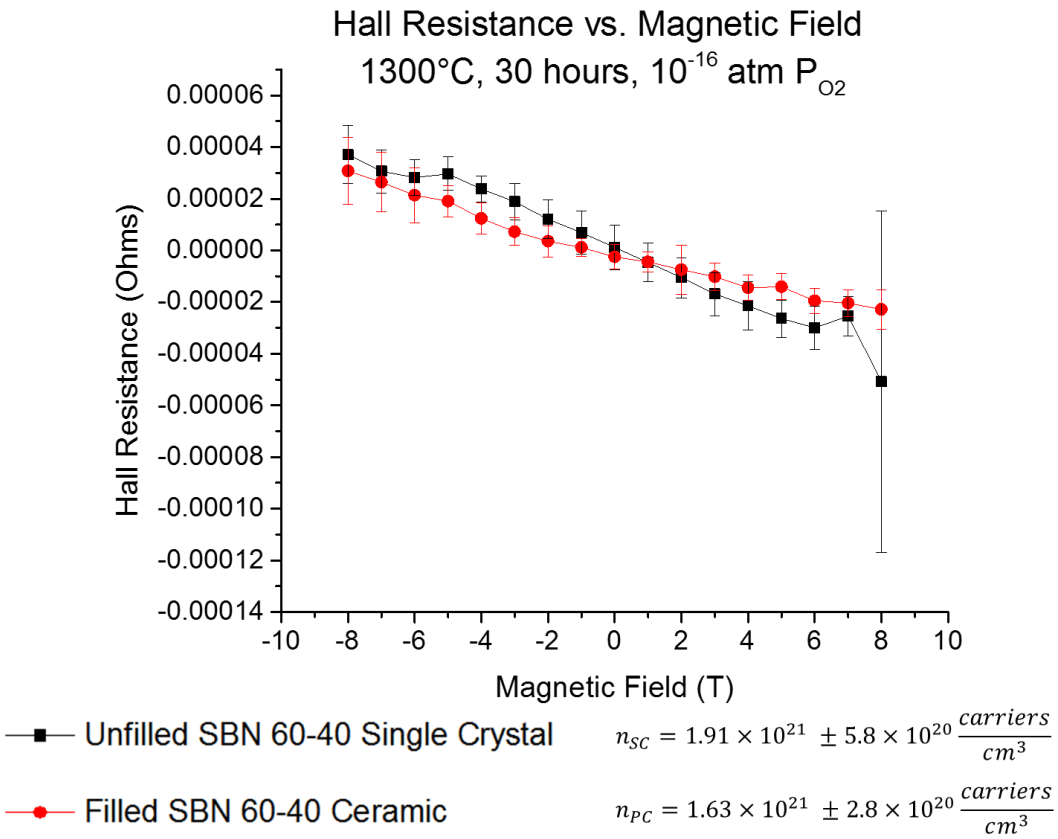

Figure 4-23. Hall measurement using Ti electrodes on unfilled single crystal and filled ceramic of 60-40 composition.

Three important indicators of "good" measurements can be derived from looking at Eq 3.12 as discussed in the experimental procedure:

$$R_{XY} = B_Z \times \frac{1}{ned} \qquad \textbf{(Eq 3.12)}$$

the Hall resistance should be linearly dependent on the applied magnetic field (slope is $\frac{R_{XY}}{B_Z}$). In going from positive to negative magnetic fields, the Hall resistance crosses 0, ideally at 0 magnetic field (if $B_Z = 0 \ \therefore R_{XY} = 0$); the sign of the slope indicates the type of charge carrier. The measurement in Figure 4-23 meets all three criteria. The degree of error on the resistance reading increases at higher magnitudes of the magnetic field due to the larger standard deviations measured by the instrument at high fields.

Figure 4-23 shows that the carrier concentration between the single crystal and the ceramic are within error of each other. In both cases, for SBN samples annealed in forming

gas conditions (10^{-16} atm pO_2) a carrier concentration on the order of 10^{21} carriers/cm^3 is observed. The slope is also consistent a negative charge carrier being the dominant carrier type.

Having established that the presence of grain boundaries should not significantly affect this type of measurement, the carrier concentration differences between the filled and unfilled SBN ceramics were investigated. In less conductive samples (as a result of higher pO_2,) instances of non-Ohmic contacts were seen on an oscilloscope when using Ti as an electrode. The use of Ga-In electrodes on barium strontium niobate as reported by Cava for Ohmic contacts was adapted for use on SBN[30]. Switching to Ga-In electrodes demonstrated a linear I-V curve, which is consistent with Ohmic contacts.[6]

The results of the differences in carrier concentration between the filled and unfilled SBN ceramics is shown in Figure 4-24. The filled 60-40 sample in Figure 4-24 is a different sample than the one showcased in Figure 4-23.[7]

[6] The Ga-In electrodes also has another benefit: since Hall measurements were conducted at room temperature, liquid Ga-In flowing was not an issue. The fact that they can be painted and adhered well is useful for cases when the electrodes need to be redone. They can simply be painted on in less than 5 minutes; this is more convenient than resorting to room sputter coaters for the deposition of Ti-Pt electrodes.

[7] The individual Hall resistance vs. magnetic field plots (i.e. such as in Figure 4-22) for the SBN ceramics under different pO_2 is displayed in the Appendix.

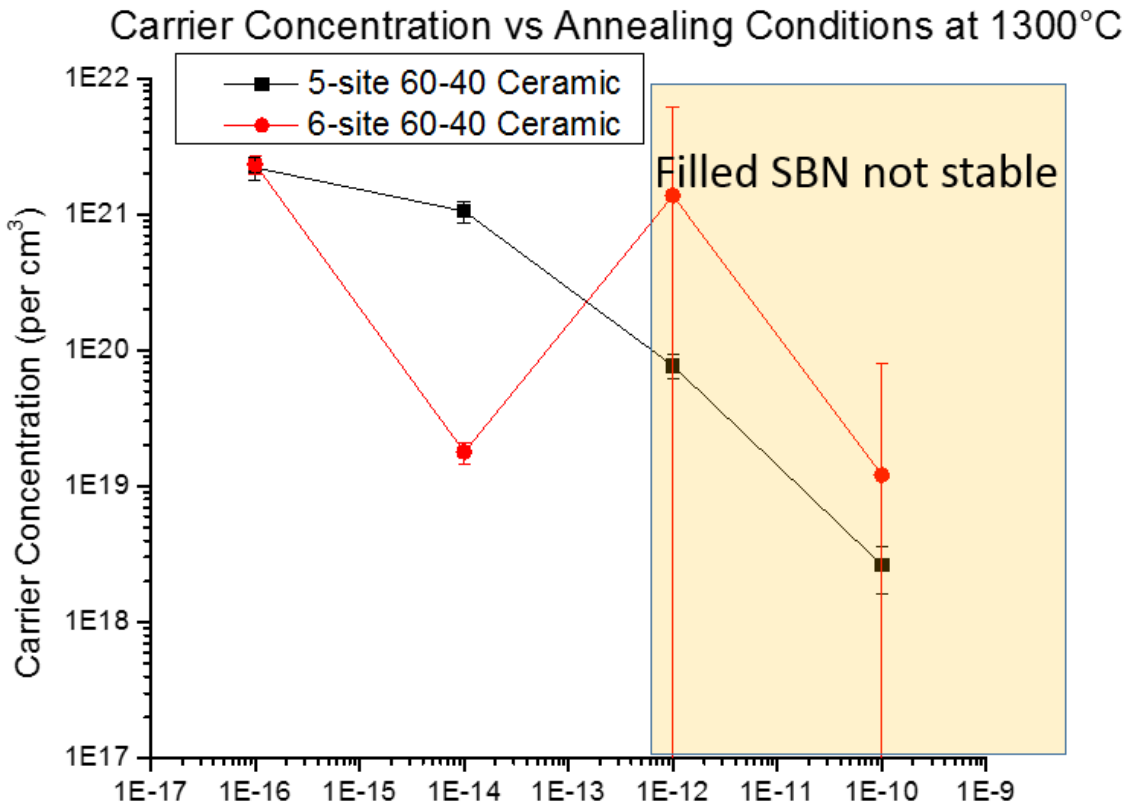

Figure 4-24. Carrier concentration vs annealing condition at 1300°C between filled and unfilled 60-40 SBN ceramics. Note the double log scale. The filled 60-40 sample is a different sample than the one shown in Figure 4-23.

At 10^{-16} atm pO_2, the carrier concentrations are within the same order of magnitude and are in error with each other: $n_{Filled-16} = 2.32 \times 10^{21} \pm 3.4 \times 10^{20} \frac{carriers}{cm^3}$ and $n_{Unfilled-16} = 2.20 \times 10^{21} \pm 4.2 \times 10^{20} \frac{carriers}{cm^3}$. However, at 10^{-14} atm pO_2, the carrier concentration differs by almost two orders of magnitude between the filled and unfilled SBN. The much lower carrier concentration in the filled SBN is consistent with Figure 4-17, in which the electrical conductivities of the filled 60-40 composition and BNO were much lower. The conductivities were lower by an order of magnitude relative to their 10^{-16} atm pO_2 counterparts.

For the 10^{-14} atm pO_2 samples, the carrier concentration differs by two orders of magnitude, but the difference in conductivity between an unfilled and filled 60-40 SBN at 10^{-14} atm is only around one order of magnitude. The error bars at 10^{-14} atm are still

relatively small for both the filled and unfilled SBN, suggesting that the mobilities of the filled and unfilled SBNs are not the same. Otherwise, it may be an indication that a filled and unfilled SBN may undergo a different extent of oxidation for a given reduction atmosphere.

The carrier concentration in unfilled SBN seems to systematically decrease with an increasing pO_2; though larger error bars are seen in more resistive samples. The large error bars in the filled SBN at 10^{-12} and 10^{-10} atm are attributed to the low conductivities in these samples. The reason for this is due to the material no longer being single phase when annealed under the 10^{-12} and 10^{-10} atm pO_2 conditions. The filled SBN is no longer stable. Having undergone the lengthy 30 hour anneal at 1300°C in these more oxidizing atmospheres, the filled tungsten bronze SBN is likely no longer even the major phase in these samples.

The results shown in Figure 4-24 show that in forming gas conditions, both filled and unfilled SBN ceramics possess a carrier concentration on the order of 10^{21} per cm^3. This is greater than the typical optimum of 1.0×10^{19} and $10^{20}\ \frac{carriers}{cm^3}$, and yet these materials are not metallic. It was shown by Lee et al. that at 10^{-14} atm pO_2, the power factor of the unfilled SBN is significantly greater than that of the 10^{-12} atm sample[4]. The extrapolation of the power factor of the unfilled 60-40 single crystal annealed at 10^{-16} atm pO_2 showed that the power factor would still increase beyond the 10^{-14} atm pO_2, suggesting even more carriers would optimize SBN[4]. From Figure 4-24, this means that SBN with 10^{21} carriers/cm^3 or more shows better thermoelectric performance than with 10^{19} carriers/cm^3. This is comparable to the behavior observed in the layered cobaltites, where the spin entropy of the electrons keeps the absolute value of the Seebeck coefficient from decreasing with high carrier concentrations[31] .

The unfilled 60-40 SBN annealed at 10^{-14} atm pO_2 demonstrated a lower, yet similar magnitude in carrier concentration as the filled SBNs annealed in 10^{-16} atm pO_2 as shown in Figure 4-24. This is consistent with the electrical conductivity difference between the unfilled and filled SBNs at 10^{-16} and 10^{-14} atm pO_2. It should not yet be concluded that the entropy given by the A-site vacancy in the unfilled SBNs was primarily responsible for the larger absolute values of the Seebeck coefficient compared to the unfilled SBNs. How the

NbO_{2-x} phase in the unfilled SBNs affects the Seebeck coefficient has not yet been investigated. An experimental study showcasing the effect on Seebeck coefficients as a function of (both minute and large) changes in carrier concentrations should be conducted.

4.4 References

1 P.B. Jamieson, S.C. Abrahams, and J.L. Bernstein, "Ferroelectric Tungsten Bronze-type Crystal Structures. I. Barium Strontium Niobate $Ba_{0.27}Sr_{0.75}Nb_2O_{5.78}$," *J. Chem. Phys.*, **48** [11] 5048–5057 (1968).

2 P.B. Jamieson, S.C. Abrahams, and J.L. Bernstein, "Ferroelectric Tungsten Bronze-type Crystal Structures. II. Barium Sodium Niobate $Ba_{(4+x)}Na_{(2-2x)}Nb_{10}O_{30}$," *J. Chem. Phys.*, **50** [10] 4352–4363 (1969).

3 M.H. Francombe and B. Lewis, "Structural, Dielectric and Optical Properties of Ferroelectric Lead Metaniobate," *Acta Crystallogr.*, **11** [10] 696–703 (1958).

4 M.H. Francombe, "The Relation Between Structure and Ferroelectricity in Lead Barium and Barium Strontium Niobates," *Acta Crystallogr.*, **13** [2] 131–140 (1960).

5 J.V. Hessen, B. Sunshine, S.A., Siegrist, T. Fiory, A.T., Waszczak, "Structure and Properties of Reduced Barium Niobium Oxide Single Crystals Obtained from Borate Fluxes," *Chem. Mater,* **3** [16] 528–534 (1991).

6 O.G. D'yachenko, S.Y. Istomin, A.M. Abakumov, and E. V. Antipov, "Synthesis, Structure, and Properties of Mixed Niobium(IV,V) Oxides," *Inorg. Mater.*, **36** [3] 247–259 (2000).

7 Y.K. Hwang and Y.-U. Kwon, "Syntheses and Electrical Properties of Tetragonal Tungsten Bronze Type Solid Solution $Ba_{6-x}La_xNb_{10}O_{30+\delta}$ (x= 0, 1, 2, 3) and $Sr_6Nb_{10}O_{30}$," *Mater. Res. Bull.*, **32** [11] 1495–1502 (1997).

8 S. Lee, R.H.T. Wilke, S. Trolier-McKinstry, S. Zhang, and C.A. Randall, "$Sr_xBa_{1-x}Nb_2O_{6-\delta}$ Ferroelectric-thermoelectrics: Crystal Anisotropy, Conduction Mechanism, and Power Factor," *Appl. Phys. Lett.*, **96** [3] 031910–1 – 031910–3 (2010).

[9] J.A. Bock, S. Trolier-McKinstry, G.D. Mahan, and C.A. Randall, "Polarization-based Perturbations to Thermopower and Electronic Conductivity in Highly Conductive Tungsten Bronze Structured (Sr,Ba)Nb_2O_6: Relaxors vs Normal Ferroelectrics," *Phys. Rev. B*, **90** [11] 115106–1 – 115106–8 (2014).

[10] S.O. Kasap, *Principles of Electronic Materials and Devices*, 3rd ed. McGraw Hill, New York, NY, 2006.

[11] B.D. Cullity, *Elements of X-ray Diffraction*, 2nd ed. Addison-Wesley, Reading, MA, 1956.

[12] P.J. Jacques, S. Allain, O. Bouaziz, A. De, A.-F. Gourgues, B.M. Hance, Y. Houbaert, J. Huang, *et al.*, "On Measurement of Retained Austenite in Multiphase TRIP Steels — Results of Blind Round Robin Test Involving Six Different Techniques," *Mater. Sci. Technol.*, **25** [5] 567–574 (2009).

[13] W.D. Kingery, H.K. Bowen, and D.R. Uhlmann, *Introduction to Ceramics*, Second. John Wiley & Sons, New York, NY, 1960.

[14] M. Trubelja, E. Ryba, and D.K. Smith, "A Study of Positional Disorder in Strontium Barium Niobate," *J. Mater. Sci.*, **31** 1435–1443 (1996).

[15] M.P. Leffler, "A Study of Positional Disorder in Strontium Barium Niobate;" M.S. Thesis, Pennsylvania State University, 1989.

[16] X.H. Zheng and X.M. Chen, "Dielectric Ceramics with Tungsten-bronze Structure in the $BaO–Nd_2O_3–TiO_2–Nb_2O_5$ System," *J. Mater. Res.*, **17** [07] 1664–1670 (2002).

[17] C.S. Dandeneau, T.W. Bodick, R.K. Bordia, and F.S. Ohuchi, "Thermoelectric Properties of Reduced Polycrystalline $Sr_{0.5}Ba_{0.5}Nb_2O_6$ Fabricated via Solution Combustion Synthesis," *J. Am. Ceram. Soc.*, **96** [7] 2230–2237 (2013).

[18] M.I. Mendelson, "Average Grain Size in Polycrystalline Ceramics," *J. Am. Ceram. Soc.*, **52** [8] 443–446 (1969).

[19] J.C. Wurst and J.A. Nelson, “Lineal Intercept Technique for Measuring Grain Size in Two-Phase Polycrystalline Ceramics,” *J. Am. Ceram. Soc.*, **55** [2] 109 (1972).

[20] C. Wood, “Materials for Thermoelectric Energy Conversion,” *Reports Prog. Phys.*, **51** 459–539 (1988).

[21] S. Lee, J.A. Bock, S. Trolier-McKinstry, and C.A. Randall, “Ferroelectric-thermoelectricity and Mott Transition of Ferroelectric Oxides with High Electronic Conductivity,” *J. Eur. Ceram. Soc.*, **32** [16] 3971–3988 (2012).

[22] R.E. Hummel, *Electronic Properties of Materials*. Springer Science & Business Media, 2011.

[23] K. Schulgasser, “Relationship Between Single-crystal and Polycrystal Electrical Conductivity,” *J. Appl. Phys.*, **47** [5] 1880–1886 (1976).

[24] Z. Hashin and S. Shtrikman, “Conductivity of Polycrystals,” *Phys. Rev.*, **130** [1] 129–133 (1963).

[25] A. Reuss, “Calculation of the Flow Limits of Mixed Crystals on the Basis of the Plasticity of Monocrystals,” *Z. Angew. Math. Mech*, **9** 49–58 (1929).

[26] W. Voigt, *Lehrbuch der Kristallphysik (mit Ausschluss der Kristalloptik)*. Springer Fachmedien, Wiesbaden ,Germany, 2014.

[27] T. Kolodiazhnyi, *Private Communication*, (2015).

[28] T. Kolodiazhnyi, H. Sakurai, O. Vasylkiv, H. Borodianska, and Y. Mozharivskyj, “Abnormal Thermal Conductivity in Tetragonal Tungsten Bronze $Ba_{6-x}Sr_xNb_{10}O_{30}$,” *Appl. Phys. Lett.*, **104** [11] 111903–1 – 110903–3 (2014).

[29] D.M. Smyth, *The Defect Chemistry of Metal Oxides*. Oxford University Press, New York, NY, 2000.

[30] P.B. Jamieson, “Ferroelectric Tungsten Bronze-Type Crystal Structures. I. Barium Strontium Niobate $Ba_{0.27}Sr_{0.75}Nb_2O_{5.78}$,” *J. Chem. Phys.*, **48** [11] 5048–5057 (1968).

[31] H.K. Rockstad, R. Flasck, and S. Iwasa, “Seebeck Coefficient in Amorphous Chalcogenide Films,” *J. Non. Cryst. Solids*, **8-10** 326–330 (1972).

[32] P.A. Cox, *Transition Metal Oxides: an Introduction to their Electronic Structure and Properties*. Oxford University Press, New York, NY, 2010.

[33] G.J. Snyder and E.S. Toberer, “Complex Thermoelectric Materials,” *Nat. Mater.*, **7** [2] 105–14 (2008).

[34] R.J. Cava, W.F. Peck Jr, J.J. Krajewski, and D.A. Fleming, “Compensation of the Temperature Coefficient of the Dielectric Constant of Barium Strontium Titanate,” *Appl. Phys. Lett.*, **67** [25] 3813–3815 (1995).

[35] I. Terasaki, “Layered Cobalt Oxides: Correlated Electrons for Thermoelectrics;” pp. 51–70 in *Thermoelectr. Nanomater. SE - 3*. Edited by K. Koumoto and T. Mori. Springer Berlin Heidelberg, 2013.

Chapter 5

Conclusions and Future Work

5.1 Summary of Findings

The primary objective of this thesis was to investigate the A-site filling in SBN motivated by the high power factors reported by Lee et al. and the high electrical conductivities in the barium end member single crystal reported by Hessen et al.[1, 2]. The barium end member was used as a model system to provide a framework for studying the other SBN compositions. In order to facilitate systematic studies, a conventional synthesis method was desirable in lieu of the 60-100 hour annealing times via vacuum ampoules as a single crystal by-product[2–4].

The objective of proving A-site filling in BNO and SBN (and by using solid-state processing methods) was achieved in this thesis. With BNO as the model system, it was shown that at annealing conditions below about 10^{-14} atm pO_2 at 1300°C, the filled tungsten bronze phase is unstable, which coincides with the onset of anomalous electrical conductivity increase reported by Lee et al.[5]. The evidence for A-site filling was provided by XRD in which no secondary phases were detectable; SEM, in which no secondary phase contrast was observed, and by similar magnitudes in electrical conductivity when sintered at 10^{-16} atm pO_2. The occurrence of A-site filling was further checked by quantitative EDS, which showed a distinction in the Sr and Ba content between a filled and unfilled bronze, and a TEM micrograph that showed no observable secondary phases along grain boundaries.

The second objective was to investigate the extent of site-filling across the composition range of SBN. This objective is also tied to the hypothesis of A-site filling being responsible for the anomalous increase in electrical conductivity. It was believed that the occupancy of one Sr or Ba atom would be compensated by two electrons, leading to an

increase in charge carriers on the order of $10^{21}/cm^3$. If this was true, then high electrical conductivities would be expected regardless of composition if phase purity is achieved. The results showed that filled SBN can be fabricated up to the 80-20 composition, with preferential site occupancy occurring somewhere between the 20-80 and 40-60 compositions. While similar magnitudes of electrical conductivity were found in 10^{-16} atm annealed samples, it was found that BNO and 60-40 remained phase pure at 10^{-14} atm pO_2, but suffered a major decrease in electrical conductivity. The low electrical conductivity was supported by Hall measurements showing a two order of magnitude decrease in the carrier concentration. It was not conclusive if the oxidized grain boundaries or the possibility of the A-site filling hypothesis being incorrect was the cause for this observation. If A-site filling was not solely responsible for the high electrical conductivities, then it is likely that it played an indirect role by changing the nature of how the defects were being compensated.

With the goal of designing a high-performing n-type oxide thermoelectric, it can be concluded that filled SBN bronzes annealed at 10^{-16} atm is not the optimal composition or annealing condition for high power factors. The carrier concentration was on the order of $10^{21}/cm^3$, which lies on the extreme end of what is expected to be the optimal range of 10^{19}-$10^{20}/cm^3$. Because of the complexity and flexibility of the tungsten bronze structure, there are still many variables and chemistries (i.e. C-sites) that can be explored with respect to optimizing an oxide thermoelectric.

5.2 Future Work

The electrical conductivity was the primary property of interest in this thesis. However, there are two terms, the mobility and carrier concentration, that ultimately affect this quantity. Only the carrier concentration has been characterized in this work. However, as discussed by Bock et al., there is an expectation that at higher temperatures (above ~450 K), the conduction mechanism is now a band conductor with mobility edges. The electrical conductivity would no longer be limited by the low mobilities of hopping conduction and

so the magnitude of the mobility should be considered. Related to the mobility is the validity of the high electrical conductivity reported in the BNO single crystal by Hessen et al.[2]. The conductivity along the c-axis reported in this material is two orders of magnitude larger than the a-axis, which is inconsistent with the just the single order of magnitude observed in unfilled SBN single crystals[5]. As a single crystal, the effects of oxidized grain boundaries is negated. Hence, for a single crystal of BNO, the absence of octahedral tilting and lack of oxidized grain boundaries may be correlated to higher mobilities and electrical conductivities. One could start by synthesizing a single crystal of BNO and confirming the values (and the reproducibility) of the electrical conductivity.

If according to Jamieson and Trubelja et al., Ba provides more upright octahedra than Sr, then the hypothesis of octahedral tilting affecting mobility along the c-axis should be explored. Preliminary results have shown that BNO lacks superlattice diffraction spots in TEM, implying no octahedral tilting, whereas in 60-40 filled SBN, superlattice diffractions can be seen. This is shown in Figure 5-1.

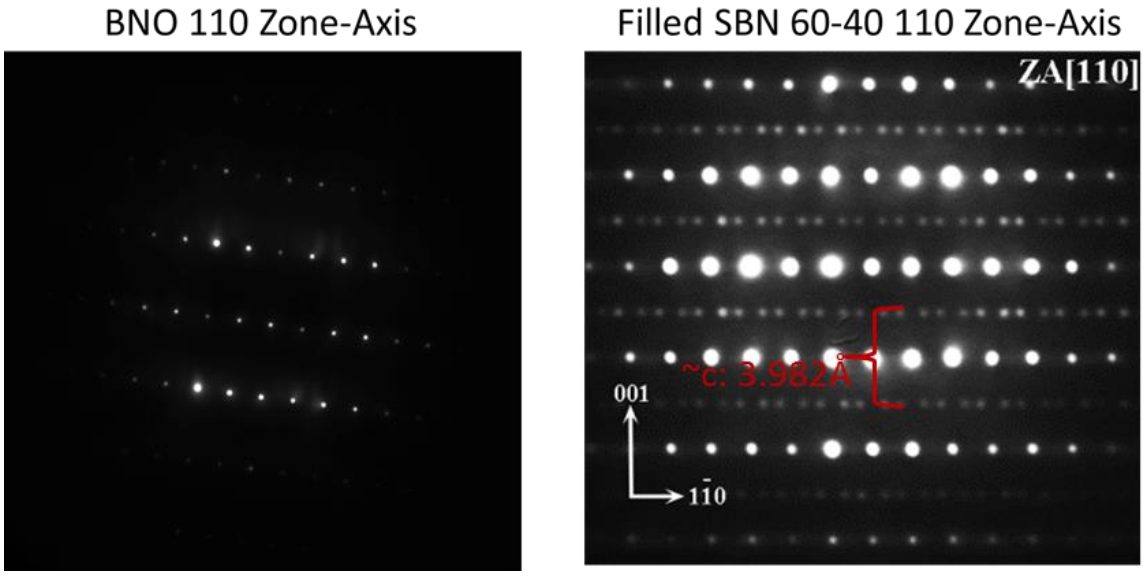

Figure 5-1. TEM diffraction in filled SBN viewed along [110] zone-axis. BNO exhibits no superlattice diffraction spots, while the 60-40 composition shows the presence of superlattice diffraction spots.

The superlattice diffraction shown in Figure 5-1 on the 60-40 composition viewed along [110] appears to occur in multiples of the c-axis length. Therefore, along c, the octahedral tilting appears to be commensurate with the structure. This is consistent with reported diffractions in other filled and unfilled tetragonal tungsten bronzes as reported by Levin et al., Randall et al., and Bursill et al.[6–8]. Figure 5-1 also shows that there are more instances of the superlattice diffractions than there are of the primary structure diffractions along [110] in the 60-40 filled SBN. This was also observed in the work of Bursill et al. in the unfilled SBNs. [7]. Along [110], Levin et al. depicted the transition of a commensurate superlattice into an incommensurate distortion when observing the diffraction pattern of $Ba_2NdNb_3Ti_2O_{15}$ at 423 K and 453 K, respectively[6]. The degree of deviation from commensurate periodicity, δ, was between 0.050 and 0.034 depending on temperature; where δ=0 means commensurate[6]. The superlattice diffractions of SBN in Figure 5-1 resembles those in the incommensurate transition of $Ba_2NdNb_3Ti_2O_{15}$ reported by Levin et al.[6]. Thus, the filled SBNs seem to have an incommensuration along [110.]

If there was ferroelectric behavior in these filled SBNs, it is possible the 60-40 composition of the filled SBN may be not be a relaxor ferroelectric. Based on the crystal-chemical framework using tolerance factors as modeled by Zhu et al., the tolerance factor of the A1 site and the average A site size (A1+A2/2), this composition lies within the normal ferroelectric region[9]. This contrasts with the unfilled counterpart at this composition, in which relaxor behavior is observed at this composition. Experimental evidence is required to verify the speculation of normal ferroelectric behavior in filled 60-40 SBN. This is especially true since exceptions to the model proposed by Zhu et al exist. This includes $Sr_4Na_2Nb_{10}O_{30}$, which is a normal ferroelectric, but was predicted to be a relaxor[9].

If carrier mobility as a function of octahedral tilt is investigated, compositions can be made with increasing Sr content in intervals of 5% up to 80-20. If may be possible to evaluate the degree of octahedral tilting by quantifying the relative intensities of the superlattice diffractions. A study in quantifying the degree of tilting could be correlated to the mobility, which could be measured by a Hall experiment. Being able to adjust the

mobility via octahedral tilting without changing the carrier concentration would help retain higher Seebeck coefficients, and preserve high electrical conductivities.

As discussed in the Chapter 4, the effects of preferential site occupancy on degree of tilting should also be investigated if mobility and tilting is being studied. Of course, before initiating studies between tilting and electrical conductivity, the extent of oxidation as a function of composition should be investigated by impedance spectroscopy and/or thermogravimetric analysis (TGA). If impedance spectroscopy shows that the resistance contributions from grain boundaries are decreasing with increasing Sr content from BNO to the 40-60 composition, then it is likely the observed differences in electrical conductivities in Figure 4-19 may be better explained by oxidation. TGA should be used to independently confirm this: more oxidized samples would show increased oxygen up-take.

This work had suggested the possibility that A-site filling was not solely responsible for the dramatic increase in conductivity. Its role is still unclear. A likely hypothesis is that it affects the way defects are compensated. This was shown by the conductivity differences between the unfilled and filled SBNs annealed at 10^{-14} atm pO_2 and the carrier concentration that was evaluated. The development of a Brouwer diagram as a function of pO_2 between the filled and unfilled SBNs would show when the compensation mechanism starts to deviate.

In making SBN a realistic commercial thermoelectric, there is a problem in regards to oxidation. The operating temperature for SBN is expected to be around 550-750 K, where zT would be highest. However, under atmospheric conditions, this would eventually oxidize SBN, dramatically reducing the operation lifetime of the device. Degradation in an open atmosphere will limit the applicability of this material. Methods to prevent oxidation, such as atomic layer deposition coatings, could be pursued. Or, given the flexibility in the structure, another way to electronically compensate defects without relying on oxygen activity should be pursued.

On optimizing SBN, more accurate Seebeck measurements are required. The ~32% error shown in Figure 4-22 is high, and even though the power factor is below that of the unfilled SBN, a more accurate assessment is necessary in systematically investigating the effect of carrier concentration on the magnitude of the Seebeck coefficient. This will be important in optimizing SBN. The high conductivities observed in the equilibrated samples of filled SBN (and in particular the 40-60 composition, which had almost 300 S/cm at room temperature) should have its power factor evaluated, for it is possible that SBN could have a lower operational temperature than previously indicated. This would also somewhat resolve the oxidation problem.

It should be noted that, in the work by Bock et al., the short-range polarization due to relaxor ferroelectricity lowered the absolute value of the Seebeck coefficient from about 250K to about 525 K in SBN.[10] It has been reported, but not confirmed that the filled SBNs exhibit centro-symmetry and is not expected to have any ferroelectric character from room temperature and above. The Seebeck measurements in Figure 4-22 also do not show the parabolic U-shaped trend from 250K to 525 K. It was found that compositions from BNO to 60-40 can be oxidized at 600°C to become insulating and remain single phase. Dielectric measurements were conducted on an oxidized 60-40 sample in which at room temperature, the material behaved like a linear dielectric. When measuring the dielectric constant and loss, it was observed that space charge contributions from excited carriers occurred from 100°C to 200°C. At temperatures below room temperature, there is evidence of some type of dielectric relaxation. This is shown in Figure 5-2.

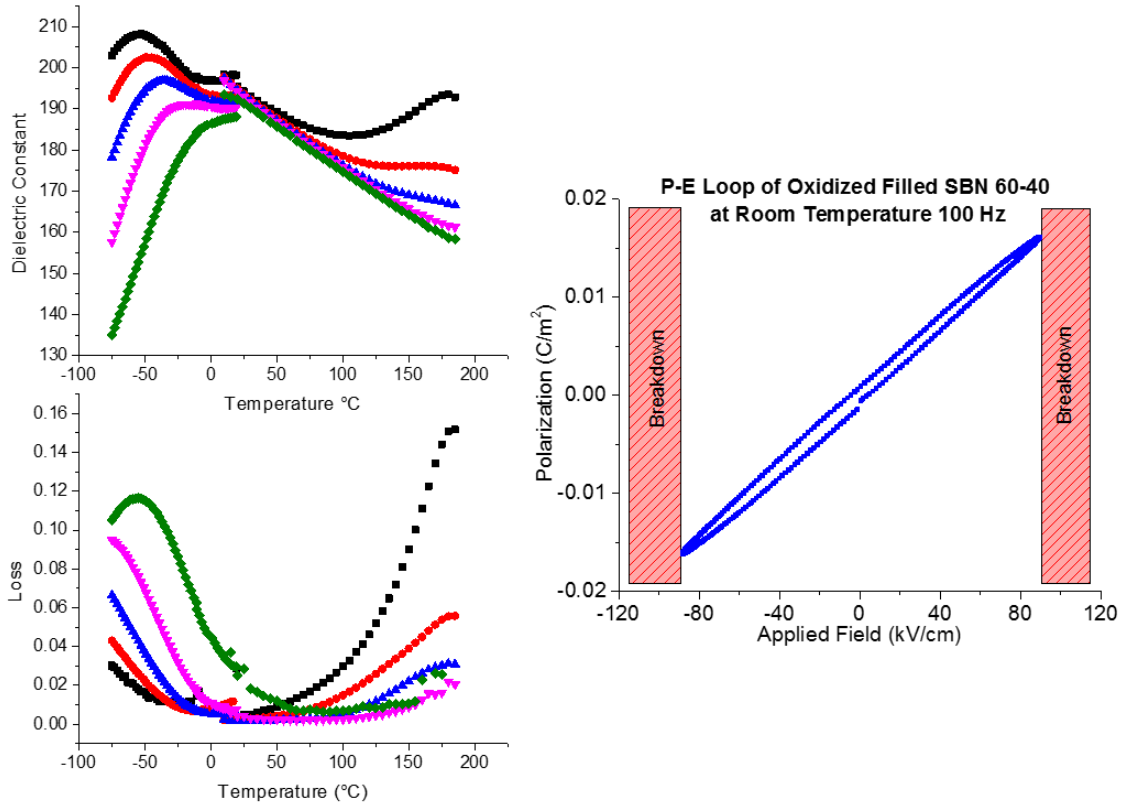

Figure 5-2. Dielectric and P-E loop measurements on a phase-pure, oxidized, filled SBN of 60-40 composition. The disjoint in the dielectric data is due to the plot consisting of two separate measurements: one above room temperature, and one below room temperature.

The fact that no polarization is found at room temperature and above suggests that there is no polarization that could diminish the Seebeck coefficient. Avenues of exploring a lower operating temperature for SBN is therefore, recommended.

5.3 References

[1] S. Lee, J.A. Bock, S. Trolier-McKinstry, and C.A. Randall, "Ferroelectric-thermoelectricity and Mott Transition of Ferroelectric Oxides with High Electronic Conductivity," *J. Eur. Ceram. Soc.*, **32** [16] 3971–3988 (2012).

[2] J.V. Hessen, B. Sunshine, S.A., Siegrist, T. Fiory, A.T., Waszczak, "Structure and Properties of Reduced Barium Niobium Oxide Single Crystals Obtained from Borate Fluxes," *Chem. Mater*, **3** [16] 528–534 (1991).

[3] O.G. D'yachenko, S.Y. Istomin, A.M. Abakumov, and E. V. Antipov, "Synthesis, Structure, and Properties of Mixed Niobium(IV,V) Oxides," *Inorg. Mater.*, **36** [3] 247–259 (2000).

[4] Y.K. Hwang and Y.-U. Kwon, "Syntheses and Electrical Properties of Tetragonal Tungsten Bronze Type Solid Solution $Ba_{6-x}La_xNb_{10}O_{30+\delta}$ (x= 0, 1, 2, 3) and $Sr_6Nb_{10}O_{30}$," *Mater. Res. Bull.*, **32** [11] 1495–1502 (1997).

[5] S. Lee, R.H.T. Wilke, S. Trolier-McKinstry, S. Zhang, and C.A. Randall, "$Sr_xBa_{1-x}Nb_2O_{6-\delta}$ Ferroelectric-thermoelectrics: Crystal Anisotropy, Conduction Mechanism, and Power Factor," *Appl. Phys. Lett.*, **96** [3] 031910–1 – 031910–3 (2010).

[6] I. Levin, M.C. Stennett, G.C. Miles, D.I. Woodward, A.R. West, and I.M. Reaney, "Coupling Between Octahedral Tilting and Ferroelectric Order in Tetragonal Tungsten Bronze-structured Dielectrics," *Appl. Phys. Lett.*, **89** [12] 122908–1 – 122908–3 (2006).

[7] L.A. Bursill and P.J. Lin, "Electron Microscopic Studies of Ferroelectric Crystals: Detection of Weak Symmetry Elements," *Ultramicroscopy*, **18** [1] 235–240 (1985).

[8] C.A. Randall, R. Guo, A.S. Bhalla, and L.E. Cross, "Microstructure-property Relations in Tungsten Bronze Lead Barium Niobate, $Pb_{1-x}Ba_xNb_2O_6$," *J. Mater. Res.*, **6** [08] 1720–1728 (1991).

[9] X. Zhu, M. Fu, M.C. Stennett, P.M. Vilarinho, I. Levin, C.A. Randall, J. Gardner, F.D. Morrison, *et al.*, "A Crystal-Chemical Framework for Relaxor versus Normal Ferroelectric Behavior in Tetragonal Tungsten Bronzes," *Chem. Mater.*, **27** [9] 3250–3261 (2015).

[10] J.A. Bock, S. Trolier-McKinstry, G.D. Mahan, and C.A. Randall, "Polarization-based Perturbations to Thermopower and Electronic Conductivity in Highly Conductive Tungsten Bronze Structured (Sr,Ba)Nb_2O_6: Relaxors vs Normal Ferroelectrics," *Phys. Rev. B*, **90** [11] 115106–1 – 115106–8 (2014

Appendix

SBN Hall Measurements: Hall Resistance vs. Magnetic Field

Below is the individual Hall measurements (that have been corrected for electrode misalignment) used to generate Figure 4-24.

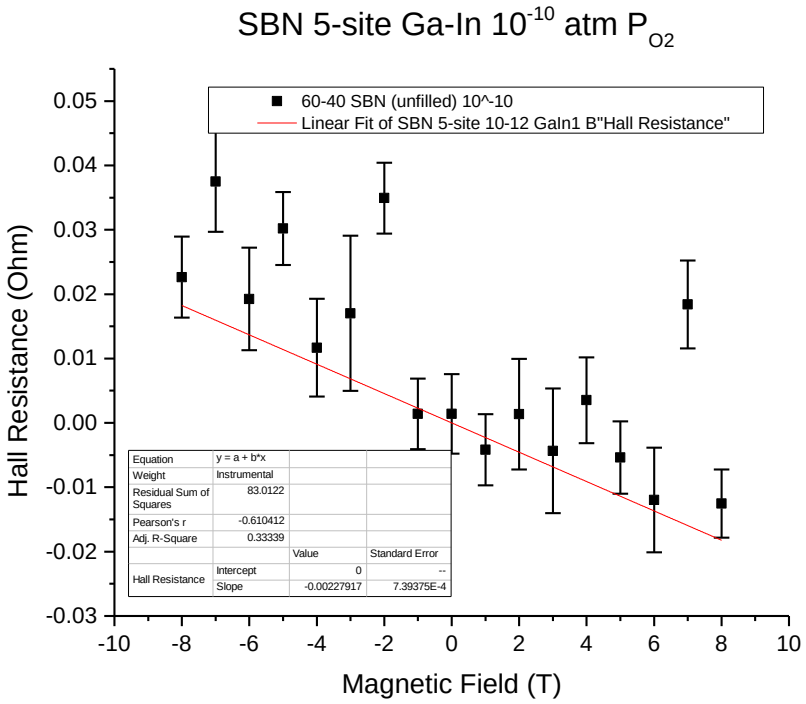

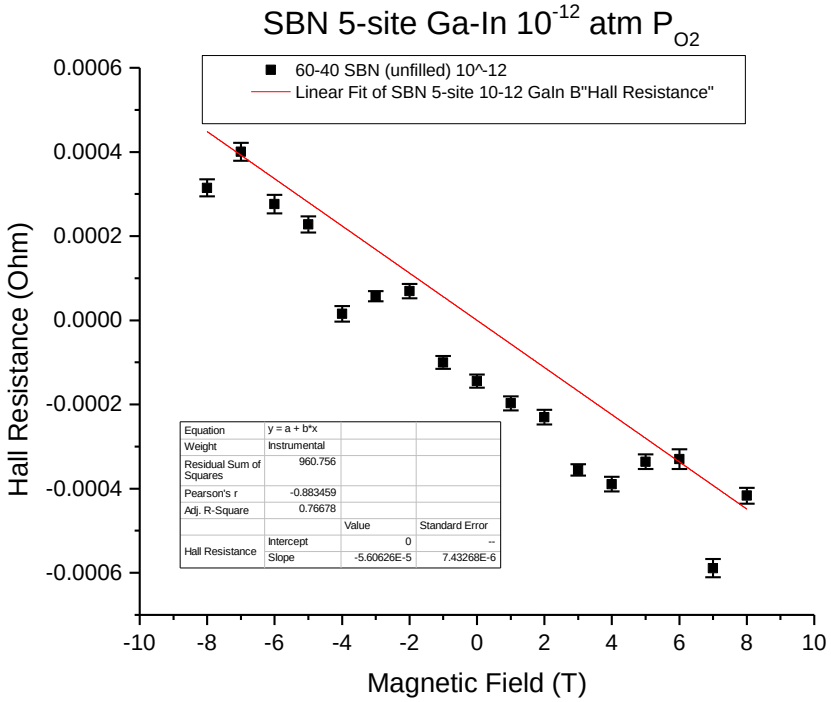
SBN 5-site Ga-In 10-12 atm PO2
60-40 SBN (unfilled) 10^-12
Linear Fit of SBN 5-site 10-12 GaIn B"Hall Resistance"
Hall Resistance (Ohm)
Magnetic Field (T)
0.0006
0.0004
0.0002
0.0000
-0.0002
-0.0004
-0.0006
-10
-8
-6
-4
-2
0
2
4
6
8
10
Equation y = a + b*x
Weight Instrumental
Residual Sum of Squares 960.756
Pearson's r -0.883459
Adj. R-Square 0.76678
Value Standard Error
Hall Resistance Intercept 0 --
Hall Resistance Slope -5.60626E-5 7.43268E-6

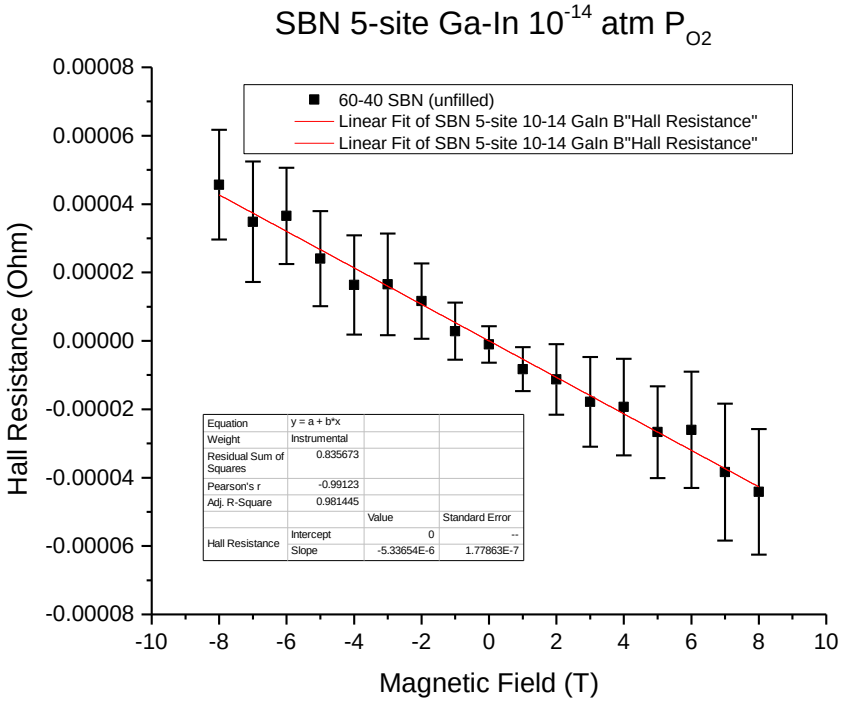
SBN 5-site Ga-In 10-14 atm PO2
60-40 SBN (unfilled)
Linear Fit of SBN 5-site 10-14 GaIn B"Hall Resistance"
Linear Fit of SBN 5-site 10-14 GaIn B"Hall Resistance"
Hall Resistance (Ohm)
Magnetic Field (T)
0.00008
0.00006
0.00004
0.00002
0.00000
-0.00002
-0.00004
-0.00006
-0.00008
-10
-8
-6
-4
-2
0
2
4
6
8
10
Equation y = a + b*x
Weight Instrumental
Residual Sum of Squares 0.835673
Pearson's r -0.99123
Adj. R-Square 0.981445
Value Standard Error
Hall Resistance Intercept 0 --
Hall Resistance Slope -5.33654E-6 1.77863E-7

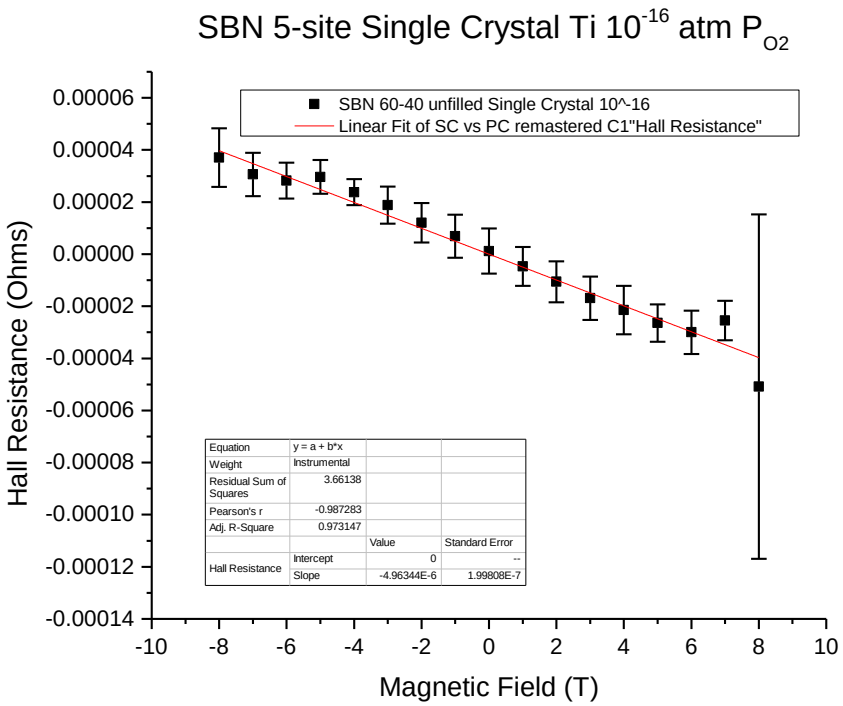
SBN 5-site Single Crystal Ti 10-16 atm PO2
SBN 60-40 unfilled Single Crystal 10^-16
Linear Fit of SC vs PC remastered C1"Hall Resistance"
Hall Resistance (Ohms)
Magnetic Field (T)
Equation y = a + b*x
Weight Instrumental
Residual Sum of Squares 3.66138
Pearson's r -0.987283
Adj. R-Square 0.973147
Value Standard Error
Hall Resistance Intercept 0 --
Hall Resistance Slope -4.96344E-6 1.99808E-7

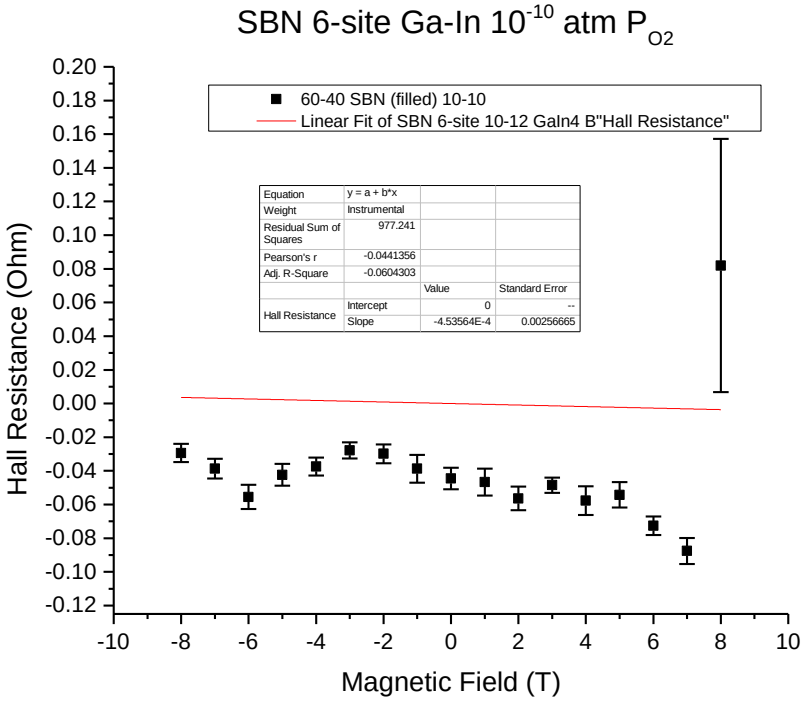
SBN 6-site Ga-In 10-10 atm PO2
60-40 SBN (filled) 10-10
Linear Fit of SBN 6-site 10-12 GaIn4 B"Hall Resistance"
Hall Resistance (Ohm)
Magnetic Field (T)
Equation y = a + b*x
Weight Instrumental
Residual Sum of Squares 977.241
Pearson's r -0.0441356
Adj. R-Square -0.0604303
Value Standard Error
Hall Resistance Intercept 0 --
Hall Resistance Slope -4.53564E-4 0.00256665

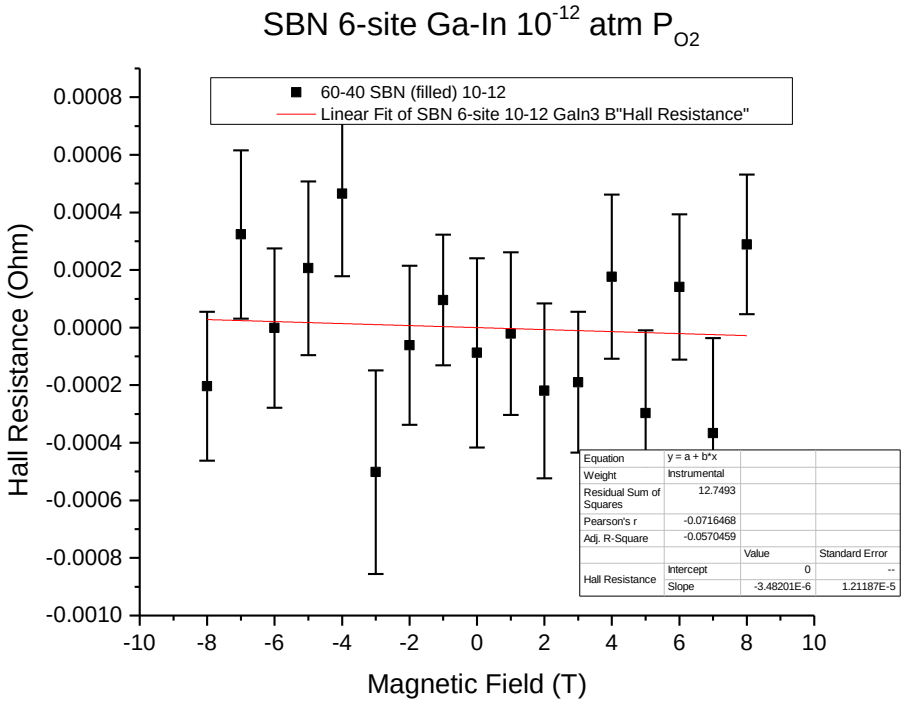
SBN 6-site Ga-In 10-12 atm PO2
60-40 SBN (filled) 10-12
Linear Fit of SBN 6-site 10-12 GaIn3 B"Hall Resistance"
Hall Resistance (Ohm)
Magnetic Field (T)
0.0008
0.0006
0.0004
0.0002
0.0000
-0.0002
-0.0004
-0.0006
-0.0008
-0.0010
-10
-8
-6
-4
-2
0
2
4
6
8
10
Equation y = a + b*x
Weight Instrumental
Residual Sum of Squares 12.7493
Pearson's r -0.0716468
Adj. R-Square -0.0570459
Value Standard Error
Hall Resistance Intercept 0 --
Hall Resistance Slope -3.48201E-6 1.21187E-5

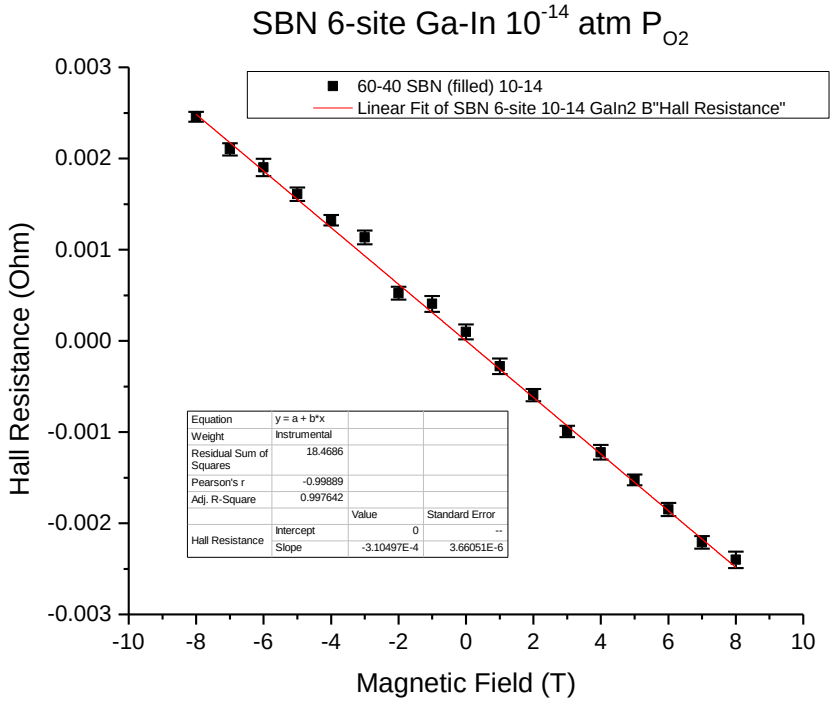
SBN 6-site Ga-In 10-14 atm PO2
60-40 SBN (filled) 10-14
Linear Fit of SBN 6-site 10-14 GaIn2 B"Hall Resistance"
Hall Resistance (Ohm)
Magnetic Field (T)
0.003
0.002
0.001
0.000
-0.001
-0.002
-0.003
-10
-8
-6
-4
-2
0
2
4
6
8
10
Equation y = a + b*x
Weight Instrumental
Residual Sum of Squares 18.4686
Pearson's r -0.99889
Adj. R-Square 0.997642
Value Standard Error
Hall Resistance Intercept 0 --
Hall Resistance Slope -3.10497E-4 3.66051E-6

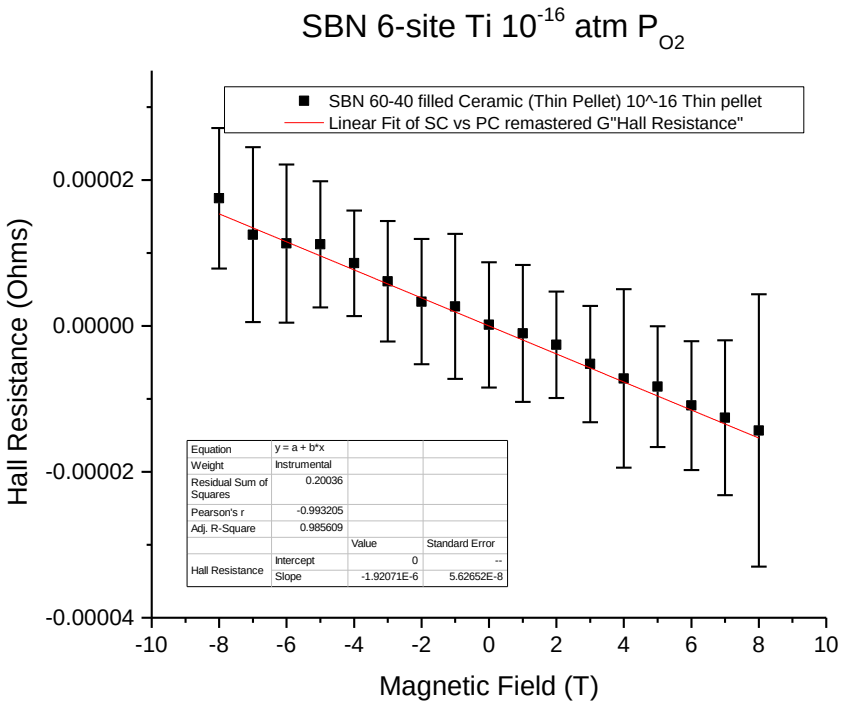
SBN 6-site Ti 10-16 atm PO2
SBN 60-40 filled Ceramic (Thin Pellet) 10^-16 Thin pellet
Linear Fit of SC vs PC remastered G"Hall Resistance"
Hall Resistance (Ohms)
0.00002
0.00000
-0.00002
-0.00004
-10
-8
-6
-4
-2
0
2
4
6
8
10
Magnetic Field (T)
Equation y = a + b*x
Weight Instrumental
Residual Sum of Squares 0.20036
Pearson's r -0.993205
Adj. R-Square 0.985609
Value Standard Error
Hall Resistance Intercept 0 --
Slope -1.92071E-6 5.62652E-8